CHARACTERIZATION OF BENZENE LASER-INDUCED NONTHERMAL EQUILIBRIUM VIA NITRIC OXIDE LASER INDUCED FLUORESCENCE TEMPERATURE MEASUREMENTS

A Dissertation

by

NICLAS ALLEN WEST

Submitted to the Office of Graduate and Professional Studies of
Texas A&M University
in partial fulfillment of the requirements for the degree of

DOCTOR OF PHILOSOPHY

Chair of Committee,	Simon W. North
Committee Members,	Rodney D.W. Bowersox
	Emile A. Schweikert
	Dong Hee Son
Head of Department,	Simon W. North

May 2018

Major Subject: Chemistry

ABSTRACT

A benzene Laser Induced Non-thermal Equilibrium (LINE) technique was characterized for utilization in N_2 supersonic and hypersonic gas flow fields. Characterization of a LINE technique, toward tuning of the rate, magnitude, and geometry of a Collisional Energy Transfer (CET) perturbation to or from the bath is desirable because CET rate has been shown to be coupled with macroscopic flow field properties like turbulent fluctuations in velocity. Therefore, the creation of a tunable LINE technique will allow for testing of the coupling of Non-Thermal Equilibrium (NTE) and turbulence in canonical flow fields in order to create models that can help design more efficient supersonic and hypersonic vehicles. To characterize benzene LINE in this dissertation the relaxation of highly vibrationally excited benzene, generated by pulsed UV laser excitation, was studied using the transient rotational-translational temperature rise of the N_2 bath, which was measured by proxy using two-line Laser Induced Fluorescence (LIF) of seeded NO. The resulting experimentally measured time-dependent N_2 temperature rises were modeled with MultiWell based simulations of CET from benzene Vibration to N_2 Rotation-Translation (V-RT).

In flow fields above room temperature we find that the average energy transferred in benzene deactivating collisions depends linearly on the internal energy of the excited benzene molecules and depends approximately linearly on the N_2 bath temperature between 300 K and 600 K. The results are consistent with experimental

studies and classical trajectory calculations of CET in similar systems. In low temperature flow fields (140 K-300 K) the CET rate was found to have an inverse temperature dependence which may indicate the turning on of a new CET pathway at low temperatures. Since very little work on the relaxation of highly vibrationally excited molecules at temperatures below ~250 K has been done in the past, more experiments and simulations are needed to determine the mechanism of the increase in CET rate at low temperature.

A benzene LINE technique has now been characterized over a diverse range of temperatures. It may now be utilized to generate perturbations in supersonic and hypersonic flow fields.

ACKNOWLEDGMENTS

First, I would like to thank my mom, dad, brother, and extended family for their unending love and support. Next, I would like to thank my advisor, Dr. Simon North, for guiding me and shaping my graduate education one coffee walk at a time. Among the many things that I am glad that I was able to learn about from him are parts of his vast experimental scientific knowledge, his skills at making great presentations, and many of his habits that help create the lifestyle of a successful scientist. I would also like to thank my undergraduate advisor, Dr. Jeffrey Bartz, for providing my first access to a physical chemistry lab and for providing the guidance that I needed to send me running into my graduate school career.

There are many TAMU staff members that made the work that I did at TAMU possible. I want to thank Monica Gonzales for letting all the graduate students in 2109 talk things out with her and for helping push forms through the business office. I want to thank Dr. Lisa M. Pérez for teaching me how to get things done in the chemistry department. I want to thank Will Seward for building and fixing everything imaginable and telling funny jokes while doing it. I want to thank Tim Pehl for helping me save literally thousands of dollars by hacking laser electronics, building custom electronics, and reviving old lab equipment.

The students in the North research group also greatly influenced me while I was at TAMU. I want to thank Michael Grubb for teaching me that you can make your

computer do basically anything with LabVIEW. I would like to thank Michelle Warter for being the wise oldest student still left in the group for my early graduate years. I want to thank Amanda Renz for being another wise old graduate student that shared the office space with us. I would like to thank Wei Wei for letting me “steal” all of the best stuff out of his lab and for sharing Chinese culture with me. I want to thank Rodrigo Sanchez Gonzalez for always answering all of my questions about how the rPHT works. I would like to thank Wade Eveland for housing me when I first moved to College Station and helping me meet people when I was here the first summer before the rest of my class arrived. I want to thank Wilmarie Marrero Ortiz for experiencing and talking through the hurdles of graduate school with me as a graduate student in the North group of the same class year. I would like to thank Feng Pan for great talks in our office, scientific and otherwise, and for sharing Chinese culture with me. I would like to thank Josh Winner for building the best lab sculptures that I have ever seen and for chess advice. I want to thank Zach Buen for gracefully living through the final stressful push in my graduate school career as the Jr student on my project. I would like to thank Colin Wallace for discussing all kinds of cool fancy gadgets like espresso makers and headphones. I want to thank Carolyn Gunthardt for great talks in our office, scientific and otherwise.

I also greatly value the collaboration with aerospace engineers at TAMU that helped me to appreciate the real-world motivation for my research. I want to thank Dr. Rodney Bowersox for providing valuable insights about why my gas flow fields have behaved in weird ways, for maintaining the excellent NAL facility to work at, and for

explaining the real-world examples of how our fundamental chemistry will eventually influence hypersonic travel. I would like to thank Chi Mai for inviting all the NAL students to movies and places to hang out which really made me feel more connected to the NAL even though most of my work was conducted in the chemistry building. I want to thank Brianne McManamen and Ian Neel for helping to maintain good communication between students at the NAL and in the chemistry building.

I would also like to thank a number of my friends for moral support during graduate school. I want to thank Danny and Gabby, for making the houses that we rented feel like homes. I would like to thank Noah for sharing with me his Jim Henson like passion of science/engineering. I want to thank Obi for talking me through tough times. I would like to thank my running club for being the perfect mental escape from graduate school when things were not always going well in the lab and celebrating with me when they were going well. I want to thank my dancing friends for traveling with me out of College Station when I needed to get out of the city from time to time.

Lastly, I would like to thank my other colleagues and the department faculty and staff for making my time at Texas A&M University a great experience.

CONTRIBUTORS AND FUNDING SOURCES

Contributors

This work was supervised by a dissertation committee consisting of Professor Simon North [advisor], Professor Emile Schweikert, Professor Robert Lucchese, and Professor Dong Hee Son of the Department of Chemistry and Professor Rodney Bowersox of the Department of Aerospace Engineering.

The original rPHT cell in Chapter 2 was designed by Dr. Rodrigo Sanchez-Gonzalez and the original slow flow cell in Chapter 2 was designed by previous students in the North research group. Many of the nozzles for the rPHT cell were designed by Dr. Rodrigo Sanchez-Gonzalez, Wade Eveland, and Niclas West with contour curves generated by Dr. Rodney Bowersox. The fuel injector system for pulsing gas at a higher throughput through the rPHT cell was designed by Feng Pan, Josh Winner, and Brianne McManamen. All other modifications to the rPHT cell and the slow flow cell were designed by Niclas West and built by Will Seward and others in the machine shop.

Data in Chapter 5 was collected in part by Josh Winner who also helped with the data analysis. Data in Chapter 6 was collected in part by Zach Buen who also helped with the data analysis. All other data collection and analysis was conducted by Niclas West.

Valuable discussion and collaboration with theoretical chemists Dr. William Hase and Dr. Amit Paul at Texas Tech University helped guide the understanding of the experimental results in Chapter 5. Valuable discussion and collaboration with Dr. Rodney

Bowersox and his aerospace engineering students at the National Aerothermochemical Laboratory at TAMU helped guide understanding of gas flow field behaviors in Chapters 5 and 6.

All other work conducted for the dissertation was completed by Niclas West independently.

Funding Sources

Graduate study was supported in part by a Texas A&M Graduate Merit Fellowship, a JEMS Scholarship for Collaborative Research, a Martin Donald Corera Memorial Endowed Fund Travel Award in Chemistry, and a Jack H. Lunsford '57 Endowed Fellowship in Chemistry.

This work was made possible in part by the United States Air Force Office of Research under Grant Number C13-0027. Its contents are solely the responsibility of the authors and do not necessarily represent the official views of the United States Air Force Office of Research.

NOMENCLATURE

CET	Collisional Energy Transfer
LINE	Laser Induced Non-thermal Equilibrium
TNE	Thermal Non-Equilibrium
t	Time
T	Temperature
<v>	Average Velocity

TABLE OF CONTENTS

Page

LIST OF FIGURES

Page

LIST OF TABLES

CHAPTER I

INTRODUCTION AND LITERATURE REVIEW*

Background and Motivation

Non-equilibrium between the Boltzmann distributions of differing types of molecular motion is known to exist in supersonic and hypersonic flow fields and is known as Thermal Non-Equilibrium (TNE) or Non-Thermal Equilibrium (NTE). TNE is often generated by shock waves and in gas expansion since the gas in the flow experiences a sharp change in pressure and in molecular internal energy as the velocity of the gas flow is increased or decreased over too few collisions for the equilibration of different types of molecular motion to occur. However, the rate of re-equilibration of molecular translation, rotation, vibration, and electronic excitation do not occur on the same time scales and often molecular Collisional Energy Transfer (CET) can occur over the length scale of a flow field. Previous work has shown that this CET can modify macroscopic flow properties, like turbulent fluctuations in velocity, in the flow fields.

---

* Reprinted in part from N. A. West, J. D. Winner, R. D. W. Bowersox, and S. W. North. Resolving the Energy and Temperature Dependence of C6H6* Collisional Relaxation via Time-Dependent Bath Temperature Measurements, The Journal of Chemical Physics **145**, 014308 (2016). with the permission of AIP Publishing.

Reprinted in part from R. Sanchez-Gonzalez, W. D. Eveland, N. A. West, C. L. N. Mai, R. D. W. Bowersox, and S. W. North, Low-temperature collisional quenching of NO $A^2\Sigma^+$(v '=0) by NO($X^2\Pi$) and O_2 between 34 and 109 K, Journal of Chemical Physics **141**, 074313, (2014). with the permission of AIP Publishing.

Turbulence in supersonic and hypersonic boundary layers is often caused by acoustic fluctuations in a flow field. It has also been demonstrated that if molecules in the flow can absorb the acoustic energy through CET of the correct magnitude and time scale, the onset of transition to a turbulent flow field will be delayed. It is favorable in many supersonic and hypersonic flow fields to delay the transition from a laminar flow field to a turbulent flow field. Turbulence in flow fields around supersonic and hypersonic vehicles increases drag and the rate of heating of the vehicle which in turn requires more expensive vehicle exteriors that can either withstand the increased heat or sacrificially ablate when they become too hot in order to protect the interior of the vehicle.

It is not known to what extent TNE can be utilized to modify the acoustic fluctuations that cause turbulence in supersonic and hypersonic boundary layers, but a few studies have begun to measure the coupling between TNE and the modification of turbulence. The first studies to examine the role of TNE in modifying turbulence focused on delaying turbulent transition in hypersonic boundary layers by addition of varying percentages of CO_2 into the flow fields.[1-5] Some of these studies examine flow fields with CO_2 pre-mixed into the gas while others examine the effect of injecting CO_2 into the boundary layer of a hypersonic vehicle. In all cases, it is the bending vibrational mode of CO_2 that is able to collisionally absorb fluctuations in translational energy of the flow field, T-V CET, which causes the delayed transition to turbulence in the flow field.

Since the rate that CO_2 was able to absorb acoustic fluctuations in flow fields caused the delay of transition to turbulence, the next thing studied was the injection of other types of molecules into the same flow fields.[6] The injection of He, N_2, and C_4F_8 into the supersonic 5° angle cone flow field by Schmidt et al. demonstrated that the onset of transition to turbulence was increased in the flow field with He injection and delayed in the flow field with C_4F_8 injection as compared to a flow field with N_2 injection. Therefore, tuning molecular factors that change the rate and magnitude of CET like molecular weight and number of vibrational modes were shown to allow for determination of just the right rate of CET to modify the transition to turbulence in this flow field. This can be clearly seen in Figure 3 of the work by Schmidt et al. where they utilized Schlieren imaging to visualize the change of delay of transition from laminar to turbulent flow field with change in molecular species injected into the flow field.[6] This shows that there are optimal CET rates for absorbing specific frequencies of acoustic fluctuations and therefore the ability to tune CET for diverse flow field conditions is desirable.

Previous work to study the coupling of the decay of turbulence and the generation of TNE was performed by Fuller et al.[7] Decaying turbulence, generated by gas flow through an aluminum grid, was attenuated by a RF plasma downstream of the aluminum grid. After the RF plasma generated v=1 N_2 TNE, and the v=1 N_2 underwent vibration to translation, V-T, collisional relaxation which attenuated turbulent fluctuations in velocity in the flow field and increased the rate of relaminarization of the flow field.

Research Objectives

It is the goal of this dissertation to characterize the collisional relaxation of highly vibrationally excited benzene in nitrogen flow fields toward developing a novel Laser Induced Non-thermal Equilibrium (LINE) technique. The benefits of LINE over other types of TNE modification techniques include: control of the rate of CET in a flow field, control of the total magnitude of TNE/CET in a flow field, and control of the spatial geometry of the perturbation that is created in the flow field. Benzene LINE would allow for the generation of controlled TNE such that the effect of precise amounts of TNE on specific structures in a gas flow field can be examined. For example, benzene LINE could be "written" into a hypersonic flow field before or after shock waves with differing laser beam shapes, sizes, and patterns. Through utilization of benzene LINE with flow field diagnostic techniques like VENOM, the correlation between TNE and the modification of macroscopic flow field properties like turbulent fluctuations in velocity can be examined in a more controlled way than methods of TNE modification have previously allowed.[8, 9]

Literature Survey

Highly Vibrationally Excited Polyatomic Molecule CET

In order to characterize a LINE technique, it is important to first understand any literature on the CET of the molecules utilized in the LINE technique. The collisional relaxation of highly vibrationally excited polyatomic molecules in atomic, diatomic, and polyatomic baths have been studied extensively experimentally and computationally at bath temperatures near room temperature and at limited magnitudes of vibrational

excitation of the highly vibrationally excited molecules. Highly vibrationally excited polyatomic molecules studied include: benzene (C_6H_6)[10-12], deuterated benzenes (C_6D_6)[11, 12], halogenated benzenes (C_6F_6)[10, 12-16], alkyl benzenes (C_6H_5R)[17], azulene ($C_{10}H_8$)[18], naphthalene ($C_{10}H_8$)[19], cycloheptatriene (C_7H_8)[20], and pyrazine ($C_4H_4N_2$)[21, 22]. These highly vibrationally excited molecules have been studied in baths including noble gases[10, 23], CO_2[12-14, 21, 22], N_2[15, 16], H_2O[24], and baths of unexcited polyatomic molecules.[23, 25]

Polycyclic aromatic hydrocarbons (PAHs) and other similar polyatomic aromatic molecules are ideal for studying vibration to rotation/translation (V-RT) CET and vibration to vibration (V-V) CET because ensembles of these molecules can be experimentally prepared in a narrow distribution of highly vibrationally excited states. Experimental generation of highly vibrationally excited molecules is often carried out by photoexcitation with UV light to excited singlet states where subsequent internal conversion to the ground singlet state rapidly occurs. This creates an ensemble of vibrationally excited molecules in a Boltzmann distribution of internal energies at the original temperature of the bath except it is now shifted up in energy by the amount of energy in the absorbed photon.

Another reason that PAHs and other similar polyatomic aromatic molecules are good for studying V-RT CET and V-V CET is that once they are prepared in a highly vibrationally excited state, they do not subsequently undergo reactions as quickly as many other hydrocarbons.[26] The slowness of dissociation can be explained by the RRKM equation which is utilized to predict the rate of unimolecular dissociation, *k(E,J)*.

$$k(E,J) = \frac{G^{\ddagger}(E,J)}{hN(E,J)}, \quad (1)$$

Where *E* is the vibrational energy of the molecule, *J* is the rotational state of the molecule, $G^{\ddagger}(E,J)$ is the sum of states above the transition state at *E* and *J*, *h* is Planck's constant, and *N(E,J)* is the density of states at *E* and *J*. For a large aromatic molecule, $G^{\ddagger}(E,J)$ is relatively small since all of the bonds are strong compared to other hydrocarbons which causes the transition states to be high in energy and the sum of states at large values of *E* to be small. Also, *N(E,J)* is very large for large aromatic molecules at high *E*. Both the small $G^{\ddagger}(E,J)$ and large *N(E,J)* cause the rate of unimolecular dissociation to be relatively low for large aromatic molecules.[26] Therefore, under the correct pressure conditions, most of the highly vibrationally excited molecules will collisionally relax instead of undergoing unimolecular dissociation.

Multi-Exponential Down Models

Under intermediate pressure regimes, it is necessary to predict the likelihood of a strong collision, one that transfers enough energy to bring the molecule below the dissociation threshold, in order to predict overall reaction rates. The distribution utilized to determine the likelihood of strong collisions in many experimental and computational studies is, *P(E,E')*, the probability of transferring a given amount of energy per collision for collisions that transfer energy from the highly vibrationally excited molecule to the bath. The most common model utilized for fitting *P(E,E')* is some variation of the multi-exponential down model.

$$P(E,E') = \frac{1}{C(E')}\sum_{i=1}^{N} f_i \, exp\left(-\left(\frac{E'-E}{\alpha_i(E')}\right)^{Y_i}\right), E' \geq E \quad (2)$$

where *E'* and *E* are the energy of the highly vibrationally excited molecule before and after the collision respectively, *C(E')* is a normalization constant, *N* is the total number of exponentials utilized, f_i is the fractal weighting of each exponential such that the sum of the f_i values equals 1, $\alpha_i(E')$ is a fit parameter that is closely related to the average amount of energy transferred per collision, and Y_i is a parameter to weight either less efficient collisions if $Y_i > 1$ or more efficient collisions if $Y_i < 1$. If Y_i is utilized in *P(E,E')* (i.e. $Y_i \neq 1$), then Y_i is usually less than 1 for polyatomic-diatomic collisions and greater than 1 for polyatomic-polyatomic collisions at room temperature.[23] A simple single exponential down model where $N = 1$ and $Y_i = 1$ was utilized in fits to experimental results in this dissertation since the experiments in this work did not resolve the functional form of *P(E,E')*. Therefore, the single exponential down model predicts that higher amounts of energy transferred per collision is exponentially less likely to happen compared to lower amounts of energy is transferred per collision. In order to determine the functional form of the probability of transferring energy from the bath to the highly vibrationally excited molecule, *P(E',E)*, the detailed balance equation is utilized.

$$\frac{P(E,E')}{P(E',E)} = \frac{\rho(E)}{\rho(E')} exp\left(-\frac{E'-E}{k_B T}\right), \quad (3)$$

where $\rho(E)$ is the benzene density of states at energy E, k_B is the Boltzmann constant, and T is the temperature in Kelvin. Examples of single and double exponential down models are shown in Figure 1.

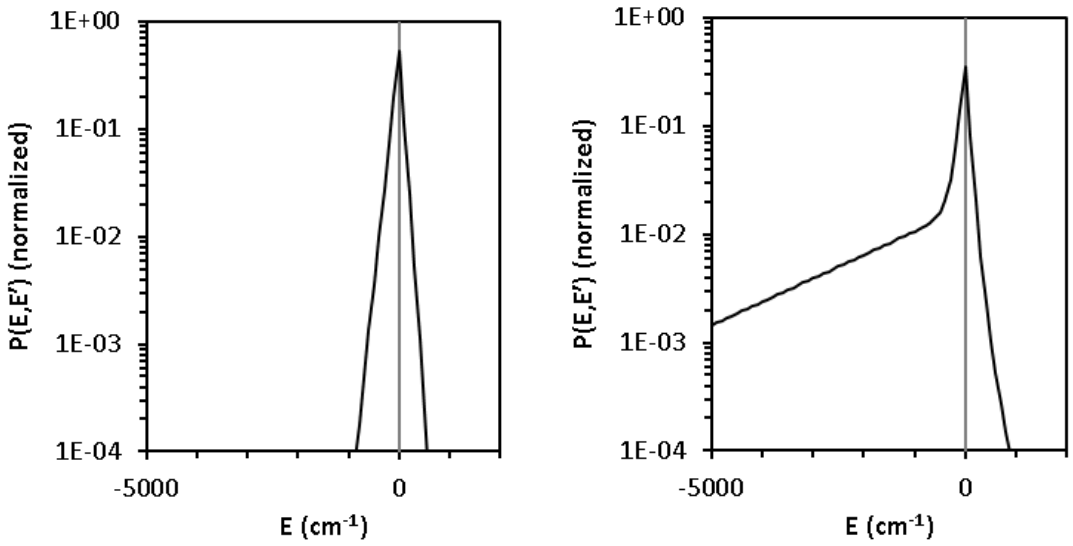

FIG. 1. Left: Plot of example single exponential down model with $f_1 = 1$, $\alpha_1 = 100$, and $Y_1 = 0$. Right: plot of example bi-exponential down model with $f_1 = 0.95$, $f_2 = 0.05$, $\alpha_1 = 100$, $\alpha_2 = 2000$, $Y_1 = 0$, and $Y_2 = 0$.

CET Internal Energy Dependence

The dependence of the internal energy of a highly vibrationally excited molecule on the rate of CET has been studied both experimentally and computationally. A common way to incorporate internal energy dependence into an exponential down model is to use an energy dependent $\alpha_i(E')$ value.

$$\alpha_i(E') = C_0 + C_1E' + C_2(E')^2, \quad (4)$$

Where C_0, C_1, and C_2 are fit parameters. Although many studies model pressure-dependent reaction rate coefficients by utilizing an $\alpha_i(E')$ that is independent of internal energy, E', many other studies that measure CET report an $\alpha_i(E')$ that has been modeled with a linear relationship with E'.

The first evidence for an E′ dependent CET rate between a highly vibrationally excited aromatic molecule, azulene, and a variety of bath gases including monatomic, linear, and nonlinear molecules was observed in experiments by Barker *et al*. where the E′ dependent CET rate was shown to depend on the type of bath gas.[27-29] Later, an E′ dependent benzene CET rate was reported in multiple experiments which monitored the internal energy of the photoexcited benzene during collisional relaxation. In UV Absorption (UVA) experiments carried out by Nakashima *et al.*, the authors measured changes in the transient absorption spectrum of photoexcited benzene and hexafluorobenzene due to CET in a N_2 bath.[30-35] Based on the experimental results, the authors proposed a single exponential decay function for the internal energy of the excited benzene over time implying that the CET rate depends on the internal energy of the excited benzene molecule.[35] In subsequent work, Barker and co-workers monitored infrared fluorescence (IRF) of photoexcited benzene as it collisionally relaxed in many bath gases, including N_2, and fit the experimental data with master equation modeling.[11, 36] These experiments found that the CET from the excited benzene molecules depended

approximately linearly on average internal energy of benzene over a large energy range. For C_6H_6*-C_6H_6 collisions, the authors found that C_6H_6* transferred ~1,500 cm^{-1} per collision given an <E'> of 40,000 cm^{-1} and ~450 cm^{-1} per collision given an <E'> of 10,000 cm^{-1}. For C_6H_6*-N_2 collisions, the authors found that C_6H_6* transferred ~45 cm^{-1} per collision given an <E'> of 34,000 cm^{-1} and ~25 cm^{-1} per collision given an <E'> of 10,000 cm^{-1}.

There have been several experiments and calculations examining energy exchanged in single collisions between single energy-donor molecules and single bath molecules which have also found that CET efficiency depends on the energy-donor molecule internal energy. In one study, Lenzer *et al.* employed single-interaction classical trajectory calculations of benzene and hexafluorobenzene, initiated at various vibrational and rotational excitations, colliding with a variety of rare gases.[10] The authors observed that the energy transferred per collision depended approximately linearly on the level of vibrational excitation of benzene. They also found donor rotational energy to transfer more effectively at higher rotational energy of the donor molecules and to be very small when the donor rotational temperature was close to the bath temperature. In related experiments with excited pyrazine in a CO_2 bath, energy transfer to both rotational and translational energy of the bath increased as the initial internal energy of the pyrazine increased from laser excitation at 308.8 nm (32,383 cm^{-1}) to laser excitation at 266 nm (37,594 cm^{-1}).[22]

Another method that has been utilized to measure the CET rate dependence on *E'* is Kinetically Controlled Selective Ionization (KCSI). CET rate data from KCSI experiments is preferred over UVA and IRF experiments due to the precision of KCSI measurements as discussed by Barker *et al*.[37] In KCSI experiments performed by Lenzer *et al.* on a variety of highly vibrationally excited molecules, the authors resonantly ionized the vibrationally excited molecules within narrow energy windows at varying time delays after the generation of the excited molecules such that collision-dependent internal energy distribution profiles could be obtained.[38-41] The authors suggested that CET efficiency could be roughly modeled utilizing a single exponential-down function, N = 1 and Y_i = 1 in Equation 2, with a $\alpha_1(E')$ that is linearly dependent on *E'*. However, the authors also said that an exponential-down model utilizing more parameters, N ≠ 1 and $Y_i \neq 1$ in Equation 2, is preferred if more accurate CET distribution fits are available for the system under study.

When more data on the post-collision internal energy distributions of a vibrationally excited aromatic molecule and a bath gas is available, *P(E,E')* are often fit to a biexponential-down function, N = 2 and Y_i = 1 in Equation 2, instead of a single-exponential-down function. Utilizing a biexponential-down function allows for the inclusion of a small fraction (usually $f_2 < 0.10$) of supercollisions, collisions that transfer an average of > 2,000 cm^{-1}. Supercollisions were first discovered in a number of experimental and theoretical studies.[42-53] Supercollisions are described by the second exponential in *P(E,E')* such that $\alpha_1(E') << \alpha_2(E')$, and the energy dependence of $\alpha_1(E')$ and

$\alpha_2(E')$ have been experimentally and theoretically fit for a limited energy range for a limited number of systems.

Early work to measure the high energy tail of the biexponential $P(E,E')$ for C_6H_6 was carried out by Flynn and co-workers, who investigated the single collision V-RT CET behavior of photoexcited C_6H_6, C_6D_6, and C_6F_6 colliding with CO_2 by probing CO_2 via Tunable Diode Laser Absorption Spectroscopy (TDLAS)[12, 14] The work revealed a small fraction of supercollisions occurring in CO_2 collisions with nascent highly-excited benzene molecules. These findings are consistent with the findings of Lenzer *et al.* who employed single-interaction classical trajectory calculations of benzene and hexafluorobenzene initiated at various vibrational and rotational excitations colliding with rare gases, and utilized a bi-exponential function for a P_{down} model when fitting changes in internal energy of the excited benzene and hexafluorobenzene.[10] Additionally, in KCSI work by Lenzer *et al.*, biexponential-down and parametric ($Y_i \neq 1$) exponential-down models were used.[38-41]

The dynamics of supercollisions has also been the focus of numerous studies. Clary *et al.* employed vibrational close-coupling infinite order sudden quantum scattering calculations for highly vibrationally excited benzene colliding with rare gases.[54] In this treatment, up to two vibrational modes of a benzene molecule are excited in each simulation and the rotation is fixed. An ensemble of calculations was then run in order to average over all orientations such that an approximation of a full quantum treatment of the collision complex could be achieved. The authors found that an increase in

inelastic cross section occurs with an increase in excitation of low-frequency out-of-plane vibrational modes. These highly excited out-of-plane vibrations are thought to be the origin of supercollisions in benzene molecules. The dynamics of benzene supercollisions was also probed experimentally by Mitchell *et al.* who studied highly excited difluorobenzene isomers colliding with CO_2 by probing CO_2 TDLAS after a single collision.[13] Their results are consistent with quantum scattering calculations that suggest a correlation of benzene v_{11} and v_{16} vibrational modes, the "gateway" modes, with more efficient energy transfer.

One way to determine how an internal energy dependent functional form of *P(E,E')* of a highly vibrationally excited molecule affects the rate of CET as well as the impact it has on reactivity is to examine the moments of the average energy transferred per collision vs the internal energy of the highly vibrationally excited molecule, Equation 5.

$$< \Delta E(E')^n >= \int_0^\infty (E - E')^n P(E, E') dE, \quad (5)$$

Where *n* is the moment number of the internal energy distribution such that n = 1 is the first moment of the average energy transferred per collision. Although both single and biexponential *P(E,E')* models can be tuned to yield the same first moment of the internal energy distribution, $<\Delta E>$, the second moment of the internal energy distribution, $<\Delta E^2>$, will be larger when utilizing the biexponential *P(E,E')* model.[40, 55] A larger $<\Delta E^2>$ value is significant in for reacting systems in which either a larger fraction of reactants would be

quickly collisionally deactivated in the case of a photochemical reaction, or a larger fraction of reactants would be quickly activated in the case of a thermal reaction. Therefore, the biexponential *P(E,E')* model results in different internal energy distributions which affect internal energy dependent rates of reaction to yield different overall rates of reaction than those predicted by the internal energy distributions resulting from the utilization of a single exponential *P(E,E')* model.

The first two moments of the collisional relaxation of hexafluorobenzene and "model" benzene were calculated in recent work by Paul *et al.*[15, 16] There the authors performed classical trajectory calculations of single highly vibrationally excited C_6F_6 or "model" C_6H_6 molecule in constant density periodic baths of N_2 to simulate the time dependent deactivation of the excited molecule. The large variation in the second moment of the CET was shown to not have a significant effect on the overall relaxation rate of the highly vibrationally excited molecule.

CET Mechanisms and Bath Temperature Dependence

A quantity that is reported in studies of CET temperature dependence for many systems is the average energy transferred in deactivating collisions, $<\Delta E_d>$, in Equation 6.[37, 56]

$$< \Delta E_d >= \frac{\int_0^{E'} (E' - E) P(E, E') dE}{\int_0^{E'} P(E, E') dE}. \quad (6)$$

For V-RT CET from benzene and related aromatic species to atomic or diatomic baths there have been conflicting reports of the dependence of $<\Delta E_d>$ on bath temperature.

Barker *et al.* have reported that, in experimentally measured (KCSI and IRF) polyatomic energy-donor molecules in diatomic and monatomic baths, there is very little dependence of CET on bath temperature when measured near room temperature.[37] However, a different temperature dependence model was proposed by Miller *et al.*, who utilized a multiple well master equation approach to study the temperature dependence of energy transfer, first in methane-Ar collisions, and later in propargyl recombination to form benzene between 300 - 2,000 K.[56, 57] In order to fit recombination rate constants, the form of their average energy transferred in deactivating collisions is related to bath temperature through the relation: $<\Delta E_d>=400(T/300)^{0.7}$ cm^{-1}. Yet another study of benzene CET rate dependence on bath temperature was carried out by Bernshtein *et al.* They performed classical trajectory calculations of highly vibrationally excited benzene colliding with unexcited benzene and argon molecules at 100, 200, 300, and 500 K.[23] It was found that $<\Delta E_d>$ in excited benzene-argon collisions increases between 100 and 500 K, but that $<\Delta E>$ remains approximately constant. The increase in magnitude of energy transferred per collision with temperature for V-RT CET is consistent with an impulsive collision model where higher velocity molecules are reflected higher on a repulsive potential energy surface which allows for larger magnitude CET. The actual energy transfer event occurs in about 50 fs at the end of the collision complex lifetime in an impulsive collision.[23] The impulsive collisions model is often proposed to model V-RT CET behavior around or above 300 K.

However, at lower temperatures and for polyatomic-polyatomic collisions "chattering" interactions become more important. In a "chattering" collision, there are many small energy transfer events over the several ps lifetime of the collision complex.[23] This allows for efficient V-V CET as the collision complex lifetime increases with decrease in temperature. In chattering collisions molecular rotations play a little role in CET, rotations are mechanistically involved but there is no net transfer of energy to molecular rotation.

Theoretical Background

Benzene Photophysics

There are many properties of benzene that make it an ideal molecule to utilize for a LINE technique. First, any molecule that is seeded into a gas flow field for a LINE technique should be able to cause a large perturbation per molecule to the bath when excited by laser light so that the concentration of that molecule can be kept small enough to not significantly perturb the flow when it is not excited. It is also desirable that the seeded molecule will not undergo chemical reactions in the flow field so that the only changes to the flow field are the result of the desired LINE perturbation. Therefore, the benzene photophysics that cause it to be an ideal candidate for utilization in the LINE technique will be discussed below.

Benzene photophysics has been well characterized in a number of previous studies.[26, 35, 58-69] Photoexcitation of X ($^1A_{1g}$) benzene to S_1 ($^1B_{2u}$) with T_0 = 38,086 cm^{-1} and to S_2 ($^1B_{1u}$) with T_0 = 49,100 cm^{-1} occurs near 263 nm and 204 nm respectively.[70]

TABLE 1. Benzene absorption cross sections at easily accessible or experimentally relevant wavelengths.

Wavelengths (nm)	Cross sections (cm^2)	Relevance
355	N/A < T_{rm}	Nd:YAG laser 2nd harmonic
266	$2.31x10^{-20}$	Nd:YAG laser 3rd harmonic[71]
248	$2.62x10^{-19}$	KrF excimer laser[71]
226	$2.47x10^{-20}$	NO LIF absorption[72]
193	$1.81x10^{-17}$	ArF excimer laser[73]

The fluorescence quantum yield at excitation wavelengths shorter than 244.5 nm decreases with shortening of wavelength such that the fluorescence lifetime at 266.2 nm excitation is 100 ns where the fluorescence quantum yield is 0.22 and the fluorescence lifetime at 242 nm is 7 ns.[34] Total internal conversion ultimately leading to S_0 occurs within ~10 ps (S_2 decay to S_1 and S_0 ~40fs, S_1 to S_0 ~5-10 ps). The first triplet state ($^3B_{1u}$) with T_0 = 29,510 cm^{-1} is produced through intersystem crossing with a yield of <1% at wavelengths shorter than 244.5 nm and has a phosphorescence lifetime of a few hundred ns. It is thought that most of the benzene photochemistry proceeds from highly vibrationally excited ground-state benzene. There the collision-free dissociation rate of benzene at 193 nm, $1\pm0.2x10^5$ s^{-1}, is insignificant in the pressure regime of this study where the collision rate is approximately $2.4x10^8$ s^{-1}.[26] The major isomers produced from 193 nm excitation of benzene are dewarbenzene, fulvene, and benzvalene.[58] These

isomers are produced with low yield; therefore highly vibrationally excited benzene is generated with a quantum yield near unity at 193 nm.

Nitric Oxide Laser Induced Fluorescence

Since the first step of Laser Induced Fluorescence (LIF) is absorption, all NO LIF experiments must consider that the absorption cross section for nitric oxide near 226 nm is 2.54×10^{-19} cm^2.[74] The fraction of NO molecules that absorb one photon of 226 nm light is given by the fractional absorption equation.

$$\Phi = 1 - exp(-\rho\sigma). \quad (7)$$

Where ρ is photon density in cm^{-2} and σ is the absorption cross section in cm^{-2}.

A simple way to model the LIF process is with a 2 level model presented in Figure 2.[75, 76]

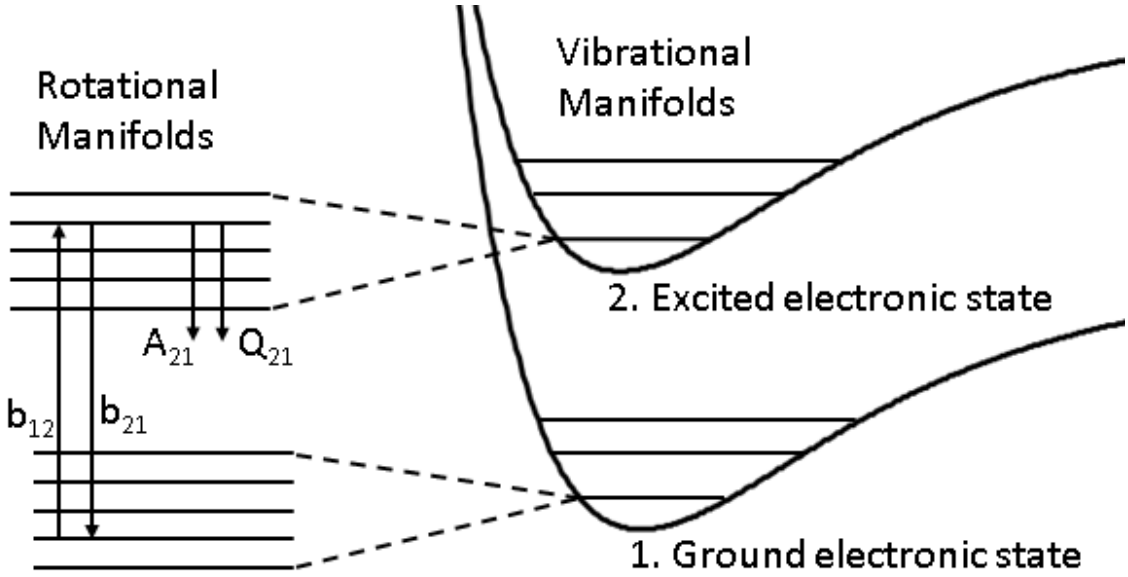

FIG. 2. Two level model energy diagram.

Where the terms used to describe the 2-level system are defined in Table 2.

TABLE 2. Terms used to describe the 2-level model.

Term	Definition	Units
N^0_1	Initial ground state population	cm^{-3}
N_1	Ground state population	cm^{-3}
N_2	Excited state population	cm^{-3}
B_{12}	Stimulated absorption Einstein Coefficient	$m^3J^{-1}s^{-2}$
B_{21}	Stimulated emission Einstein Coefficient	$m^3J^{-1}s^{-2}$
I_{sat}	Saturation intensity	Jm^{-2}
I_l	Laser intensity	Jm^{-2}
A_{21}	Spontaneous emission Einstein coefficient	s^{-1}
Q_{21}	Quenching coefficient	s^{-1}
c	Speed of light ($3x10^8$)	ms^{-1}
$\Omega/4\pi$	Collection solid angle	
H	Fluorescence collection efficiency term	
$h\nu_{emitted}$	Emitted photon energy	J
S_f	Fluorescence signal intensity	Js^{-1}
V	Measurement volume	m^3
$g(\nu_{abs}, \Delta\nu_{abs}, \nu_{las}, \Delta\nu_{las})$	Overlap integral	

The fluorescence signal intensity measured in an LIF experiment is given by Equation 8.

$$S_f = N_2 A_{21} \eta. \tag{8}$$

Where η is a fluorescence collection efficiency term given by Equation 9.

$$\eta = h\nu_{emitted} V \left(\frac{\Omega}{4\pi}\right) [g(\nu_{abs}, \Delta\nu_{abs}, \nu_{las}, \Delta\nu_{las})]. \tag{9}$$

Equation 8 implies that in order to predict the intensity of fluorescence originating from level 2, it is necessary to solve for the population of level 2, N_2. To determine this, start with the differential rate equations for the populations of level 1 (ground) and level 2 (excited) states.

$$\frac{dN_1}{dt} = -b_{12} N_1 + N_2 (A_{21} + Q_{21} + b_{21}). where\ b_{12} = B_{12} \frac{I}{c} \tag{10}$$

$$\frac{dN_2}{dt} = -\frac{dN_1}{dt}. \tag{11}$$

And define,

$$N_1^0 = N_1 + N_2. \tag{12}$$

Then assume the steady state approximation.

$$\frac{dN_1}{dt} = 0 = -b_{12}(N_1^0 - N_2) + N_2 (A_{21} + Q_{21} + b_{21}). \tag{13}$$

Next solve for N_2.

$$N_2 = \left(\frac{N_1^0 B_{12}}{B_{12} + B_{21}}\right)\left(1 + \frac{I_{sat}}{I_l}\right)^{-1}. where\ I_{sat} = \frac{c(A_{21} + Q_{21})}{(B_{12} + B_{21})} \tag{14}$$

Substituting this result for N_2 into Equation 8 yields Equation 15 for the fluorescence signal intensity.

$$S_f = \left(\frac{N_1^0 B_{12}}{B_{12} + B_{21}}\right)\left(1 + \frac{I_{sat}}{I_l}\right)^{-1} A_{21}\eta. \quad (15)$$

From Equation 15, there are three major regimes under which a LIF experiment can be conducted with respect to laser power: saturated ($I_l >> I_{sat}$), partially saturated ($I_l \sim I_{sat}$), and unsaturated ($I_l << I_{sat}$). In the saturated regime, the equation for fluorescence signal intensity is reduced to Equation 16.

$$S_f = \left(\frac{N_1^0 B_{12}}{B_{12} + B_{21}}\right) A_{21}\eta. \quad (16)$$

Here S_f is independent of laser power and quenching and is an ideal regime for conducting experiments. However, the dye lasers capable of producing 226 nm output in the North group labs are not powerful enough to operate in this regime with laser beam diameters that are desirable for experiments presented in this dissertation. In the unsaturated regime the equation for fluorescence signal intensity is reduced to Equation 17.

$$S_f = \left(\frac{N_1^0 B_{12} I_l}{c}\right)\left(\frac{A_{21}}{A_{21} + Q_{21}}\right)\eta. \quad (17)$$

Where the term ($A_{21}/(A_{21}+Q_{21})$) is defined as the fluorescence efficiency since a higher fluorescence efficiency implies that quenching has a lower effect on S_f. Since this regime is linearly dependent on laser intensity, it is referred to as the linear fluorescence regime. It is in this regime that all experiments were carried out in this dissertation. The last regime is the partially saturated regime where S_f varies nonlinearly with I_l. This regime

is therefore not ideal for comparing relative LIF measurements between multiple states since it would require all of the probed states to be equally saturated.

A more accurate way to model the LIF process is with a 5-level model. This analysis has been carried out for NO previously in the North research group and the major effect of this model is to delay the onset of saturation to higher laser powers.[77]

Low Temperature Fluorescence Quenching

The temperature dependence of the quenching cross section of nitric oxide laser induced fluorescence by species in a flow field is important for considering how signal/noise of temperature measurements will be decreased at low temperatures as well as the quenching behavior can be utilized as a tool to determine the density of the bath if the temperature of the bath is also determined. Following laser excitation of NO, the observed fluorescence decays resulting from the parallel reactions of spontaneous emission and quenching can be explained by Equation 18 and Equation 19.

$$NO(A^2\Sigma^+) \xrightarrow{k_f} NO(A^2\Pi), \tag{18}$$

$$NO(A^2\Sigma^+) + M_i \xrightarrow{k_{q,i}(T)} NO(A^2\Pi) + M_i^*, \tag{19}$$

Where k_f is the intrinsic rate of fluorescence of NO (5.19×10^6 s^{-1}), M_i is the number density of quenching species *i*.in the gas mixture in cm^{-3}, and $k_{q,i}(T)$ is temperature dependent quenching rate constant of species *i*.[78, 79]

The quenching behavior of NO LIF by NO and O_2 above 125 K has been previously studied.[78] The range of this characterization was also recently extended to temperatures

as low as 34 K.[79] An inverse power law model that takes into account long-range multipole interactions between NO ($A^2\Sigma^+$, v'=0) and the collision partner was determined to provide a good description of the inverse temperature dependence of the cross sections for NO and O_2 between 34 K – 300 K and was combined with the high temperature fit to obtain the temperature dependent quenching cross section, *σ(T)*.

$$\sigma(T) = c_1\left(\frac{300}{T}\right)^{c_2} + c_3 e^{-c_4/T}, \tag{20}$$

Where *σ(T)* is the species and temperature dependent quenching cross section in Å^2, c_1 – c_4 are fitting parameters, and *T* is the temperature in Kelvin. The experimentally determined values for the fit parameters of the quenching cross sections are given in Table 3.

TABLE 3. Best-fit values for the global modeling of the quenching cross section temperature dependence.

Quencher	c_1 (Å^2)	c_2	c_3 (Å^2)	c_4 (K)
NO($X^2\Pi$)	40.7(0.5)	0.22(0.03)	25.7(2.0)	1.38x10^3(0.2×10^3)
O_2	26.7(0.5)	0.36(0.03)	15.8(0.8)	0.86×10^3(0.12×10^3)

The quenching cross sections of a species can be converted to a quenching rate constant, $k_{q,i}(T)$.

$$\langle \sigma_{q,i}(T) \rangle = k_{q,i}(T) \sqrt{\frac{\pi \mu_{NO,i}}{8 k_b T}}, \tag{21}$$

Where $\mu_{NO,i}$ is the NO/quencher reduced mass and k_B is the Boltzmann constant

The quenching rates of all of the species in the flow field can be summed up to obtain the temperature and pressure dependent fluorescence lifetime of nitric oxide, k_{tot}, Equation 22.

$$k_{tot}(T) = k_f + [M] \sum_{i=1}^{N} k_{q,i}(T) X_{q,i}, \tag{22}$$

Where *[M]* is the total number density of the gas mixture in cm^{-3}, *N* is number of different species present in the gas mixture, and $X_{q,i}$ is the mole fraction of quenching species *i* in the gas mixture. Therefore, if the product of $k_{q,i}(T)$ and $X_{q,i}$ is large compared to k_f, then the fluorescence decay will be fast and there will be less fluorescence signal to acquire and integrate from a PMT of iCCD camera.

Rotational Temperature Measurement

The two major methods of determining the rotational temperature of a N_2 bath via NO LIF utilized in this dissertation are through two-line LIF measurements and through fits to LIF scans. Both of these methods rely on knowing which regions to select of the 8 sets of bandheads (R_{21}, Q_{21}-R_{11}, P_{21}-Q_{11}, P_{11}, R_{22}, Q_{22}-R_{12}, Q_{12}-P_{22}, and P_{12}) that make up the NO gamma band that arise from the $A^2\Sigma^+$ (v′ = 0) ← $X^2\Pi$ (v′′ = 0) transitions described in detail by Herzberg.[80] Peaks of different rotational states in these bandheads often overlap with each other causing difficulties in isolating specific rotational states to

monitor for temperature measurements. This is particularly prominent for shorter wavelength peaks/bandheads since the wavelength of higher *J* peaks decreases with increase in *J* after the bandhead turns around due to the A state equilibrium bond distance of NO being shorter than the X state equilibrium bond distance. Therefore, it is often best to monitor isolated peaks from longer wavelength bandheads if there is any concern that high *J* peaks may interfere with measurements.

In two-line LIF temperature measurements, the ratio of the integrated LIF signal of transitions originating from two different initial states is measured in order to solve for the temperature in Equation 23.

$$R = \frac{S_{f2}}{S_{f1}} = C_{12} f = C_{12} exp\left(\frac{-\Delta E_{21\,vib}}{k_B T}\right)\left(\frac{2J_2'' + 1}{2J_1'' + 1}\right) exp\left(\frac{-\Delta E_{21\,rot}}{k_B T}\right), \quad (23)$$

Where C_{12} is an experimental calibration factor determined by measuring *R* at a known temperature, *f* is the Boltzmann distribution equation, and $\Delta E_{vib} = 0$ for all measurements originating from the same vibrational state in this dissertation.

$$\frac{\partial T}{T} = \left(\frac{k_B T}{\Delta E}\right)\frac{\partial R}{R}, \quad (24)$$

The propagation of error of a temperature measurement implies that it is desirable to choose a large value of ΔE. However, the signal to noise is very low at high *J* states, so usually only moderately high *J* states are selected for measurements. As an example, if measuring a temperature between 300 K and 700 K, the $Q_{22} + R_{12}(5.5)$ and $P_{22} + Q_{12}(17.5)$ transitions in the NO gamma band are good choices because of their high signal to noise,

their lack of overlap with other *J* state peaks, and their high sensitivity to changes in temperature in this temperature range.

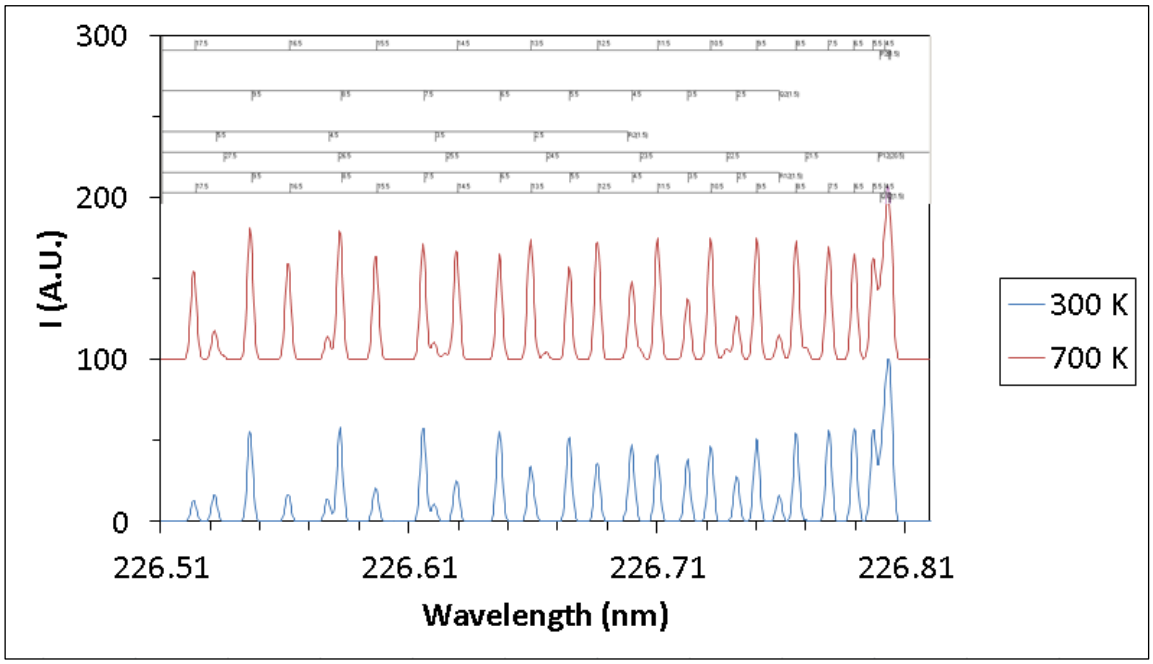

FIG 3. 300 K and 700 K LIFBASE simulations.[81]

When collecting and fitting NO LIF scans for the determination of rotational temperature there are many factors that can influence the wavelength region of the NO gamma band that is selected for the scans as well as the method for fitting the collected scans. First, the same criteria for maximizing ΔE and signal to noise applies to the range of *J* values of peaks selected for the temperature scan as the criteria explained previously for the peaks selected for a two-line LIF temperature measurement. Also, it is desirable

to locate regions to scan such that all desired peaks are in as small of a range of wavelengths as possible without significant overlap of the peaks in order to minimize the time it takes to collect each spectrum. If trying to fit a temperature with peaks from different bands, it is also desirable to select peaks that have a somewhat similar peak height since that gain on a PMT or Camera is fixed during a scan. As an example, if measuring a temperature between 140 K and 230 K, peaks in the Q_{22}-R_{12} and Q_{12}-P_{22} bandheads in the NO gamma band are good choices because of their high signal to noise, their lack of overlap with other *J* state peaks, and their high sensitivity to changes in temperature in this temperature range.

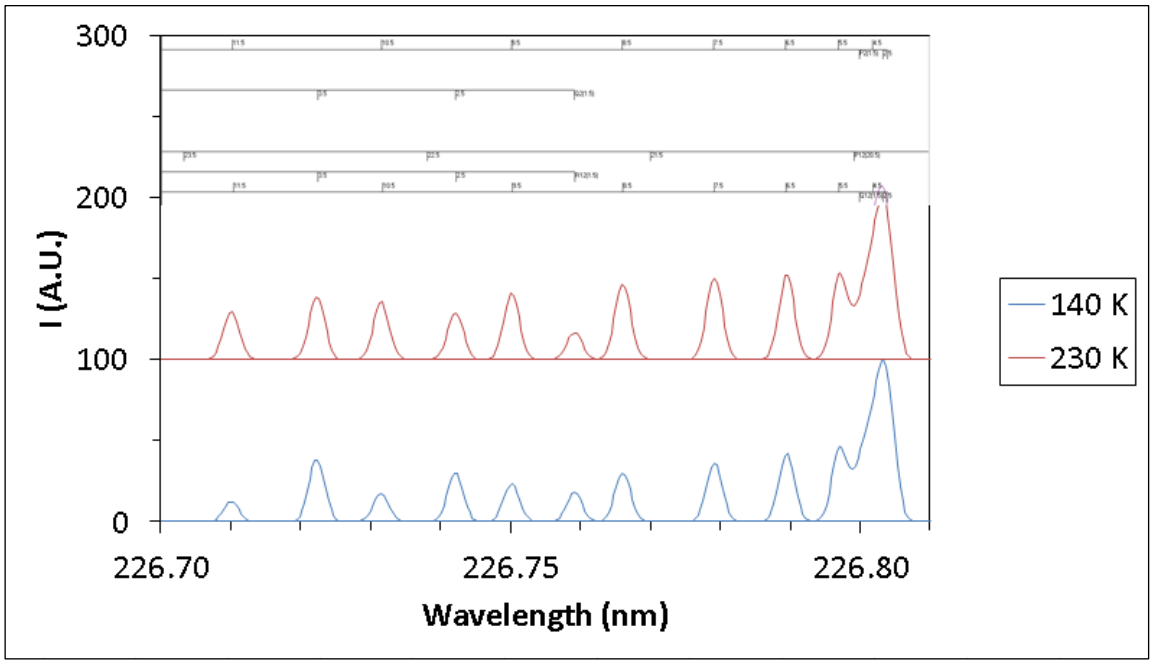

FIG. 4. 140 K and 230 K LIFBASE simulations.[81]

Thesis Overview

This dissertation is organized in seven chapters. Chapter I establishes the motivation for the development of a benzene LINE technique and provides an overview of the collisional energy transfer literature and theoretical background that guided the development of a method to characterize benzene LINE in a diverse range of gas flow field conditions. Chapter I describes how the relaxation of photoexcited benzene has been studied and modeled in the past as well as how nitric oxide LIF can be utilized to measure N_2 bath temperature rises due to the collisional relaxation of highly vibrationally excited benzene.

Chapter II describes the instrumentation that was developed in order to characterize benzene LINE in a diverse range of gas flow field conditions. It starts by describing how to seed a small percent of benzene into gas flow fields. Chapter II then describes laser systems that were utilized to pump benzene gas and also to measure rotational temperatures of the bath. Lastly, Chapter II describes two vacuum chambers, a slow flow cell and the rPHT, that were utilized to characterize benzene LINE at temperatures from 300 K to 700 K and 140 K to 300 K respectively.

Chapter III provides a description of many considerations that are necessary for precise measurements of the bath rotational temperature via NO LIF. The utilization of either a PMT or an iCCD camera is discussed for integrating NO LIF signals. Then methods for automating the fitting of scans over NO rovibronic transitions in order to quickly yield temperature values are discussed.

Chapter IV discusses the theory and method utilized for modeling the collisional relaxation of highly vibrationally excited benzene with the MultiWell master equation solving program[82, 83] Then a description of how the collision dependent rate of energy loss of benzene is converted to a rise in temperature of bath via integration of the bath heat capacity is discussed.

Chapter V describes experiments that were performed to characterize benzene LINE between 300 K and 700 K. All measurements in Chapter V were conducted in a flow field that started at 300 K and, due to variation of the concentration of benzene and the power of the pump laser, different regions of the flow field increased to different final temperatures through the V-RT collisional relaxation of benzene. By fitting the rate of temperature rise for regions of gas that achieved different final temperature values, it was determined that the rate of CET depended approximately linearly on both benzene internal energy and bath temperature.

Chapter VI describes experiments that were performed to characterize benzene LINE between 140 K and 300 K. Initial bath temperatures between 140 K and 200 K were generated via controlled expansion of gas through a pulsed de Laval nozzle instrument. Through fitting temperature rises at varying initial temperature and to varying final temperature, it was determined that the collisional relaxation rate of benzene exhibits an inverse temperature dependence below 300 K. It is possible, but not confirmed in this dissertation, that the inverse temperature dependence indicated that V-V collisional

deactivation pathway(s) turn on at low temperatures and become the dominant CET pathway.

Chapter VII provides conclusions obtained from the experiments described in Chapters V and VI. The dependence of benzene LINE on factors like concentration of benzene, pump laser power, pump laser wavelength, and bath temperature is discussed. Chapter VII also describes two possible future directions to take based on research performed in this dissertation: the characterization of LINE techniques based on other seed molecules and the utilization of benzene LINE in supersonic and hypersonic flow fields.

CHAPTER II

EXPERIMENTAL METHODS*

In order to characterize benzene LINE, special instruments were constructed so that benzene LINE characterization could be conducted at a smaller scale than in a typical hypersonic wind tunnel so that characterization experiments were conducted more quickly and less expensively. For all of the experiments, a mixture of $N_2/C_6H_6/NO$ gases was generated and subsequently fed into a continuously vacuumed instrument in order to generate a continuously refreshing gas flow field. Each experiment was initiated by pumping the C_6H_6 with pulsed ns UV light and at subsequent time delays the N_2 bath rotational temperature was probed by proxy via NO Laser Induced Fluorescence (LIF) measurements. These measurements yielded transient bath temperature rises that were utilized to characterize the possible rates and magnitudes of benzene LINE perturbations that can be controllably achieved in supersonic and hypersonic flow fields.

---

* Reprinted in part from N. A. West, J. D. Winner, R. D. W. Bowersox, and S. W. North. Resolving the Energy and Temperature Dependence of C6H6* Collisional Relaxation via Time-Dependent Bath Temperature Measurements, The Journal of Chemical Physics **145**, 014308 (2016). with the permission of AIP Publishing.

Reprinted in part from R. Sanchez-Gonzalez, W. D. Eveland, N. A. West, C. L. N. Mai, R. D. W. Bowersox, and S. W. North, Low-temperature collisional quenching of NO $A^2\Sigma^+(v'=0)$ by NO($X^2\Pi$) and O_2 between 34 and 109 K, Journal of Chemical Physics **141**, 074313, (2014). with the permission of AIP Publishing.

Gas Mixture Generation

The gas mixtures in this dissertation were prepared by mixing a constant ratio of NO gas and N_2 gas just prior to passing the gas through a high pressure bubbler with benzene. The mixture of certified 5% or 99.95% NO in N_2 (Matheson) and 99.99% N_2 (Praxair) was maintained at a constant pressure between 102 to 621 kPa depending on the experiment kPa by a LabVIEW Proportional-Integral-Derivative (PID) algorithm. The PID algorithm monitored by the pressure-dependent DC voltage output of a pressure transducer (Omega Type PX309-200A5V) with a range of 1379 kPa and generated a pressure dependent DC voltage output to control Mass Flow Controllers, MFC, (MKS Mass-Flo 1179A) driven by a four-channel power supply/readout (MKS 247) operated in constant-flow-ratio mode. The NO/N_2 gas was passed through a custom-built, jacketed, high-pressure bubbler, Figure 5, containing benzene (C_6H_6) (99.8%, Sigma-Aldrich).

FIG. 5. Left: SolidWorks jacketed high pressure bubbler. Right: Photos of a jacketed high pressure bubbler.

The resulting mixture was then passed through a custom-built water cooled 7.5 m stainless steel coil, Figure 6, which maintained a constant partial pressure of C_6H_6 by condensing excess C_6H_6 above the desired vapor pressure.

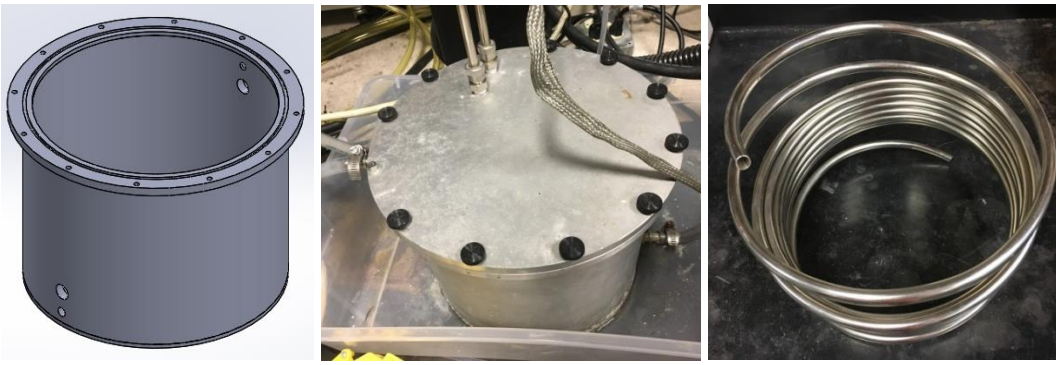

FIG. 6. Left: SolidWorks Schematic of jacket for jacketed condensation coil. Right: Photos of jacketed condensation coil and a stainless-steel coil that is similar to the one in the jacketed condensation coil.

The water was maintained at a constant temperature which was adjusted between 6.5 - 21°C by a refrigerated circulating bath (Cole-Parmer Type Polystat 12102-00) yielding a partial pressure of 5.2 – 10.4 kPa of C_6H_6 (0.8 – 10.4% of the gas mixture). The partial pressure of C_6H_6 in the gas mixture was calculated using the Antoine equation to determine the temperature dependent vapor pressure of C_6H_6.

$$P_{vap} = 10^{A-\frac{B}{T+C}}. \tag{25}$$

Where P_{vap} is pressure in bar, T is temperature in Kelvin, and the values for parameters for A, B, and C were determined experimentally to be 4.01814, 1203.835, and -53.226 respectively over the temperature range 287.70 – 354.07 K.[84] For temperatures outside this range the Clausius-Clapeyron equation was utilized to calculate the temperature dependent vapor pressure of C_6H_6 and a plot of the curves from 200 K to 350 K can be seen in Figure 7.

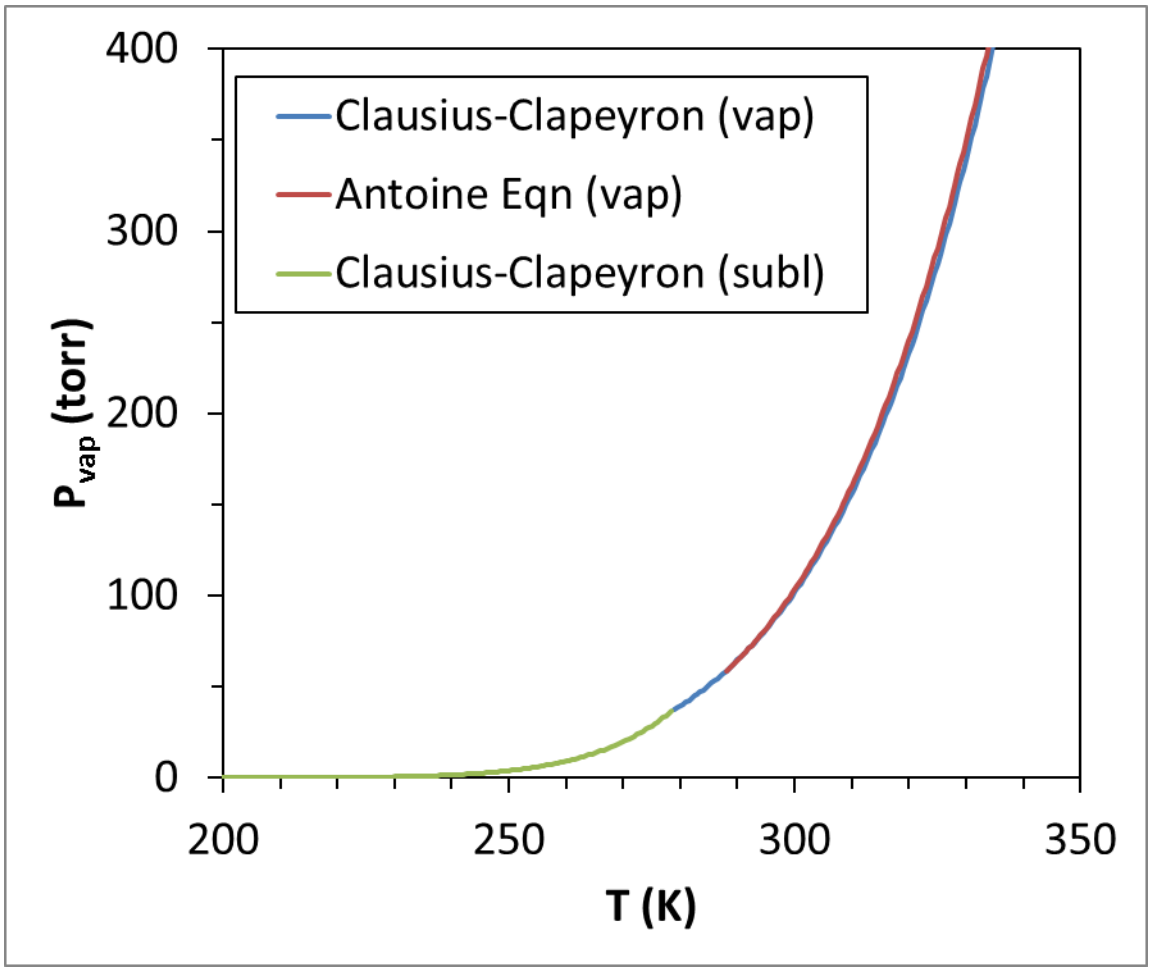

FIG. 7. Phase diagram indicating the temperature dependent vapor pressure of benzene where T_{fusion} = 278.6 K, T_{boil} = 353.3 K, T_c = 562 K, $\Delta H_{vaporization}$ = 33,000 J/mol, and $\Delta H_{sublimation}$ = 45,000 J/mol.[85]

The Antoine equation and the Clausius-Clapeyron equation yielded vapor pressure values that differed from each other by less than 3.1% for all vapor pressure values plotted.

A schematic diagram of gas mixture generation section of the instrument is shown in Figure 8.

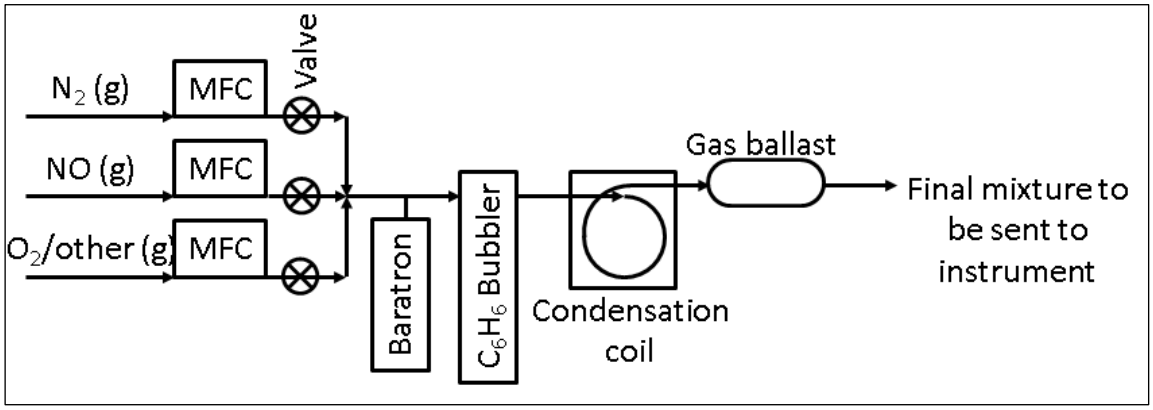

FIG. 8. Generalized schematic diagram of the gas mixture generation section of the instrument.

The generation of gas mixtures with controlled concentrations of benzene via the bubbler-condenser system was verified through UV-Vis absorption measurements. A Benzene absorbance spectrum for the rovibronic progression of the $S_1(^1B_{2u}) \leftarrow X(^1A_{1g})$ transition is shown in Figure 9.

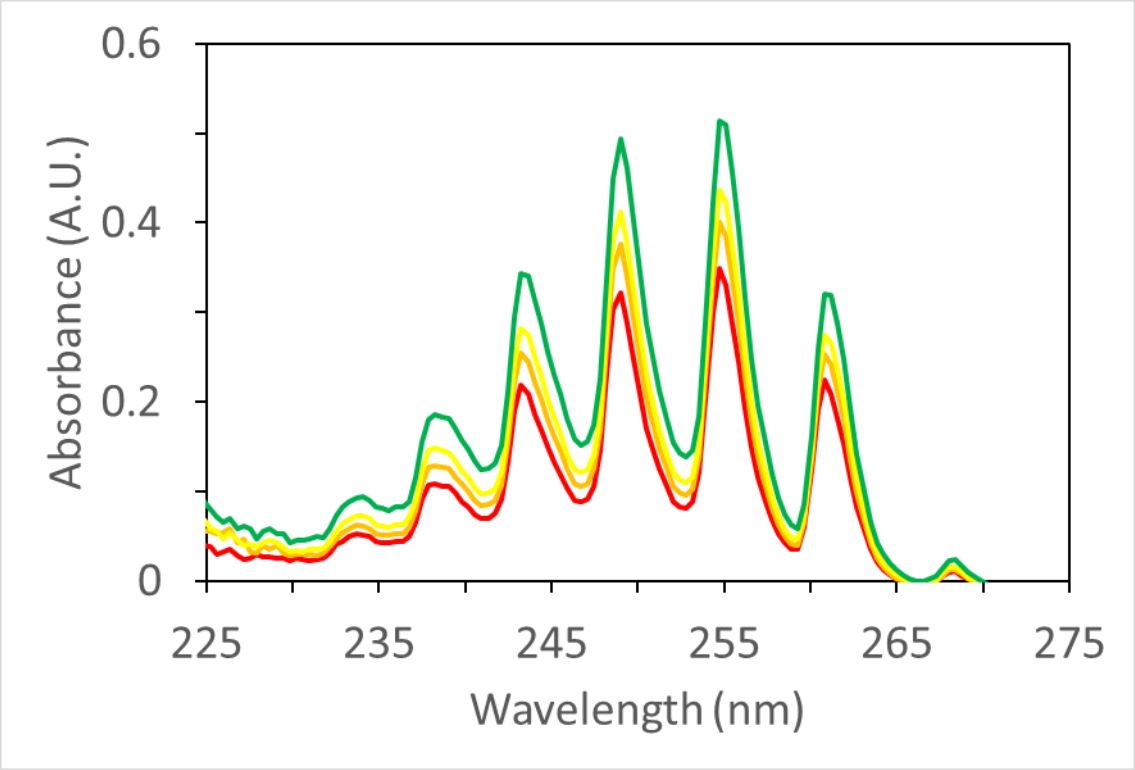

FIG. 9. Benzene absorbance spectra for the rovibronic progression of the $S_1(^1B_{2u}) \leftarrow X(^1A_{1g})$ transition. The red curve indicates [C6H6] = 1.16×10^{17} cm^{-3}, the orange curve indicates [C6H6] = 1.39×10^{17} cm^{-3}, the yellow curve indicates [C6H6] = 1.62×10^{17} cm^{-3}, and the green curve indicates [C6H6] = 1.96×10^{17} cm^{-3}.

Absorption at wavelengths shorter than 225 nm is not shown due to poor S/N due to low lamp intensity and low transmission of wavelengths shorter than 225 nm in the utilized UV/Vis instrumental setup. The concentration of benzene in generated gas mixtures was determined to be correct over the range of gas flow rates utilized in this dissertation from linear fits of a Beers law plots.

Laser Systems

Pump Laser

Highly vibrationally excited benzene (C_6H_6*) was generated by excitation at 193 nm using the ArF output of an excimer laser (Lambda Physik COMPex 201) operating at between 0.5 - 10 Hz. Based on the absorption cross section of C_6H_6 of 1.8×10^{-17} cm^2 at 193.1 nm and the laser fluences employed, fractional excitations of approximately 0.1 - 0.3 were achieved within the beam volume.[86, 87]

The shot-to-shot power of the 193 nm light could be monitored on the hand-held readout of the COMPex 201 laser, but other methods were also developed so that the power meter could be removed from the COMPex 201 laser to achieve higher overall power from the laser. One method was to make a calibration curve by fitting the average benzene emission vs the average 193 nm laser power, shown in Figure 10, so that benzene emission in experiments could be utilized to monitor shot-to-shot fluctuations of 193 nm laser power.

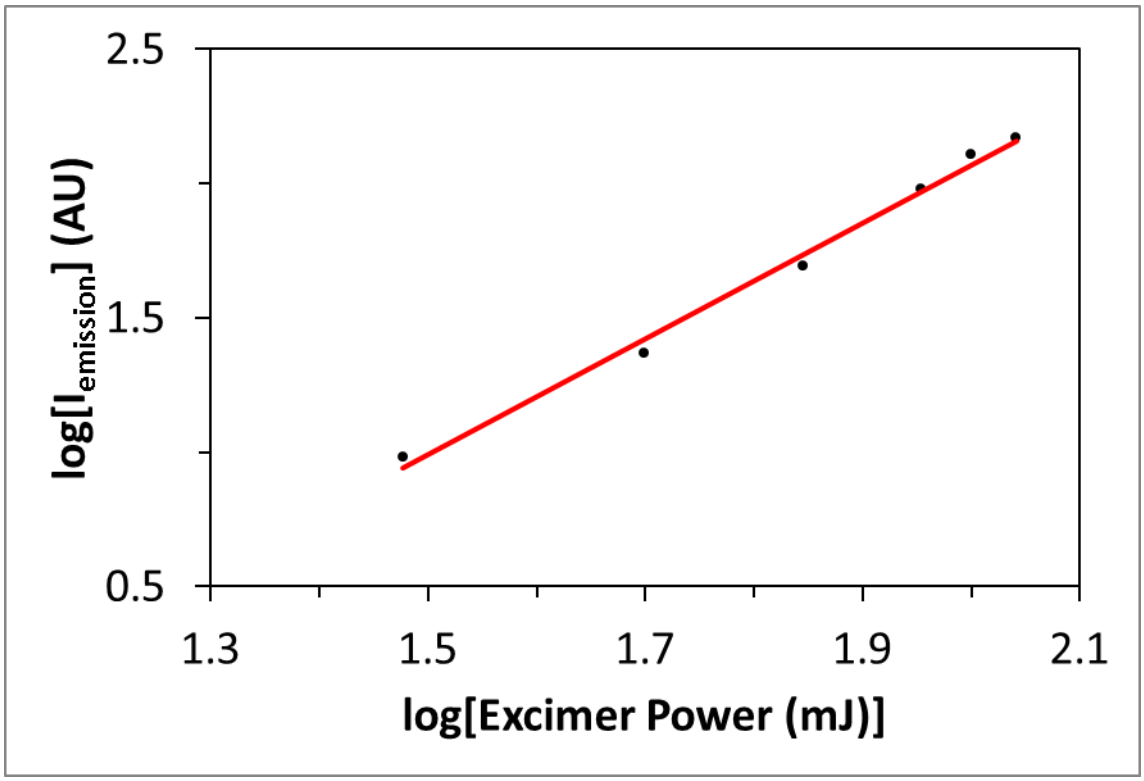

FIG. 10. Log of C_6H_6 emission vs log of 193 nm laser power (black circles) and fit line (red).

The slope of 2.16 obtained from Figure 10 indicates that the benzene emission was an approximately 2 photon process so the square root of the benzene emission is approximately linearly dependent on the 193 nm laser power. Another method that was utilized to measure the shot-to-shot power fluctuations of the 193 nm pump laser was to place a quartz cuvette containing coumarin 450 in methanol in front of 193 nm light scattered off of the entrance windows to instruments and to monitor the emission of the coumarin 450 with a fast photodiode (Thorlabs Type DET10A) or a PMT (Hamamatsu Type H6780-03), digitize the signal with an oscilloscope (Tektronix Type 2012B), and send

the digitized signal to a computer where a custom LabVIEW program integrated and plotted the emission for each laser shot.

It was also important to measure that benzene internal conversion after absorption of pump laser light and consequently the total energy transferred to the bath was linear with pump laser power. This was achieved by measuring the maximum temperature of the bath temperature rises due to $C_6H_6^*$ CET and determining that it was linear with respect to pump laser power. Attenuation of the pump beam was achieved via successive additions of fused silica windows into the beam path. Plots of the maximum temperature vs pump beam power and vs the square root of the integrated benzene fluorescence are shown in Figure 11.

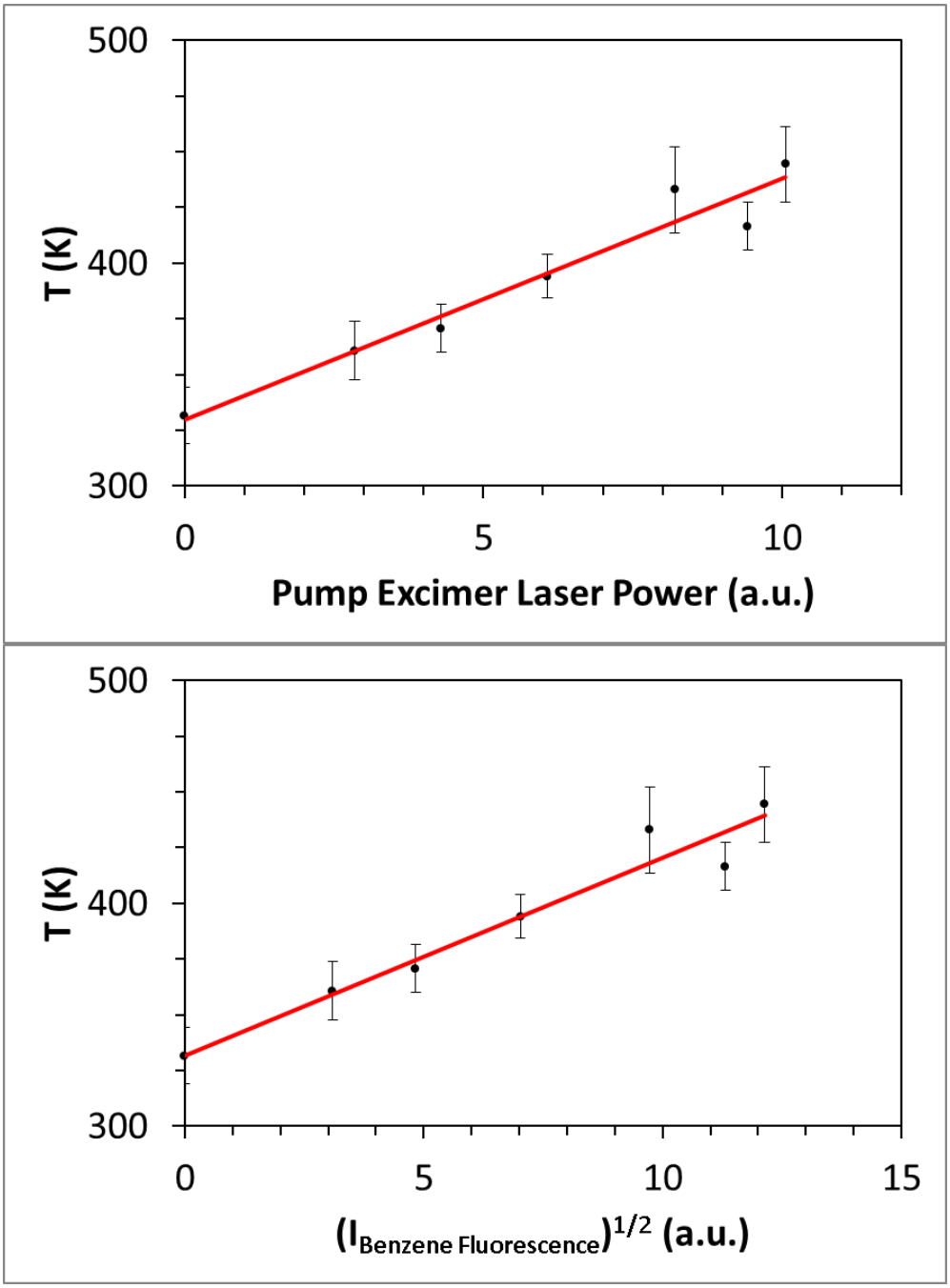

FIG. 11. Top: <T_{max}> vs pump beam power. Bottom: <T_{max}> vs the square root of the integrated benzene fluorescence.

Attenuation of Pump Laser Light

There are a number of factors that can attenuate the pump laser beam between the initial laser output and the probed interaction region in an instrument including absorption by O_2, transmission by mirrors, absorption by glass/fused silica, and absorption by C_6H_6. The absorption cross section of O_2 at 193 nm is 9.87×10^{-23} cm^2.[88] A loss of 4.7% of 193 nm beam power per meter is predicted assuming a room pressure of 760 torr with 20% oxygen at 300 K. The loss of pump laser power due to attenuation by O_2 can be minimized if the beam is enclosed by a PVC tube that is continuously purged with pure nitrogen. The loss of pump laser power due to transmission by mirrors and absorption by glass/fused silica windows can be minimized by minimizing the number of mirrors and windows utilized in the experiment. The absorption by benzene in a vacuum chamber can be minimized if a N_2 purge system is designed into the vacuum chamber to keep benzene from diffusing into any space between the window that the pump laser enters the chamber and the interaction region where it is desired that highly vibrationally excited benzene is generated.

Probe Lasers

The bath time dependent rotational-translational temperature was measured via laser induced fluorescence (LIF) using the $A^2\Sigma^+$ ($v' = 0$) $\leftarrow X^2\Pi_{1/2}$ ($v'' = 0$) transition near 226 nm. The bath time dependent rise in vibrationally excited NO was measured via laser induced fluorescence (LIF) using the $A^2\Sigma^+$ ($v' = 1$) $\leftarrow X^2\Pi_{1/2}$ ($v'' = 1$) transition near 224 nm. The NO LIF probe beam (7 x 2 mm) was generated by the frequency doubled tunable

output of a Sirah Cobra CBR-G-18 pulsed dye laser using coumarin 450 in methanol. The dye laser was pumped by the 355 nm third harmonic of a Spectra Physics LAB-150-10 Nd:YAG laser operating at 10 Hz. The 226 nm pulses had typical durations of 10 ns, linewidth of 0.08 cm^{-1}, and exit power of 2 mJ/pulse (2×10^5 W). The delay between the pump and probe lasers was varied by a digital delay generator (BNC, Model 565). Under a normal set of conditions for an experiment presented in this dissertation, a 226 nm beam of roughly 0.2 cm diameter and 2 mJ $pulse^{-1}$ passing through a gas at a total pressure of 1 torr with 1% NO at 140 K the fractional absorbance of NO, according to Equation 7, is ~ 0.018 or 98.2% of the NO remains unexcited and over a 1 m path length the 226 nm laser beam is only attenuated by about 1.7%. Therefore, in most of the LIF experiments presented in this dissertation there is negligible attenuation of the 226 nm laser beam and only a small fraction of the NO is ever excited by the laser.

NO LIF emission from excitation near 224 - 226 nm occurs primarily between ~224 - 300 nm with the maximum emission occurring near 236 nm. The emission of benzene occurs between ~275 - 325 nm, with a maximum occurring at ~290 nm as shown in Figure 12.

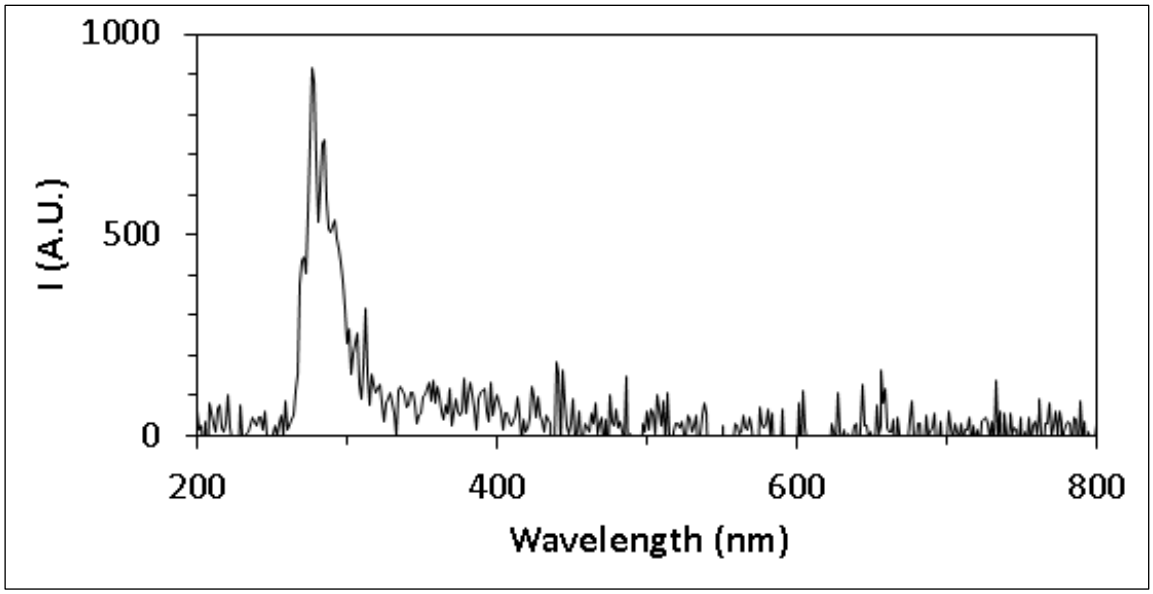

FIG 12. Benzene fluorescence spectrum from excitation by deuterium lamp, 30 s integration

There is overlap in the wavelengths from NO LIF and benzene emission, therefore at low pump-probe time delays benzene emission had to be subtracted from NO LIF signal.

The NO LIF signal was determined to be in the linear regime with respect to probe laser power by attenuating the probe beam with successive additions of fused silica windows into the beam path or detuning the doubling crystal of the probe laser and then fitting the integrated NO LIF intensity vs probe beam power as shown in Figure 13 where its linearity is predicted by the unsaturated regime the equation for fluorescence signal intensity Equation 17.

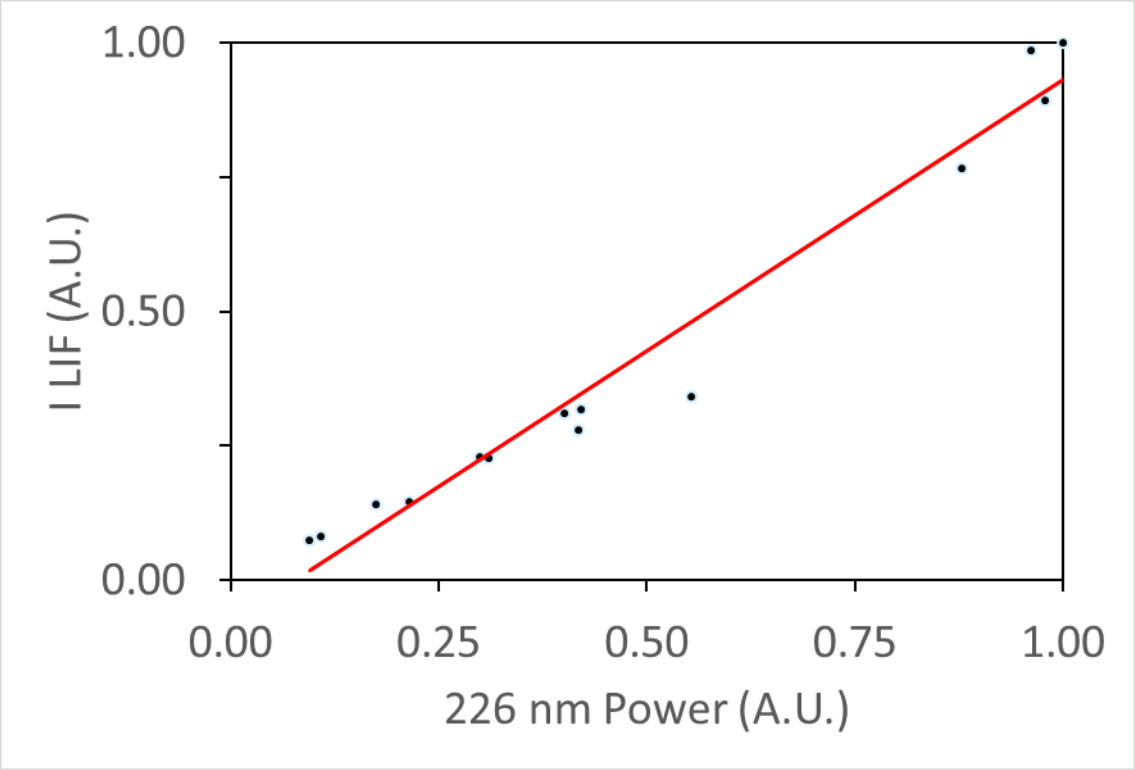

FIG 13. NO LIF signal vs 226 nm power.

Shot-to-shot probe laser power fluctuations were also monitored by directing scattered light from the probe beam onto a phosphor plate (Type P46) and measuring the phosphorescence with a PMT (Hamamatsu Type H6780-03). To remove room light, a UG5 visible filter (Thorlabs) was mounted to the phosphor plate, and to remove light besides phosphorescence, a 546.1 nm band pass filter (Omega Optical Type 546.1BP10) was mounted to the PMT.

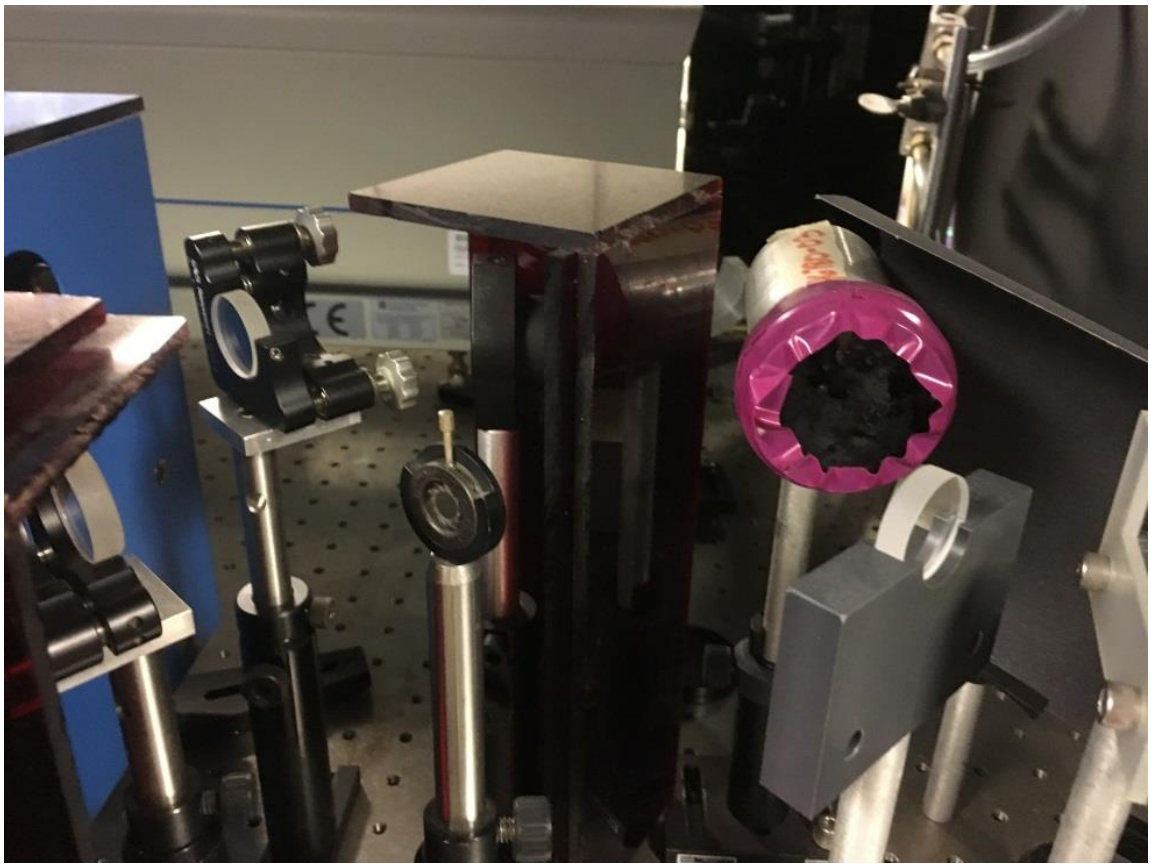

FIG. 14. Probe laser power correction setup.

The PMT signal was then digitized by a 12-bit Lecroy (HRO 66Zi) oscilloscope at a sampling rate of 2 GS/s and integrated using a custom LabVIEW program. The resulting phosphorescence signal was integrated with a 1,000 ns gate. Due to the linear dependence of NO LIF on probe laser power, variation in NO LIF signal due to shot-to-shot fluctuations in probe laser power were corrected by dividing LIF signal by the integrated power-correction phosphorescence signal.

When it was necessary to subtract benzene emission from NO LIF data (especially at the lowest pump-probe time delays), isolated benzene emission signal was collected by blocking the probe beam with a beam flag. The beam flag consisted of a business card taped to a servo motor (EMAX ESO8A) controlled by LabVIEW through a single-board microcontroller (Arduino UNO).

NO Fluorescence Capturing Methods

Time-dependent broadband NO fluorescence decays were collected perpendicular to the pump and probe beams from a region of interest focused by a UKA 105 mm F/4.0 UV lens onto a micro-channel plate photomultiplier tube (MCP-PMT) (Hamamatsu R5916U-50) biased with −2.9 to −1.5 kV. The lens transmission is constant at ∼85% in a wavelength range from 200 to 1100 nm and the MCP-PMT spectral response covers a wavelength range from 160 to 850 nm, both being sufficient to collect the entire $A^2\Sigma^+(v'=0 \text{ or } 1) \rightarrow X^2\Pi(v'')$ progression. No optical filters were employed. The resulting signals were measured and digitized using a 12-bit Lecroy (HRO 66Zi) oscilloscope at a sampling rate of 2 GS/s, and collected and averaged in a computer. An estimate of the effects of radiative trapping on fluorescence collection resulted in attenuation of the total fluorescence of less than 3% in all experiments.

In addition, fluorescence images were acquired with an Andor iStar DH734 ICCD camera situated perpendicular to the pump and probe beams. A -10°C CCD temperature was maintained by the camera's internal thermoelectric cooler which was cooled with 21°C water maintained by a refrigerated circulating bath (Neslab Type CFT-25). The

fluorescence was focused onto the camera with a UKA 105 mm F=4:0 UV lens mounted on extension rings. To reduce contributions from background light in the room a UG5 visible filter (Thorlabs) was mounted to the front of the lens, providing a band-pass filter for light near 240 - 395 nm. During acquisition, iCCD pixels were often binned to obtain less than the full 1024 pixel x 1024 pixel images on the camera in order to run experiments up to 10 Hz due to the increased image transfer rate from the camera to the computer for higher binning of pixels. Image signals were often integrated on the CCD for 1 - 10 laser shots.

LIF excitation scans were performed using a custom LabVIEW program that scanned the probe laser wavelength in a region from 223 to 227 nm, near the bandheads of the $A^2\Sigma^+(v'=0 \text{ or } 1) \leftarrow X^2\Pi_{1/2}(v''=0)$ bands. Scans could be collected by integrating fluorescence traces from the Lecroy oscilloscope at each wavelength position and plotted as a function of laser wavelength. Scans were also collected by integrating pixels from iCCD images at each wavelength position and plotted as a function of laser wavelength.

Gas Flow Chambers

Room Temperature Chamber

Experiments to measure the bath temperature rise due to collisional energy transfer (CET) from highly vibrationally excited benzene (C_6H_6*) starting with a room temperature bath were performed in a custom-built slow-flow cell shown in Figure 15-16.

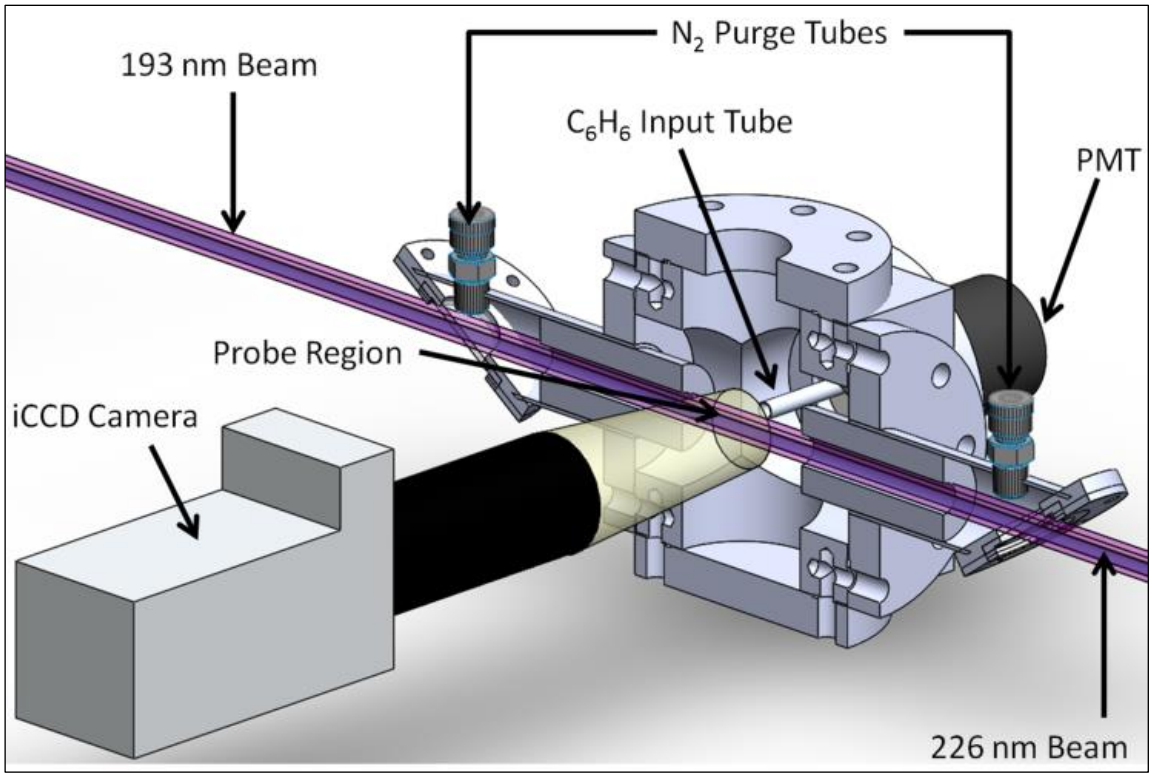

FIG 15. Schematic diagram of slow-flow cell.

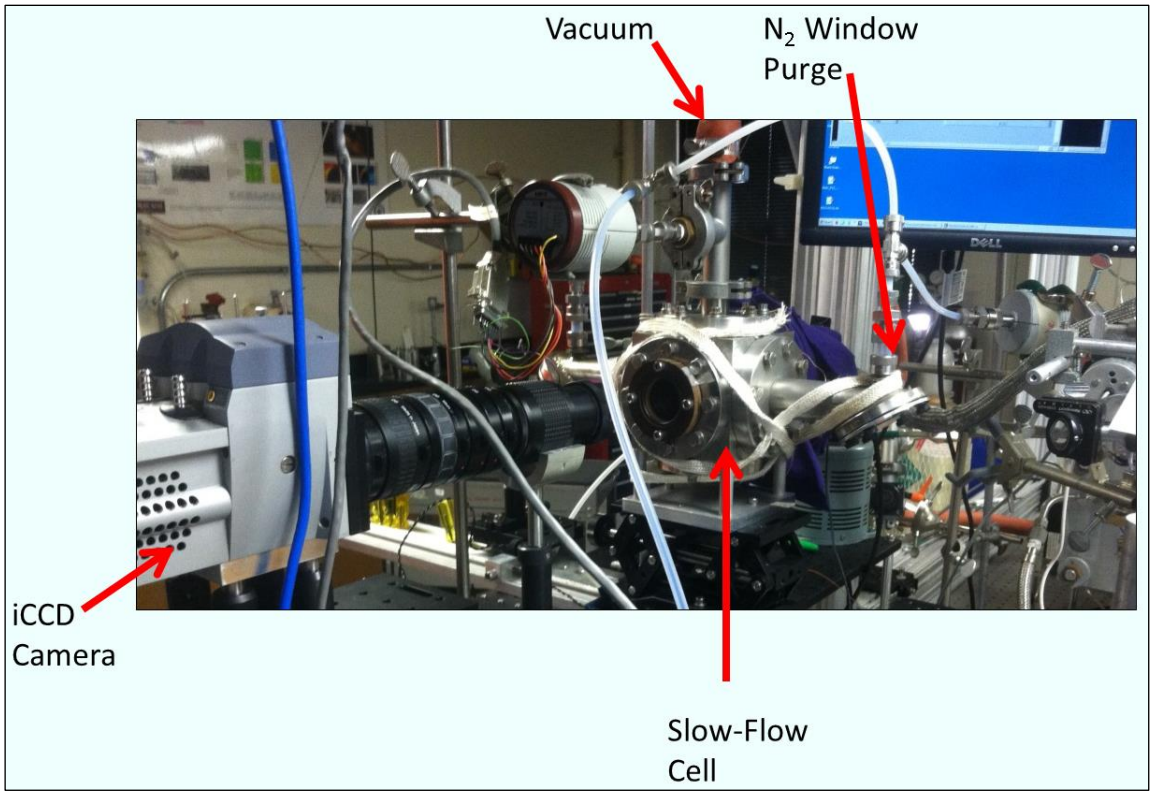

FIG. 16. Photo of slow-flow cell.

Reactant gases were introduced into the cell by Mass Flow Controllers, MFC, (MKS Mass-Flo 1179A) driven by a four-channel power supply/readout (MKS 247) operated in constant-flow mode. One mass flow controller introduced the C_6H_6 gas mixture into the cell, and another mass flow controller introduced N_2 through the window purge lines of the cell to ensure that there was a very low concentration of C_6H_6 near the cell windows. Prior to each experiment the cell windows were treated with a UV/ozone cleaner (BioForce Nanosciences Type ProCleaner 110) for 30 minutes to reduce C_6H_6 adsorption and burning onto the windows. The cell was pumped down by a Leybold D65B backing pump and Ruvac WS1001US Roots blower system establishing a

slow flow system to ensure that reactant gas was refreshed between every laser shot. Pressure in the cell was monitored by a pressure transducer (Baratron MKS Type 622) with a range of 13.3 kPa. The pump laser beam and probe laser beam were collinearly aligned through the cell. During acquisition, iCCD camera pixels were often binned to obtain 16 pixel x 32 pixel images on the camera yielding an image spatial resolution of 0.985 mm/pixel x 1.970 mm/pixel (V x H).

Repetitively Pulsed Hypersonic Test Chamber

Experiments to measure the bath temperature rise due to collisional energy transfer (CET) from highly vibrationally excited benzene (C_6H_6*) starting with a less than room temperature bath were performed in a custom-built repetitively Pulsed Hypersonic Test (rPHT) cell shown in Figure 17-18.

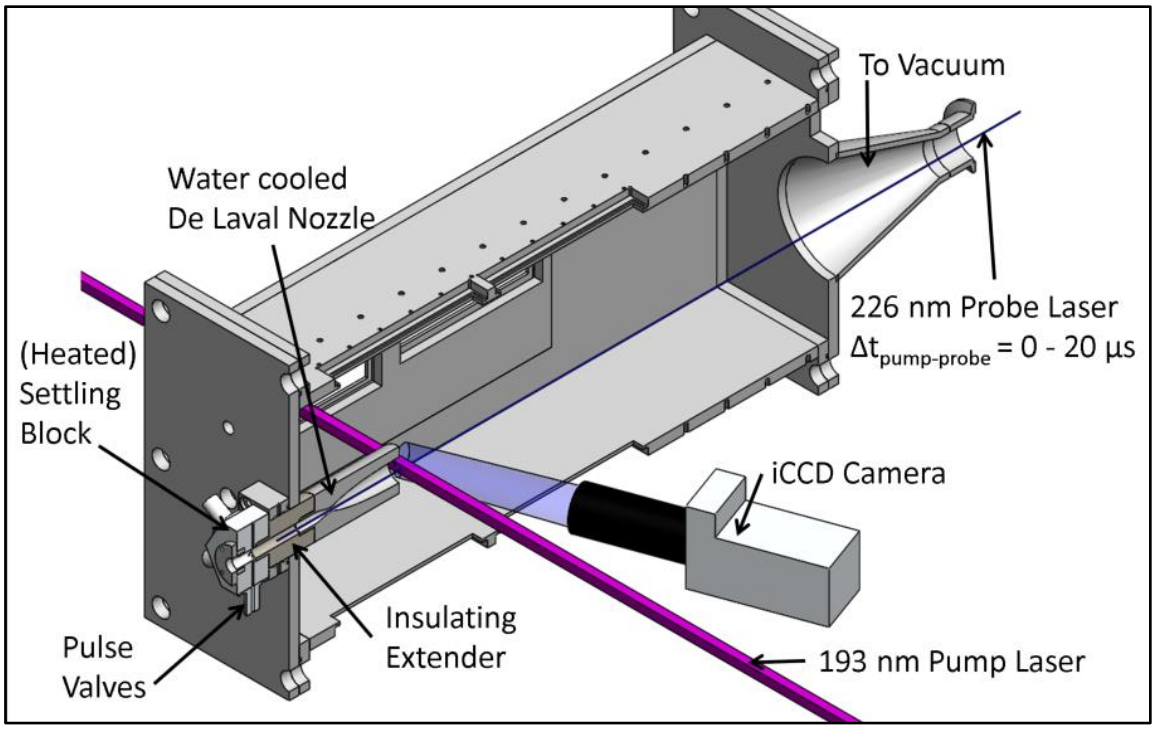

FIG. 17. Schematic diagram of the rPHT cell.

FIG. 18. Photo of the rPHT cell.

The rPHT instrument's main chamber had a total volume of 40 dm^3 and was evacuated using a Leybold D65B backing pump and a Ruvac WS1001US Roots blower assembly. The chamber was equipped with UV grade fused silica windows that provide optical access for diverse laser excitation and fluorescence collection configurations. In order to ensure that there was a very low concentration of C_6H_6 near the cell windows so that C_6H_6 adsorption and burning onto the windows was minimized, a N_2 purge "shower head" was constructed out of an approximately 8 cm diameter coil of 0.635 cm

copper tubing with holes drilled into the coil such that N_2 gas was sprayed toward the center of the coil in the direction of the window, such that the "shower head" created a gradient starting with no C_6H_6 in the area near the window where the pump laser entered the cell to normal cell conditions.

Pulsed flow operation was achieved in the rPHT by radially supplying the $N_2/NO/C_6H_6$ gas mixture to a settling chamber volume using either multiple pulse valves (Parker Pulse Valve Type Series 9) or multiple high performance 1600cc flow matched fuel injectors (DENSO Type 0426US1600) controlled by custom-made multi-channel valve driver circuits designed to produce externally triggered flow pulses of variable duration between 2 and 20 ms.

The settling block or the tubing leading to the settling block could be controllably heated by heating tape (BriskHeat Type BIH051100L) plugged into variable autotransformers (Staco Energy Products Co. Type 3PN1010) and insulated with DMCS treated glass wool (Ohio Valley, Catalog No. 3352) and aluminum foil. This allowed for controlled heating of the gas entering the rPHT cell.

Five axisymmetric converging-diverging nozzles made of aluminum, with Mach numbers of M = 2.46 ± 0.02, 2.91 ± 0.01, 3.82 ± 0.01, 4.87 ± 0.01, and 6.20 ± 0.02 were used to generate flows at temperatures of 133.0 ± 1.2, 109.1 ± 0.7, 75.0 ± 0.4, 51.2 ± 0.3, and 33.8 ± 0.3 K, respectively, given a constant settling chamber temperature of 294 ± 1 K. Photos of two nozzles are shown in Figure 19.

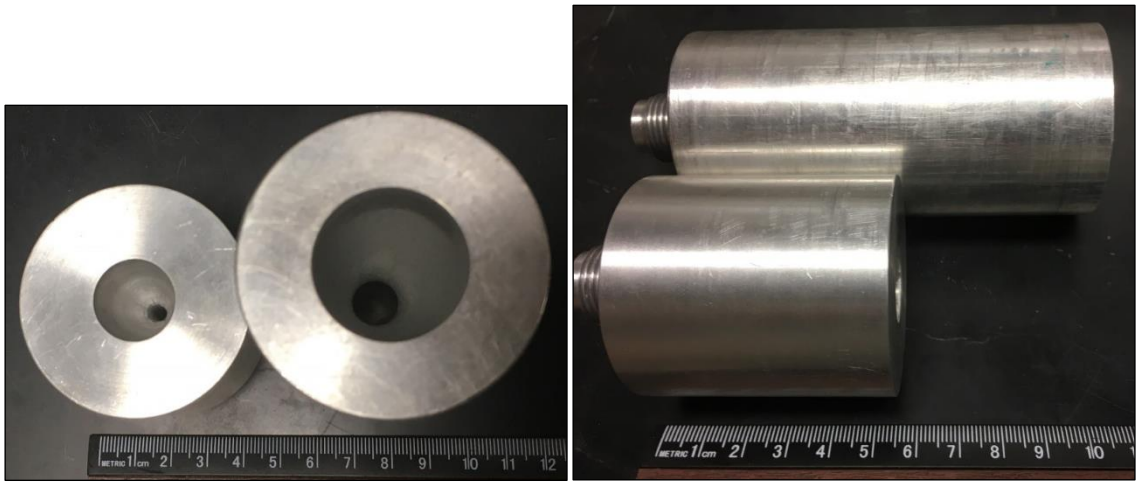

FIG. 19. Photos of M = 4.8 and M = 2.9 nozzles.

The flow temperatures achievable by each nozzle could also be increased by heating the gas in or before the settling chamber.

$$\frac{T}{T_{sett}} = \left(1 + \frac{\gamma - 1}{2} M^2\right)^{-1}, \tag{26}$$

Where M is the exit Mach number, T is the gas temperature at the nozzle exit, γ is the heat capacity ratio C_p/C_v, and the subscript *sett* indicates conditions in the settling region. The nozzles were designed using the method of characteristics accounting for boundary-layer displacement effects.[89] In order to avoid growth of boundary layer thickness due to heating of the nozzle when the backing region or settling region gas was heated, the nozzle temperature was maintained at room temperature. Nozzle temperature was maintained by extending the settling region with an insulating insert made from a 5.08 cm diameter PEEK rod and also by pumping room temperature distilled water from a five-gallon bucket reservoir through a 0.635 cm copper tubing coil that was wrapped

around the nozzle multiple times and secured with stainless steel worm-drive hose clamps (Breeze type 100 40H) to ensure good thermal contact. The pump used for this was a submersible fountain pump (Pumponics type PP53016).

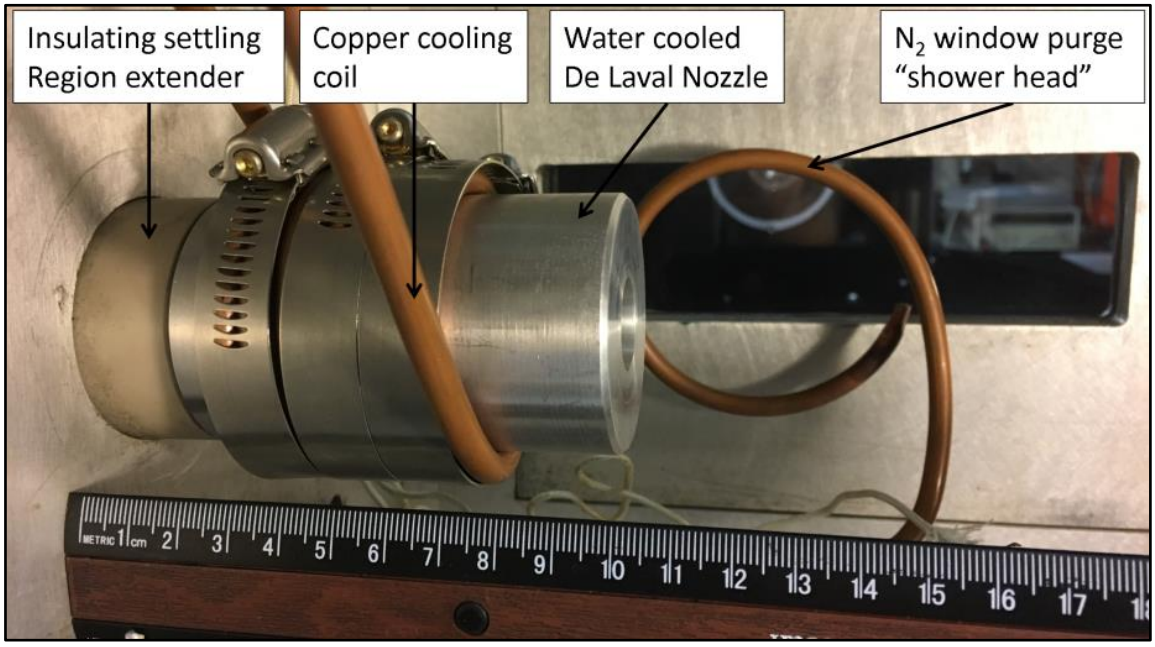

FIG. 20. Cooling coil secured to extended nozzle.

Pressure in the rPHT cell was matched to the nozzle exit pressure by adjusting a needle valve controlling the flow rate of N_2 gas emitted from the N_2 window purge "shower head" into the rPHT cell. The gas flow pulse temporal characterization for each nozzle was performed using two calibrated fast response pressure sensors, one located in the settling chamber region upstream of the nozzle throat (Endevco 8540-100 absolute piezoresistive sensor) and the other flush-mounted into the tip of a Pitot tube (Kulite

XCEL-100-5A) that was positioned at the center of the nozzle exit. The transducers, statically calibrated before nozzle characterization, were supplied with a 10 V DC excitation voltage and their signals amplified to a 10 V full-scale signal by a signal conditioner unit (Endevco model 136). The outputs from the signal conditioner were sampled at 35 kHz using a 16-bit data acquisition board (National Instruments PCI-6221). The typical flow pulse duration was set to ~8 ms. The pressure at the nozzle exit varies by less than 1% during the uniform flow intervals, corresponding to temporal fluctuations in temperature within 1%.[90, 91] The spatial uniformity of the flows generated by the nozzles was characterized by vertically translating the Pitot tube across the nozzle exit. Additional spatial characterization of these flows has been performed previously using NO planar laser induced fluorescence (PLIF) measurements.[90, 91] The resulting nozzle exit pressure surveys revealed uniform core flow conditions at the nozzle exit for at least 50% of the exit diameter for all nozzles, corresponding to uniform axisymmetric flows with diameters exceeding 1.27 cm.

The gas flow undergoes a gradual and adiabatic expansion along the nozzle centerline, and thus the exit flow properties such as pressure, density, and temperature can be described by isentropic flow relations.[89] Consequently, following characterization of the nozzles, the flow pressure and temperature conditions at the nozzle exit, in absence of any condensation of gas species in the nozzle, are only determined by the input conditions upstream of the nozzle throat and by the Mach number, as indicated in Equations 26 and 27.

$$\frac{P}{P_{sett}} = \left(1 + \frac{\gamma - 1}{2} M^2\right)^{\frac{-\gamma}{\gamma - 1}}, \tag{27}$$

Where M is the exit Mach number, P is the gas pressure at the nozzle exit, γ is the heat capacity ratio C_p/C_v, and the subscript *sett* indicates conditions in the settling region. A plot of the ratios of many nozzle properties vs Mach number is shown in Figure 21.

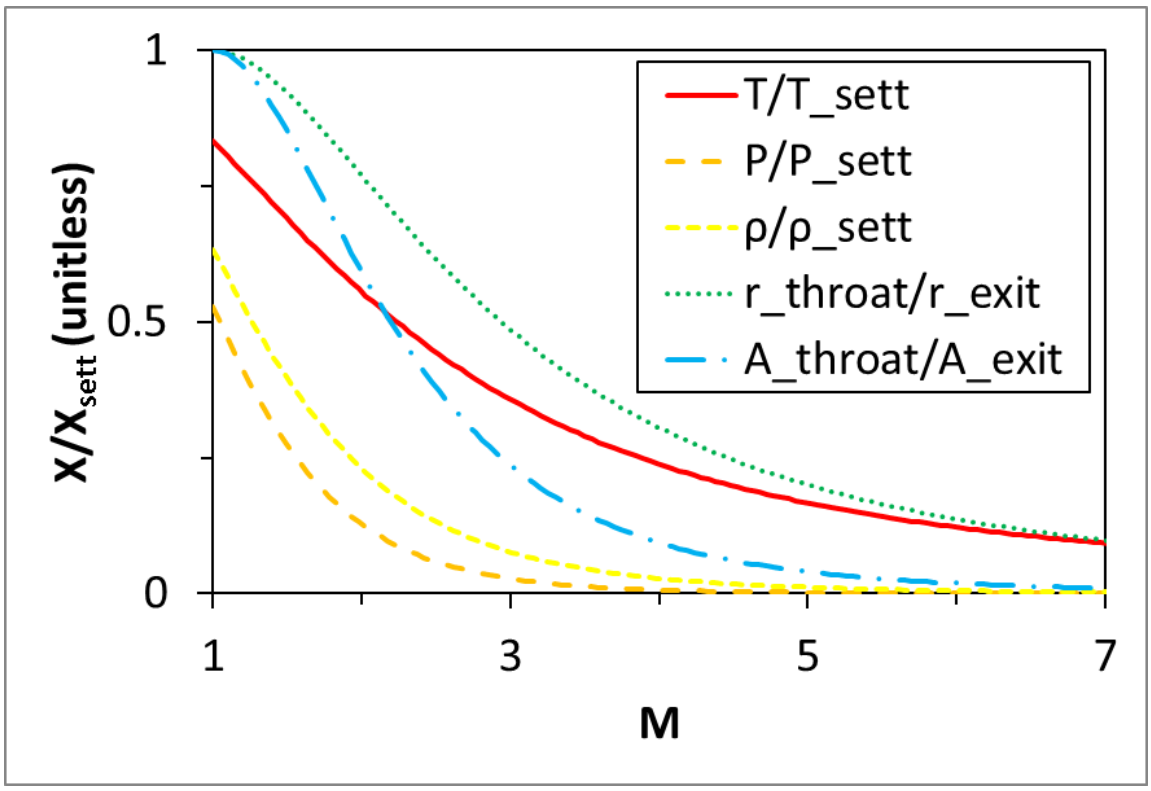

FIG. 21. Plot of the ratios of nozzle properties vs Mach number where T is temperature, P is pressure, ρ is density, r is radius, A is area, and *sett* denotes properties in the settling region.

During nozzle operation, the settling chamber temperature was monitored by a type K thermocouple and the pressure was recorded for each flow pulse by the fast-response pressure sensor. The exit flow pressure and temperature conditions were determined based on the pressure and temperature conditions measured in the settling chamber region.

When large fractions of NO (~50% NO) or moderate fractions of C_6H_6 (~1%) were utilized in experiments in the rPHT, it was necessary to consider how factors like differences in the heat capacities of the gas mixture and the formation of dimers, higher order oligomers, and clusters affected properties of the flow fields generated by the de Laval nozzles. If the ratio of the heat capacities, *γ*, of the mixture change, then the Mach number of the flow field will also change and the usual methods of characterizing the flow field with a pitot probe can be utilized to verify the new flow field properties.[90, 91] However, if a significant amount of condensation to form dimers, higher order oligomers, or clusters occurs in the nozzle, then the boundary layer thickness changes and also the gas temperature within the nozzle increases due to heat release associated with condensation.[92] Furthermore, the flow field no longer behaves as an ideal gas when condensed benzene passes through the shock wave in front of a pitot probe making the standard method of characterizing the flow field with a pitot probe too difficult since the rate of dimer formation in a cold N_2 flow field has not yet been reported. Therefore, for all experiments with benzene in the flow field, the flow field has been characterized with NO LIF. The flow temperature was characterized by fitting NO LIF scans to LIFBASE

simulations.[81] Then, the density of the flow field was characterized by measuring the low temperature rate of NO LIF decays while varying the concentration of NO in the flow field between 1-40% and solving for the slope of the plot of NO LIF decay rate vs concentration of NO, given Equation 22. From this pressure and temperature data from the settling region and flow field, a modified nozzle Mach number can be calculated.

The pulsed flow, the laser system trigger, the MCPPMT gate timing, and the iCCD gate timing were controlled using a digital delay/pulse generator (Berkeley Nucleonics Corporation 575-8C) with an RMS jitter of 50 ps. The Mach 2.46, 2.91, 3.82, and 4.87 nozzles were operated at 1 Hz, whereas the Mach 6.20 nozzle was operated at 0.5 Hz due to higher mass flow and pumping capacity requirements.

NO LIF scans were performed by triggering the laser to probe during the stable portion of each flow pulse and the integrated relative peak intensities were used to provide further confirmation of fluorescence being collected from the cold core flow at the expected temperature consistent with the nozzle Mach number. For comparison, triggering the probe laser after the flow pulse resulted in integrated relative absorption intensities consistent with gas mixtures at room temperature (294 K). The experimental LIF scans were compared against the LIFBASE spectral simulation program.[81]

Summary

The instrumentation utilized to characterize benzene LINE has been discussed. All instruments consisted of a gas mixing section, a vacuum chamber for flow field generation, a pulsed laser to initiate the experiment, and a pulsed laser to measure

transient bath temperature. The vacuum chamber utilized for bath gas initially at room temperature was a slow flow cell. The vacuum chamber utilized for bath gas initially below room temperature was the rPHT cell that cooled the gas by pulsing it through a de Laval nozzle. These instrumental setups allowed for the characterization of benzene LINE in a diverse set of initial bath conditions.

CHAPTER III

LIF TEMPERATURE MEASUREMENT METHODS*

Making accurate and precise temperature measurements are critical for the proper characterization of benzene LINE in experiments described in this dissertation. This chapter describes methods for minimizing systematic error in these measurements. When making temperature measurements with LIF, there are many factors that can influence the precision of the measurements. During the collection of temperature data, it is important to monitor and account for experimental drift, proper digitization of LIF decays, background emission signals, and, in the case of collection of temperature scans, the drift of dye laser stepper motors that can change the wavelength calibration. Overall, it is best to make measurements that are faster (less averaged) than the time scale of experimental drift in order to avoid experimental factors influencing trends in temperature measurements. These fast measurements can be collected in a data set that can be collected multiple times so that the data sets can be averaged at the end of the experiment. In this case, any data corrections and temperature fitting can be automated so that each data set can be monitored for errors or extreme experimental drift while the next data set is being collected.

---

* Reprinted in part from N. A. West, J. D. Winner, R. D. W. Bowersox, and S. W. North. Resolving the Energy and Temperature Dependence of C6H6* Collisional Relaxation via Time-Dependent Bath Temperature Measurements, The Journal of Chemical Physics **145**, 014308 (2016). with the permission of AIP Publishing.

Experimental Considerations

Drift/Experimental Design

When designing a temperature rise experiment, it is important to consider how drift in experimental conditions can affect the experimental data. Factors like drift in room temperature and drift in laser power can affect measured bath temperatures. Therefore, it is important to take precautions in order to see when experimental drift is affecting data and to remove the systematic effects that drift can have on trends extracted from data. One precaution to take is to randomize the order of pump-probe time delays utilized while making a set of temperature measurements so that the drift will show up as random noise in the data set instead of a systematic drift in a plot of the temperature vs pump-probe time delay. The data set can also be plotted vs run order to see if experimental drift has caused the results to drift up or down while the data was collected. Another precaution to take is to design the experiment such that an entire data set can be collected within one hour by taking faster, less averaged temperature scans. Scaling many such data sets to each other before averaging them together, instead of accumulating one data set for many hours, can help to avoid experimental drift influencing the analysis of results.

PMT vs iCCD

Temperature measurements can be made from integrating LIF signal from either PMT signal that has been digitized on an oscilloscope or from integrating LIF signal collected with an iCCD camera. Both methods have advantages and disadvantages and

it is often helpful to utilize both methods to diagnose experimental problems. One benefit of measuring temperature from integrated PMT traces is that the time dependent LIF signal can be viewed to see if factors like LIF quenching or emission from benzene at low pump-probe time delays are adversely affecting temperature scans. However, the only way to spatially measure temperature in a flow field with a PMT is to take a series of single point measurements where LIF from all other regions of the flow field are blocked from view of the PMT. If instead, an iCCD camera is utilized to Integrate LIF signal for temperature measurements, simultaneous spatially selective measurements are possible by comparing measurements from different pixel locations. However, in order to temporally resolve LIF decays with an iCCD camera, it would be necessary to make a series of measurements with a small LIF integration gate time that is shifted in time for each measurement.

Collecting LIF Decays with PMTs and Digitizing Signal with Oscilloscopes

When collecting LIF decays with a PMT for digitization with an oscilloscope there are many factors that can bias the measurement. First, it is important to scale the maximum value of the output signal of the PMT by adjusting the PMT gain in order to ensure that the PMT is not saturated. A saturated PMT will output signal with the wrong time dependence, which could make the time depencence of the signal change with shot-to-shot fluctuations in laser power. To estimate the maximum output voltage of a PMT for the collection of fluorescence decay signals, it is possible to utilize the maximum output current rating of a PMT, the combined 100 Ω resistance of a 50 Ω BNC cable and

a 50 Ω terminator, and Ohm's law (V=IR). As an example, the micro-channel plate photomultiplier tube (MCP-PMT) (Hamamatsu R5916U-50) has a rated maximum continuous output current of 110 μA and a maximum pulse peak current of 350 mA for 70 ps pulses. Therefore, the maximum output voltage for fluorescence decay collection is between 11 mV and 35 V. It was found that the optimal maximum voltage output for fluorescence decay collection is actually ~150 mV by comparing measurements of the intrinsic nitric oxide fluorescence decay rate to the accepted literature value for the intrinsic nitric oxide fluorescence decay rate.[79] If a PMT was saturated and yielded the inforrect time dependence for a fluorescence decay, this would bias the yielded value for the integration of the signal since a typical integration window is set in one scan such that the window starts after any laser scatter (~10 ns after the start of the decay) and ends about when the S/N < 1. This integration window is then used for all subsequent scans.

Another consideration is the digitization of the PMT signal with an oscilloscope. It is best to set the oscilloscope voltage scale such that the output of the PMT is maximized in the oscilloscope's voltage range (maximized on the oscilloscope screen) while leaving enough room for shot-to-shot fluctuations in initial LIF signal such that the signal never becomes larger than the voltage range plotted on the oscilloscope (the range of digitized voltages). It is important to do this when obtaining signal from the largest NO LIF peak that will be collected so that no peaks will have signal larger than the range that the oscilloscope will digitize. A simulation of an averaged, properly-collected

NO LIF decay digitized by a 12 bit, 2GS/s oscilloscope is shown in Figure 22 where 10 ns probe laser scatter starts at 50 ns and then NO LIF signal decays exponentially with a lifetime of 192 ns until the end of the oscilloscope trace.

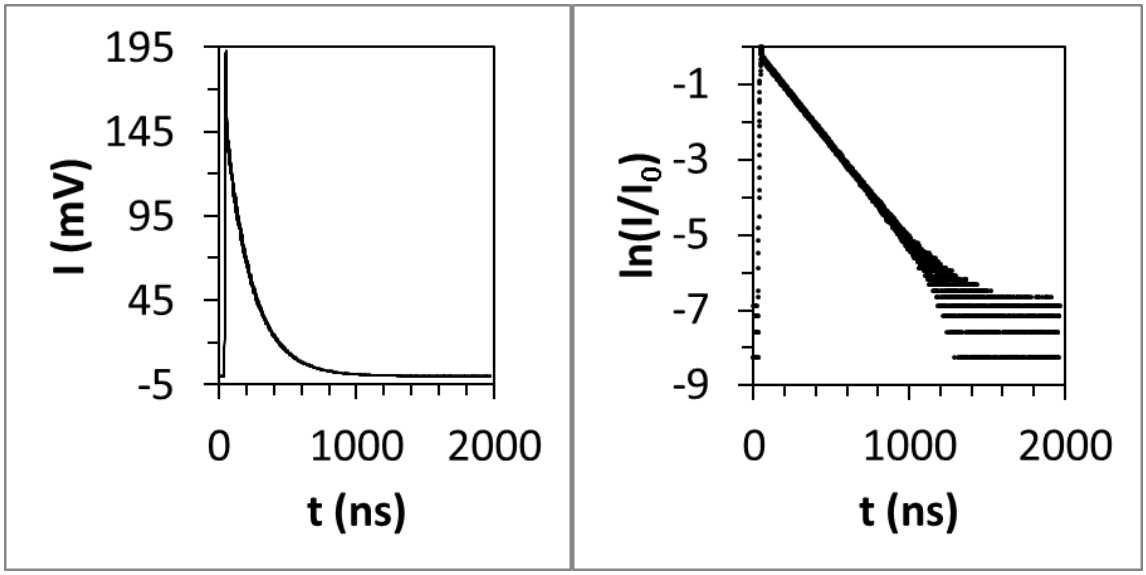

FIG. 22. Left: Simulated NO LIF decay signal digitized by a properly configured 12 bit, 2 GS/s oscilloscope. Right: Demonstration of linear and non-linear regions of the NO LIF decay on the left caused by digitization limits of the oscilloscope.

The natural log plot in Figure 22 (Right) demonstrates that a good integration window can be chosen when this plot is linear after the scatter. Therefore, the integration window would start at ~60 ns and end when the digitization of the signal biases the linearity of the natural log plot at about 1100 ns since there is not enough noise in this plot to warrant setting the integration window to a time less than 1100 ns. However, the

signal intensity will change if the temperature changes or if measuring other peaks, so it is necessary to set the integration window ending time to much less than 1100 ns since lower intensity LIF decays suffer from digitization error at much shorter time delays as shown in Figure 23.

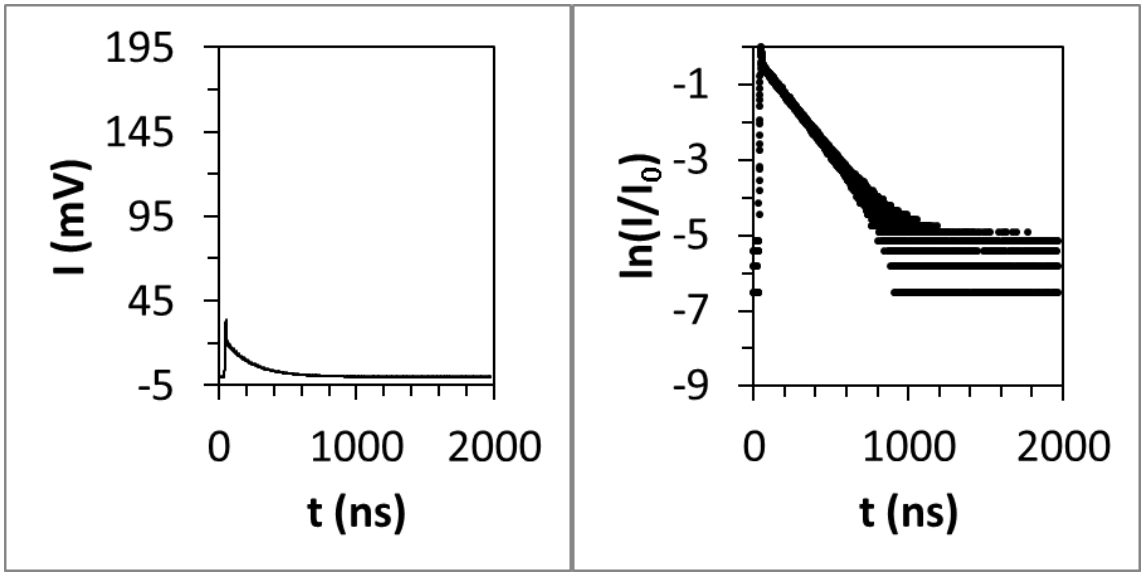

FIG. 23. Left: A simulated low intensity NO LIF decay signal digitized by a properly configured 12 bit, 2 GS/s oscilloscope. Right: Demonstration of linear and non-linear regions of the NO LIF decay on the left caused by digitization limits of the oscilloscope.

Since the onset of digitization error occurs at shorter times for lower intensity signal it is prudent to set the end value for the integration window to less than about two lifetimes of the LIF decay after the start of the decay. This also demonstrates that in order to obtain good temperature measurements it is best to increase PMT gain in between data

sets when the dye laser power drops over the life of the laser dye and also it is best to replace laser dye in between data sets if probe laser power becomes too low during an experiment.

As a final example of the difficulties associated with digitization of LIF decays, a low intensity decay that has been quenched to have a lifetime of 50 ns is plotted in Figure 24.

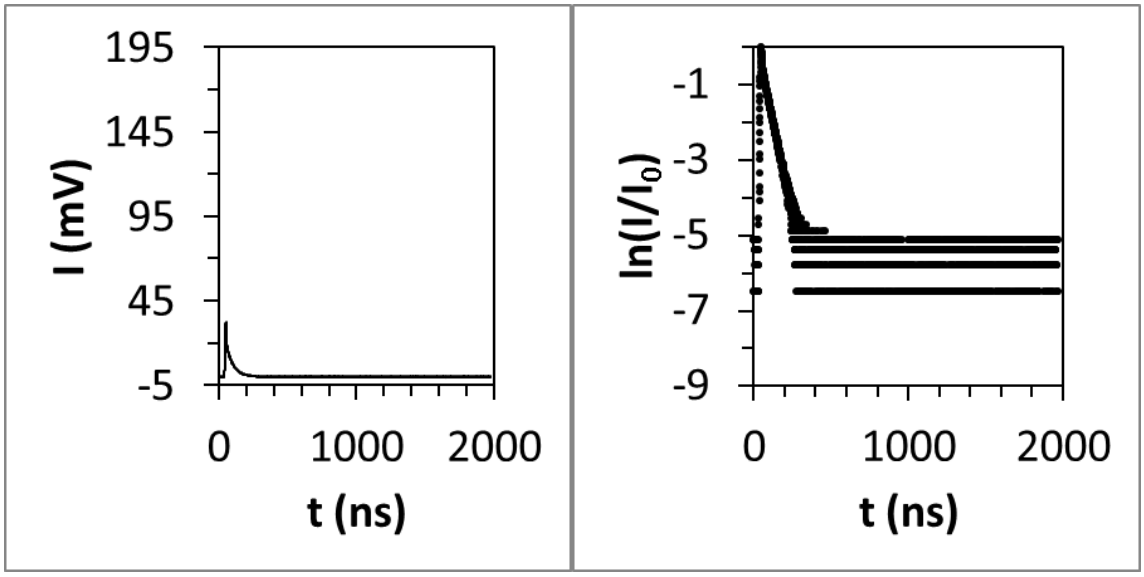

FIG. 24. Left: A simulated low intensity quenched NO LIF decay signal digitized by a properly configured 12 bit, 2 GS/s oscilloscope. Right: Demonstration of linear and non-linear regions of the NO LIF decay on the left caused by digitization limits of the oscilloscope.

A decay that has a 50 ns lifetime only yields less than 100 ns (or 200 data points for a 2GS/s oscilloscope) of useful points to integrate. Therefore, it is important to keep in

mind that there is a decrease in S/N at lower temperature and higher pressure that is the result of increased quenching of LIF decays.

Collecting and Digitizing LIF Signal with an iCCD Camera

The considerations for digitizing and integrating LIF signal on an iCCD camera are similar to the considerations for collecting LIF signal with a PMT and digitizing it with an oscilloscope. First, the maximum signal from the largest LIF peak should be maximized in the possible range of signal measured by the iCCD camera by adjusting the gain of the iCCD camera in order to not saturate the iCCD camera. Second, the integration gate on the iCCD camera should be set to the same integration window suggested for integration of PMT signal digitized on an oscilloscope. However, since it is not possible to determine the time dependence of the LIF decay with a single measurement (unlike with a single PMT measurement), it is best to measure a LIF decay with a PMT/oscilloscope in the region of interest or to calculate an estimated LIF lifetime if the quenching behavior of the flow field is known in order to determine the optimal time width for the iCCD camera gate. Also, since an iCCD camera can simultaneously spatially resolve integrated LIF decays originating from different regions of a flow field, it is important to estimate the integration gate time width in the region of the flow field that is most greatly affected quenching.

Single Laser Scans and Two-Line PLIF

LIF based temperature measurements utilizing either PMT/oscilloscope integrated signal or iCCD integrated signal can be acquired via both fits to LIF scans and

fits to two-line LIF data. Both methods have advantages and disadvantages, especially if experiments are carried out with only one probe laser as was the case for all experiments in this dissertation. One major advantage of two-line LIF is that temperature measurements can be carried out with higher temperature sensitivity at a faster rate than for LIF scans. two-line LIF has higher temperature sensitivity because the two most sensitive transitions for measuring temperature for a specific temperature range are utilized and the laser is situated at the maxima of each of those peaks during all measurements. By contrast, the temperature sensitivity of LIF scans is lower than that of two-line LIF because LIF scan data points vary in intensity as the wavelength is scanned from peak to peak and also regions of approximately zero signal are collected between peaks in scans. For example, if the S/N of the integrated fluorescence decay at the top of a rovibronic peak is 5 then the S/N would increase with the square root of the number of averaged measurements for a two-line PLIF measurement so that with averaging 10 measurements the S/N would increase to ~15.8. However, in a typical LIF scan in this dissertation, each peak of approximately gaussian shape was about 10 laser steps wide at 2σ width and each of the 10 measurements would have a varying S/N value. Therefore, the 10 measurements utilized to fit a gaussian peak would yield a total S/N of ~7.8 which is ~2 times less than the S/N from 10 measurements of a peak in the two-line PLIF method which would take the same amount of time to collect. One exception to the temperature measurement sensitivity of two-line LIF is if temperatures are measured in a range outside of where the two chosen lines are most sensitive. It is possible that

scans can incorporate multiple transitions that are more sensitive to temperature measurements over a much larger range of temperatures than can be accomplished with the two-line LIF method.

Two-line LIF temperature measurements are faster than LIF scan measurements because half of a two-line LIF data set, the integrated signals for all pump-probe time delays for one transition, can be collected without changing the laser wavelength, after which the laser wavelength is changed to the other transition where this process is repeated in order to finish the set of measurements. This allows for minimal time spent changing the probe laser wavelength. By contrast, the time it takes to change the wavelength of the probe laser in LIF scans causes an increase in time per temperature measurement as compared to the two-line LIF method.

One advantage of LIF scan temperature measurements over two-line LIF measurements is that scans do not need to be calibrated at a known temperature. This is important for checking the calibration of two-line LIF temperature measurements with LIF scan temperature measurements as sometimes regions of flow fields can behave in ways that are different than predicted by the theory behind the two-line LIF temperature measurement method, for example, when the flow fields are perturbed by condensation. In such a case, multiphoton effects were observed when measuring LIF signal vs probe laser power and these effects caused distorted temperature measurements.

Benzene Emission Removal from NO LIF Measurements

At the lowest pump-probe time delays in temperature rise measurements there is benzene emission that needs to be accounted for in both LIF scans and two-line LIF data. The benzene emission adds to the integrated signal and it has large shot-to-shot fluctuations since benzene emission is quadratically dependent on pump laser power which varies due to shot-to-shot laser power fluctuations. Therefore, any fluctuations in benzene emission that are not removed from integrated NO LIF signal utilized for temperature measurements will result in fluctuations in temperature measurements.

When removing benzene emission from two-line LIF measurements, it is best to take duplicate measurements of each integrated signal with the probe laser blocked so that this benzene emission integrated signal can be subtracted from two-line LIF measurement integrated signal. This works best if the integrated signals are the accumulation of multiple laser shots to minimize the shot-to-shot fluctuations. Any unremoved benzene emission will scale the calibration factor of two-line LIF measurements and distort temperature measurements so it is most important to remove benzene emission from the lowest pump-probe time delay data where benzene emission signal is the largest, up to ~33% of the total integrated signal in the lowest pump-probe time delays implemented in experiments in this dissertation.

In LIF scans, benzene emission results in an increase in baseline signal. If the pump laser power was constant throughout the scan, the baseline can be fit and subtracted from the LIF scan without separately collecting and subtracting benzene

emission integrated signal. However, if the pump laser power drifted throughout a scan, there will be a slope(s) in the baseline and it will be necessary to remove integrated benzene emission signal from each wavelength point separately. Either way, it is important to apply any probe laser power corrections after correcting for benzene emission since any benzene emission would distort the probe laser power correction and result in distorted temperature measurements.

NO LIF Temperature Fitting Methods

Boltzmann Plot Temperature from Scans

Obtaining a fit to the rotational temperature from a Boltzmann plot relies on the rearrangement of the rotational Boltzmann equation to obtain Equation 28.

$$E_{rot}(J) = -k_B ln\left(\frac{N_J}{g}\right) T_{rot}, \tag{28}$$

Where E_{rot} is the energy of rotational state J, k_B is the Boltzmann constant, N_J is the relative population of state J, g is the rotational degeneracy ($2J+1$), and T_{rot} is the rotational temperature. Therefore, the rotational temperature can be determined from the slope of a Boltzmann plot which plots $k_B ln(N_J/g)$ vs the rotational energy of each state as shown in Figure 25.

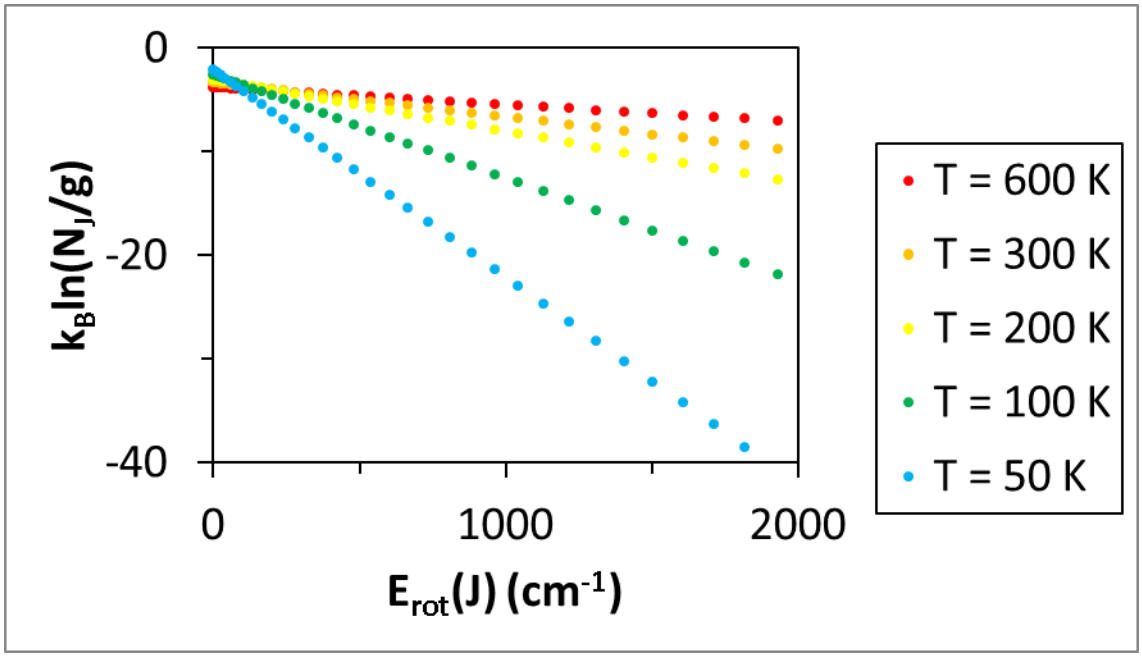

FIG. 25. Simulated Boltzmann plot for nitric oxide.

Since the relative populations of each state *J* is proportional to the area under the corresponding peak in a LIF scan, scans over transitions originating from many different rotational states can be utilized to determine the rotational temperature. Therefore, a program called "Scan_Laser_And_Fit_T_Rot.vi" was written to fit the scan peaks as sums of Gaussian functions in order to determine the relative population of each rotational state. The program "Scan_Laser_And_Fit_T_Rot.vi" utilizes a fitting algorithm, the LabVIEW Levenberg-Marquardt constrained non-linear curve fit algorithm, to fit a Gaussian function for each selected peak in a spectrum given gaussian parameter constraints and guesses have been input to the program. A step-by-step description of

how to use the program is given in Appendix A. An example fit of 8 peaks in a spectrum is shown in Figure 26.

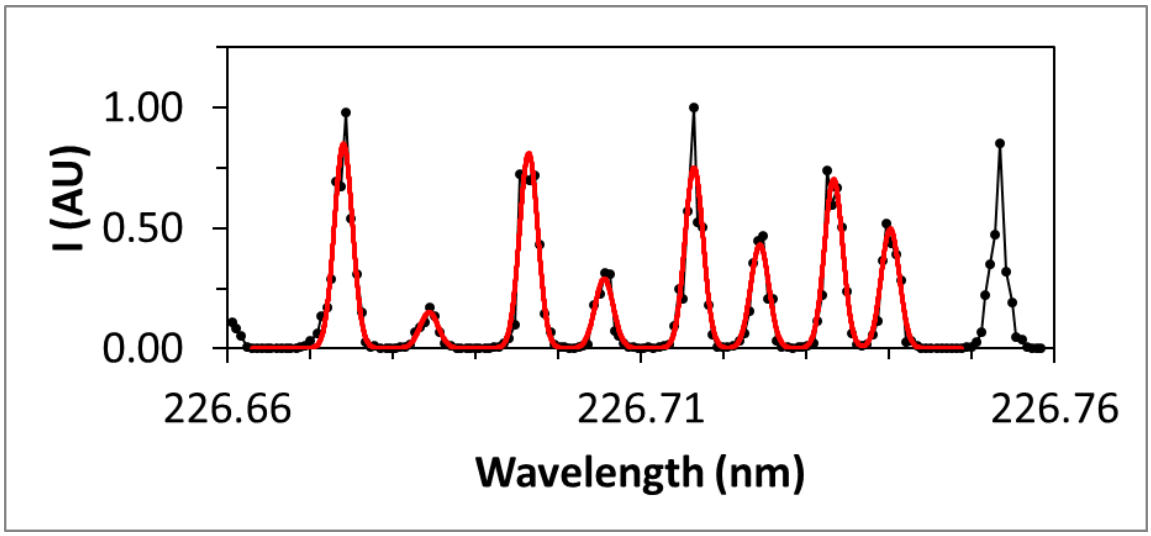

FIG. 26. The scan (black circles/curve) has been fit with 8 Gaussians (red curve).

The relative area under each Gaussian is proportional to the width multiplied by the height of the Gaussian or, if the widths of the Gaussians are constrained, just the heights may be compared. The corresponding relative population can then be derived from the area under each peak if multiplied by a branch-specific correction factor obtained from the LIFBASE database.[81] The program "Scan_Laser_And_Fit_T_Rot.vi" therefore calculates the correction factor for each peak and obtain the relative population of each *J* state for making a Boltzmann plot. A temperature value is then determined from the slope of the Boltzman plot by utilizing Equation 28. This temperature fitting process is

automated in the program “Scan_Laser_And_Fit_T_Rot.vi” such that after one scan has been fit, a set of scans over the same region can be shifted to each other with a least-squares based wavelength shift-determining algorithm and a temperature value obtained from each of the scans in the set of scans.

One last feature of the temperature fittting program “Scan_Laser_And_Fit_T_Rot.vi” that was utilized to verify the Boltzmann plot fits of NO LIF scans was the shifting of all of the scans to the wavelengths reported for the peaks in the LIFBASE program.[81] This was accomplished by comparing the assigned peak locations in an exported database from LIFBASE to the fit peak locations that correspond to the center of each fit Gaussian function. A linear fit to the shift of each peak from LIFBASE vs the peak position determined from the Gaussian fit was utilized for each scan to shift and stretch the wavelength values of experimental scans to match the true wavelength values. This method corrected for small errors in the wavelength calibration of the dye laser.

LIFBASE Fits vs Boltzmann Plot Fits

Since Boltzmann plot temperature fits are biased most strongly by high and low energy rotational states, states to which that the slope of a Boltzmann plot are most sensitive, experimental scans can be compared to LIFBASE simulations at the temperature fit by the Boltzmann plot to check for bias. Alternatively, the temperature of LIFBASE simulations can be tuned to best fit the experimental data, and the LIFBASE fit temperature can be compared to the Boltzmann plot fit temperature. In order to

obtain a best fit temperature from LIFBASE simulations, a series of LIFBASE simulations should first be made for small increments in temperature near the Boltzmann plot temperature. Then the simulations and the shifted scan need to be regridded so that they have the same number of data points at the same wavelengths. This can be accomplished by interpolation of scan data points as long as the regridded scan has approximately the same or fewer data points than the original. Next, all scans need to be normalized. Then a least squares analysis can be performed between the normalized scan and the normalized LIFBASE simulations to determine the best fit LIFBASE scan.

Summary

The focus of Chapter III was to describe considerations for designing experiments to accurately measure N_2 bath transient temperature rises via NO LIF. Experimental considerations for avoiding error due to drift in experimental conditions as well as methods of integration of digitized signal from either a PMT or iCCD camera were discussed. Then, methods of automating the fitting of NO LIF scans for the determination of bath temperature values was discussed. Overall, the ability to quickly collect accurate NO LIF scans and to fit the scans for temperature measurements while conducting experiments allowed for the development of a method to characterize the collisional relaxation of highly vibrationally excited benzene which allowed for the development of a benzene LINE technique.

CHAPTER IV

MULTIWELL MODELING*

The benzene LINE technique relies on the ability to predict the collisional relaxation of highly vibrationally excited benzene in a gas flow field. Since benzene was not probed directly in this dissertation, a method for simulating the collisional relaxation of benzene and converting it to a simulated bath temperature rise was necessary in order to obtain benzene CET rate information from fits to bath transient temperature measurements. Therefore, the MultiWell master equation program was utilized to model the collisional relaxation of benzene and the bath heat capacity was integrated in order to yield simulated bath temperature rises. Chapter IV describes the method utilized to simulate bath temperature rises for all experiments that were conducted to characterize benzene LINE in this dissertation.

Master Equation Modeling Theory

The time-dependent evolution of internal energy of non-reacting vibrationally excited molecules can be modeled using the master equation formulation:

* Reprinted in part from N. A. West, J. D. Winner, R. D. W. Bowersox, and S. W. North. Resolving the Energy and Temperature Dependence of C6H6* Collisional Relaxation via Time-Dependent Bath Temperature Measurements, The Journal of Chemical Physics **145**, 014308 (2016). with the permission of AIP Publishing.

$$\frac{dy(E',t)dE'}{dt} = \int_0^\infty [R(E',E)dE'y(E,t)]dE - \int_0^\infty [R(E,E')dE'y(E',t)]dE, \quad (29)$$

where *y(E',t)dE'* is the concentration of molecules with energy between *E'* and *E' + dE'* and *R(E,E')* is the rate coefficient for V-RT CET from an energy between *E'* and *E' + dE'* to an energy between *E* and *E + dE*.[82, 83] The energy transfer rate coefficients *R(E,E')* can be expressed as:

$$R(E,E')dE = \omega P(E,E')dE, \quad (30)$$

where ω is the total inelastic collision rate, *P(E,E')* is the probability that a molecule initially at an energy between *E'* and *E' + dE'* will transition to an energy between *E* to *E+ dE*. The total inelastic collision rate can be approximated by the Lennard-Jones collision rate, Equation 31.

$$\omega = k_{coll} = \pi\sigma_{AB}^2 < v_r > \Omega^{(2,2)^*} N, \quad (31)$$

where σ_{AB} is the Lennard-Jones diameter, $<v_r>$ is the average relative speed, $\Omega^{(2,2)*}$ is the collision integral, and *N* is the number density.[16, 37] For calculations of the collision rate between $C_6H_6^*$ and N_2, the empirical collision integral for any two gas molecules, $\Omega^{(2,2)*}$, was taken to be:

$$\Omega^{(2,2)^*} = \frac{A}{(T^*)^B} + \frac{C}{e^{DT^*}} + \frac{E}{e^{FT^*}}, \quad (32)$$

where $T^*=k_BT/\epsilon_{AB}$, A = 1.16145, B = 0.14874, C = 0.52487, D = 0.77320, E = 2.16178, F = 2.43787, k_B is the Boltzmann constant, ϵ_{AB} is the Lennard-Jones well depth, and 0.3 ≤ T*

≤ 100.[93] Lennard-Jones parameters, σ_{AB} = 4.6 Å and ε_{AB}/k_B = 181.3 K were calculated utilizing Lennard-Jones parameter combination rules with C_6H_6 and N_2 Lennard-Jones parameters.[94] The Lennard-Jones collision rate model was used in this study for better comparison to trajectory calculations, even though it is known that the inelastic collision rate is higher than the Lennard-Jones collision rate at high vibrational density of states and lower at low vibrational density of states.[37, 54] Since the energy transfer rate is determined by both the inelastic collision rate and the probability of energy transfer function, our derived parameters for the probability of energy transfer function are only valid when using the Lennard-Jones collision rate.[37]

MultiWell Model Conditions

The collisional relaxation of C_6H_6* in a N_2 bath was modeled using the master equation formulation in the program MultiWell.[82, 83] The active K-rotor and the adiabatic 2-D rotor model was utilized in the calculation of C_6H_6* density of states. All energy transfer parameters derived in this dissertation are only applicable to this model since the density of states is used in the detailed balance calculation which changes the internal energy dependence of the CET rate. Exact counts of the densities of states were carried out with the Stein-Rabinovitch extension[95] of the Beyer-Swinehart algorithm.[96] The density of states is plotted vs benzene vibrational energy in Figure 27.

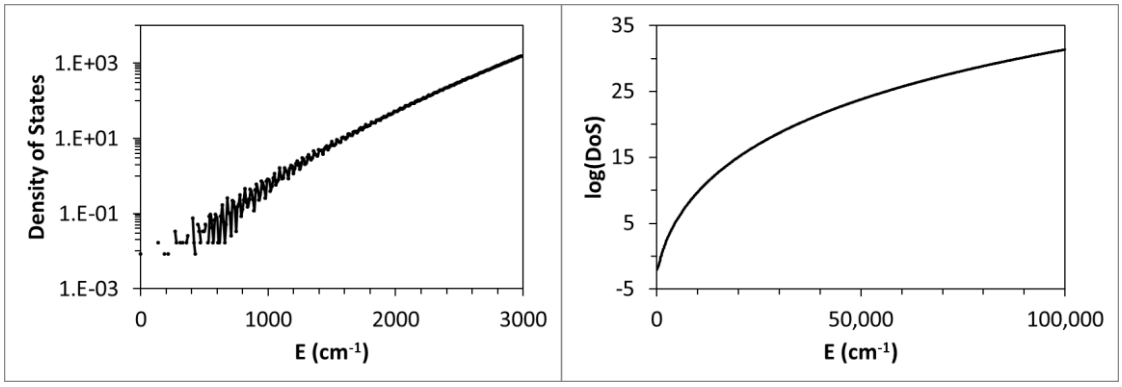

FIG. 27. Left: Low energy density of states of benzene up to 3,000 cm^{-1} of vibrational energy. Right: Whole energy range density of states of benzene up to 100,000 cm^{-1} of vibrational energy.

For the low energy range of the density of states, the plot on the left in Figure 27, the spacing between benzene vibrational states is large compared to the energy bin size used to count the density of states and some bins have zero states for the lowest energies. The sum of states generated from the density of states in Figure 27 is shown in Figure 28.

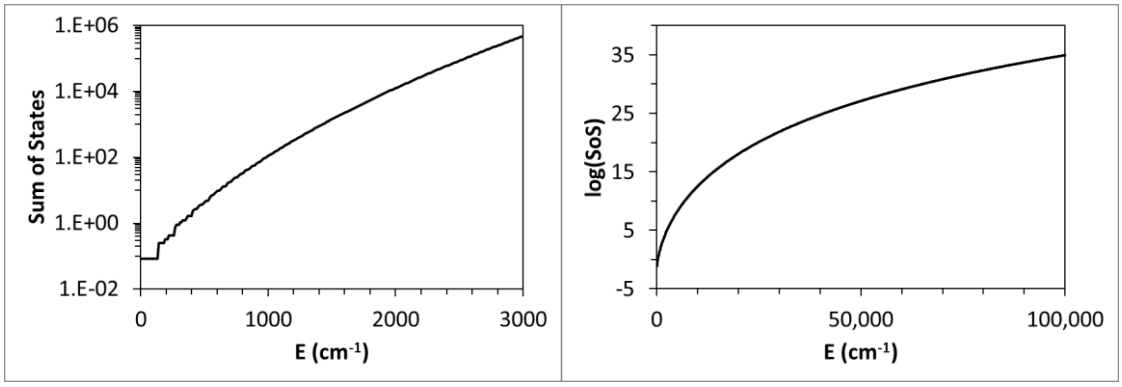

FIG. 28. Left: Low energy sum of states of benzene up to 3,000 cm^{-1} of vibrational energy. Right: Whole energy range sum of states of benzene up to 100,000 cm^{-1} of vibrational energy.

The C_6H_6 vibrational frequencies utilized in MultiWell calculations are shown in Table 4 and were obtained from Lenzer *et al.*[10]

TABLE 4. Benzene vibrational frequencies from Lenzer et al.[10]

Vibrational Mode	Symmetry	Energy (cm^{-1})
ν_1	A_{1g}	3057
$\nu_{2,3}$	E_{1u}	3057
$\nu_{4,5}$	E_{2g}	3059
ν_6	B_{1u}	3060
$\nu_{7,8}$	E_{2g}	1739
$\nu_{9,10}$	E_{1u}	1531
ν_{11}	A_{2g}	1376
ν_{12}	B_{2u}	1749
$\nu_{13,14}$	E_{2g}	1134
ν_{15}	B_{2u}	1173
$\nu_{16,17}$	E_{1u}	991
ν_{18}	B_{1u}	1026
ν_{19}	A_{1g}	926
$\nu_{20,21}$	E_{2g}	617
ν_{22}	B_{2g}	1070
$\nu_{23,24}$	E_{2u}	1015
$\nu_{25,26}$	E_{1g}	833
ν_{27}	B_{2g}	657
ν_{28}	A_{2u}	680
$\nu_{29,30}$	E_{2u}	400

The utilized C_6H_6 rotational moments of inertia, I_A = 177.8 amu Å (B_A = 9.481 cm^{-1})and I_B = I_C = 88.9 amu Å ($B_{B,C}$ = 0.1896 cm^{-1}), were obtained from Herzberg.[70] A single exponential form of *P(E,E')*, *N* = 1 and Y_1 = 1 in Equation 2, was used since the

temperature rise experiment was insensitive to the contribution of supercollisions to CET. However, when a large amount of energy is transferred into bath molecule rotational energy in a single collision it is possible to form a high energy metastable rotational state that may not thermalize on the same time scale as the rest of the bath.[97] Therefore, it is possible that the temperature rises measured in this dissertation underrepresent the total energy transferred from the excited benzene to the bath rotational energy.

In order to generate fits to experimental temperature rises, the simulated MultiWell plots of ensemble average benzene internal energy versus number of collisions were calculated and then converted to simulated temperature rises. An example of <Evib> vs number of collisions is shown in Figure 29 for bath T_0 = 140 K.

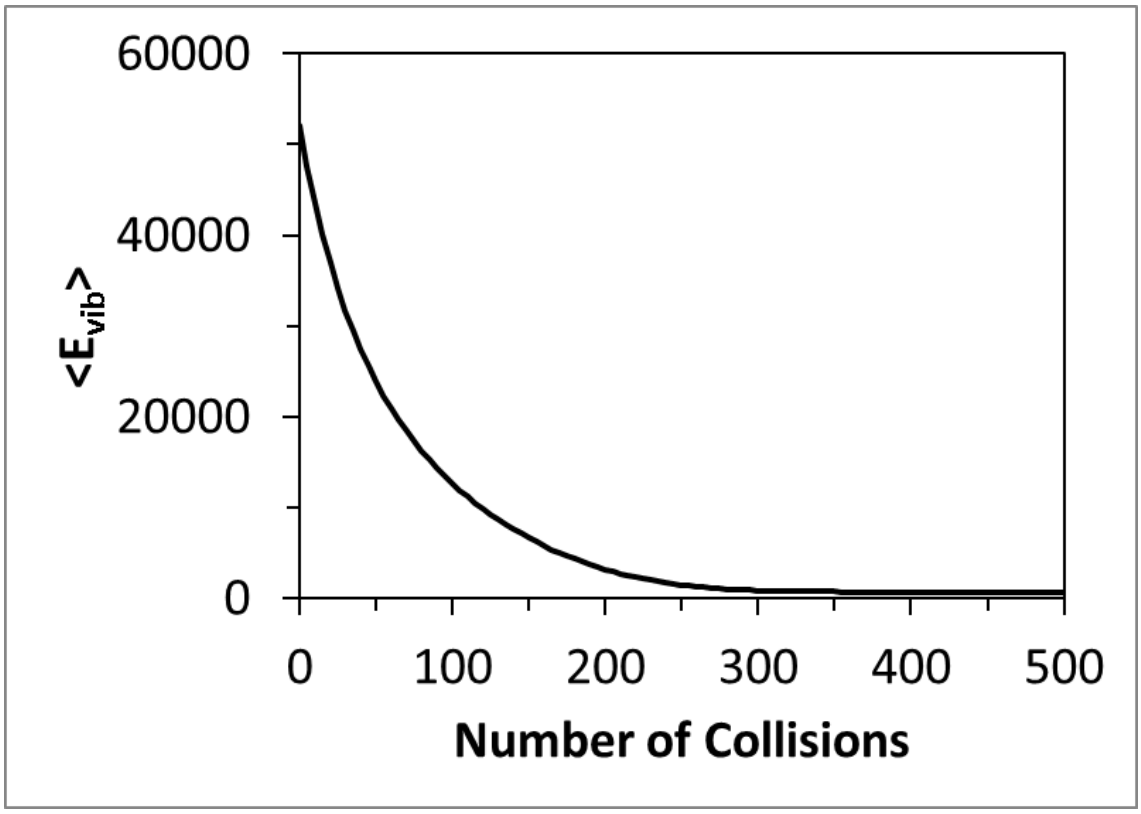

FIG. 29. Average vibrational energy vs number of collisions for an ensemble of 500,000 benzene molecule trajectories in a MultiWell simulation.

A plot of the ensemble distribution of vibrational energy vs number of collisions for the same simulation shown in Figure 29, is shown in Figure 30.

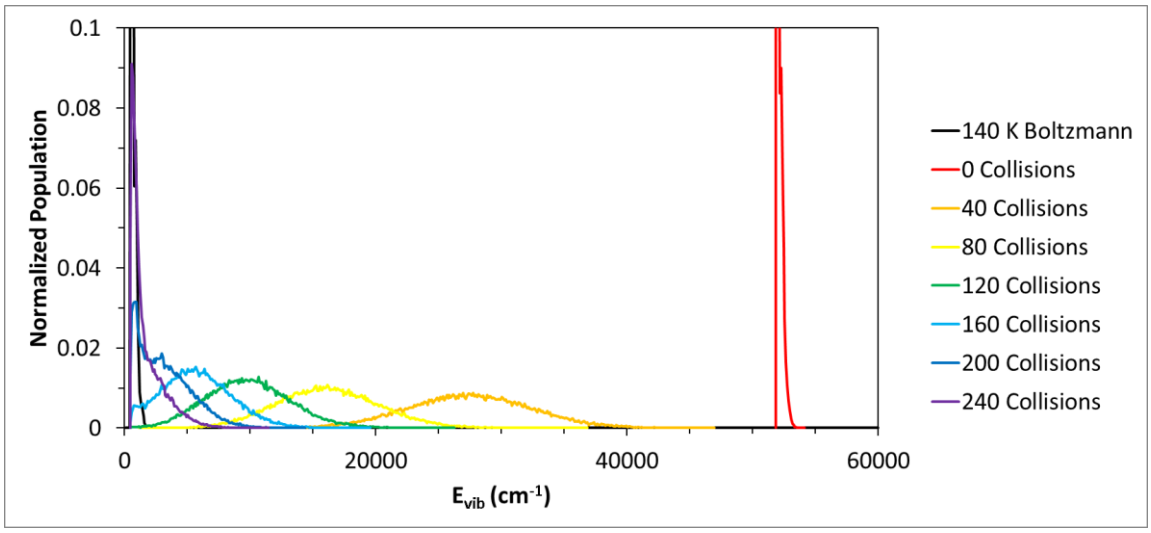

FIG. 30. Normalized vibrational energy distributions for 500,000 benzene molecules after various numbers of collisions in a MultiWell simulation. T_0 = 140 K.

In Figure 30 the initial distribution of vibrational energies is a 140 K Boltzmann distribution that is shifted by 51,813 cm^{-1}. Then, as benzene collisionally relaxes, the distribution broadens until about E_{vib} = 30,000 cm^{-1} where it begins to narrow and then eventually reach a thermalized distribution again.

Since previous studies of similar systems report predominantly V-RT CET and very little V-V CET to the bath, the energy lost from benzene was assumed to be transferred evenly into N_2 rotation and translation in the simulation.[16] To obtain simulated N_2 temperature values, the N_2 translational, rotational, and vibrational heat capacities were integrated to the temperatures that yielded the N_2 internal energies determined by the simulation. Two methods of determining the heat capacity of N_2: utilization of the

equipartition theorem and derivation of the heat capacity via differentiating partition functions.

$$C_V = \left(\frac{\partial E}{\partial T}\right)_V = -\left(\frac{\partial ln(Q)}{\partial \beta}\right)_V = k_B T^2 \left(\frac{\partial ln(Q)}{\partial T}\right)_V, \quad (33)$$

Where C_V is the heat capacity, E is energy, T is temperature, Q is the total partition function, $\beta = k_B^{-1}T^{-1}$, and k_B is the Boltzmann constant. Since the total partition function is the product of the partition functions of each type of molecular energy, $Q = (q_{electronic})(q_{vib})(q_{rot})(q_{trans})$, the total heat capacity can be written as the sum of the heat capacities of each type of molecular energy, $C_{V,tot} = C_{V,electronic} + C_{V,vib} + C_{V,rot} + C_{V,trans}$. For the equipartition theorem, the sum of the heat capacities is given by Equation 34 and Equation 35 for linear and nonlinear molecules respectively.

$$C_V(T) = 0 + mNk_B + Nk_B + \frac{3}{2}Nk_B, \quad (34)$$

$$C_V(T) = 0 + mNk_B + \frac{3}{2}Nk_B + \frac{3}{2}Nk_B, \quad (35)$$

Where m is the number of vibrational modes of the molecule in the high temperature limit and the $C_{V,electronic} = 0$ for most molecules around room temperature. In order to determine if a vibrational mode is in the high temperature limit the characteristic temperature of the mode should be compared to the temperature of the experiment.

$$\Theta_i = \frac{E_i}{k_B}, \quad (36)$$

Where Θ_i is the characteristic temperature of a mode i with energy E_i. If is $\Theta_i > 10T$ then the mode is said to be in the high temperature limit. For N_2, Θ_i = 3394.9 K since its fundamental vibrational frequency is 2358.57 cm^{-1}. Therefore, the vibrational mode of N_2 is not active for the range of temperatures, ~140 - 700 K, employed in experiments and simulations in this dissertation. This is shown to be mostly true when examining the vibrational component of the total heat capacity, C_V in Equation 37, derived from a statistical mechanics treatment.

$$C_V = \left(\frac{\partial E}{\partial T}\right)_V = -\left(\frac{\partial ln(Q)}{\partial \beta}\right)_V = k_B T^2 \left(\frac{\partial ln(Q)}{\partial T}\right)_V, \tag{37}$$

Where C_V is the heat capacity, E is energy, T is temperature, Q is the partition function, $\beta = k_B^{-1}T^{-1}$, and k_B is the Boltzmann constant. The partition function for a single vibrational mode is:

$$q_{vib} = \left(1 - exp(-\beta hcv)\right)^{-1} = \left(1 - exp(-\Theta_v/T)\right)^{-1}, \tag{38}$$

Where h is Planks constant and c is the speed of light. Incorporating q_{vib} into Equation 37 yields:

$$(C_V)_{vib,m} = \frac{k_B (hcv)^2 \beta^2 exp(\beta hcv)}{(exp(\beta hcv) - 1)^2} = k_B \left(\frac{\Theta_v}{T}\right)^2 \frac{exp(\Theta_v/T)}{(exp(\Theta_v/T) - 1)^2}, \tag{39}$$

If a molecule has multiple vibrational modes, the vibrational heat capacities of all individual modes can be summed to obtain the total vibrational heat capacity.

$$(C_V)_{vib\ tot} = \sum_{m=1}^{3N-5\ or\ 3N-6} (C_V)_{vib,m}, \tag{40}$$

A plot of the vibrational heat capacity for N_2 confirms that C_{vib} is nearly zero for N_2 below 700 K as shown in Figure 31 and then increases sharply toward the value predicted by the equipartition theorem until leveling off after the characteristic temperature of nitrogen's vibrational mode at Θ_i = 3394.9 K.

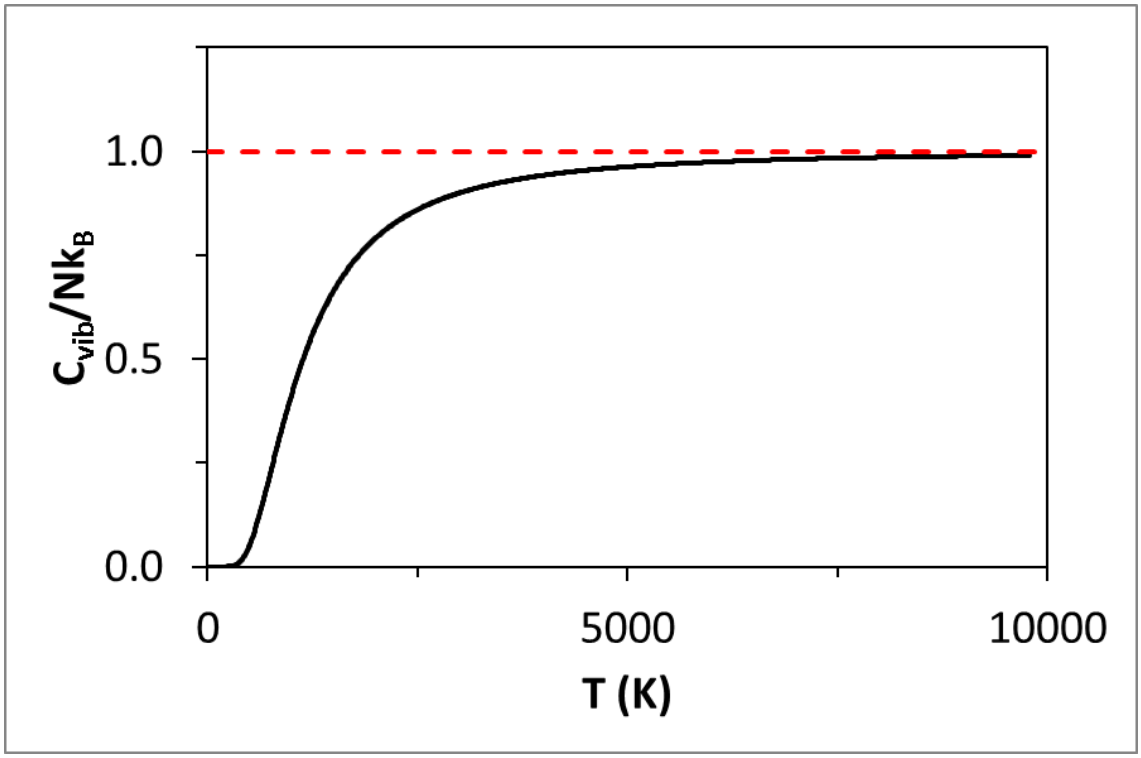

FIG. 31. Vibrational heat capacity of N_2 derived from statistical mechanics (black curve) compared to the high temperature limit (dashed red curve).

For rotation, the partition function is:

$$q_{rot} = \sum_{J}^{\infty} gexp(-J(J+1)\beta B) = \sum_{J}^{\infty} gexp\left(-J(J+1)\frac{\Theta_{rot}}{T}\right), \quad (41)$$

Where g = 2J+1 and *B* is the fundamental rotational constant. For N_2 Θ_{rot} = 2.8759 K, so at temperatures above 48.68 K N_2 rotation is said to be in the high temperature limit. N_2 being in the high temperature limit ($C_{V,rot}$ ~ Nk_B) between 140 K and 700 K is confirmed by the plot of the rotational heat capacity of N_2 shown in Figure 32.

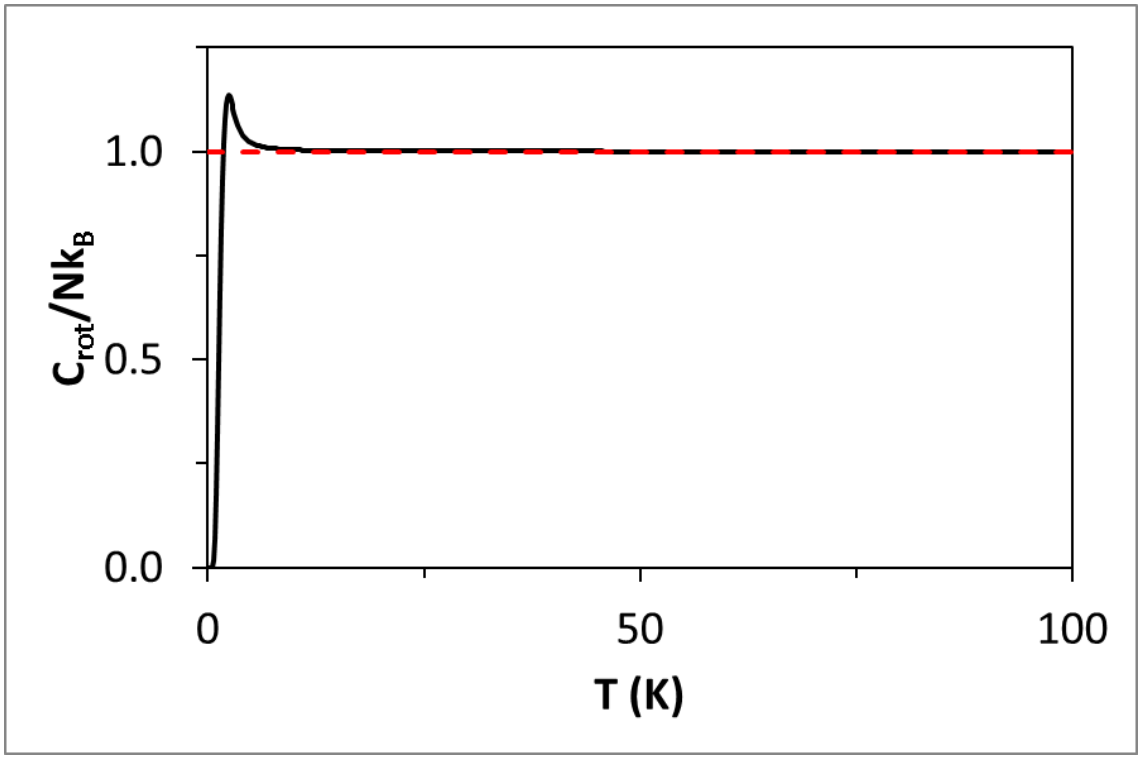

FIG. 32. Rotational heat capacity of N_2 derived from statistical mechanics (black curve) compared to the high temperature limit (dashed red curve).

All molecules in this dissertation are assumed to be in the high temperature limit for calculation of translational heat capacities. The total heat capacity for N_2 below 1000 K is therefore the sum of the vibrational, rotational, and translational heat capacities which is shown in Figure 33.

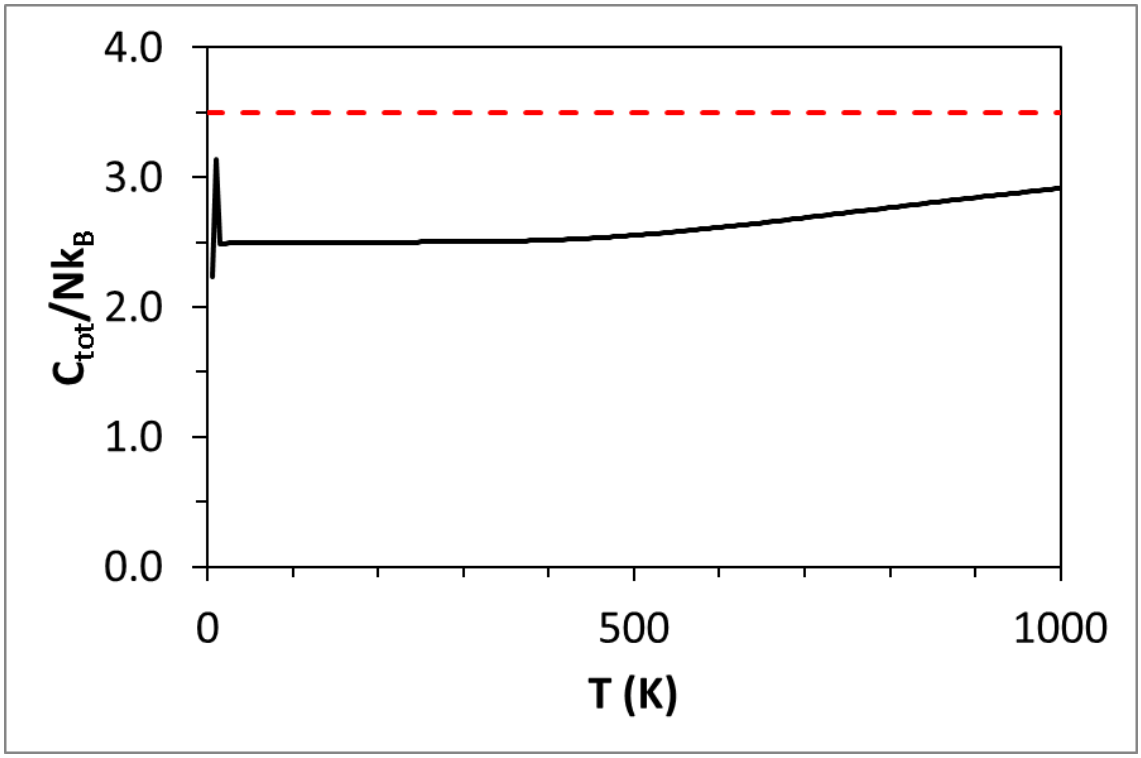

FIG. 33. Total heat capacity of N_2 derived from statistical mechanics (black curve) compared to the high temperature limit (dashed red curve).

If it is assumed that nearly all of the energy lost from benzene CET is gained by N_2 as an increase in temperature, then the loss of energy per $C_6H_6^*$ molecule and gain in energy of each N_2 molecule can be calculated. The N_2 total heat capacity can then be integrated

from the average initial temperature of N_2 to each temperature value at a given number of collisions such that the integral of the heat capacity to each temperature value equals the total amount of energy gained per N_2 molecule. Therefore, the temperature rise plot derived from the benzene collisional relaxation plot, Figure 29, is shown in Figure 34.

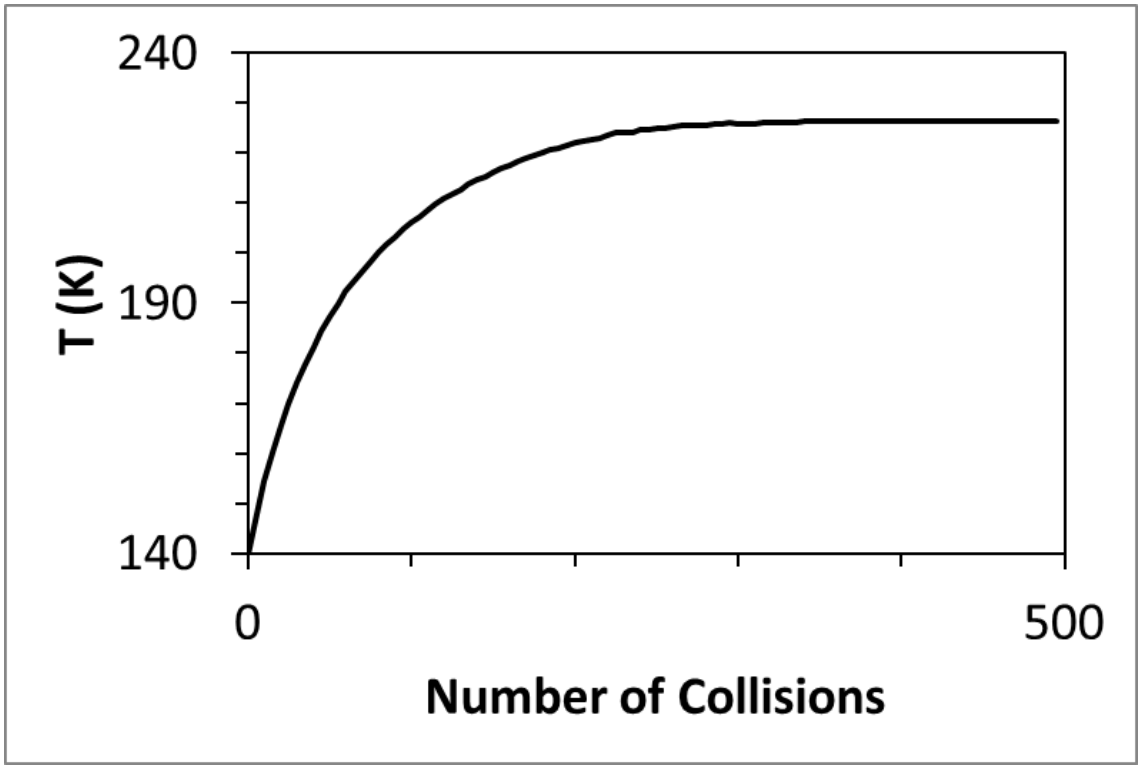

FIG. 34. Bath temperature rise derived from integrating the N_2 total heat capacity.

If instead of a temperature rise from an initial temperature of 140 K to a final temperature of 225 K, a temperature rise from an initial temperature of 300 K to a final temperature of 610 K is simulated then the difference in rates of these temperature rises

can be utilized to determine the temperature dependence of C_6H_6*-N_2 CET rate. First, the CET rate is slower above 300 K, so the relaxation of $C_6H_6^*$ requires more collisions as shown in Figure 35.

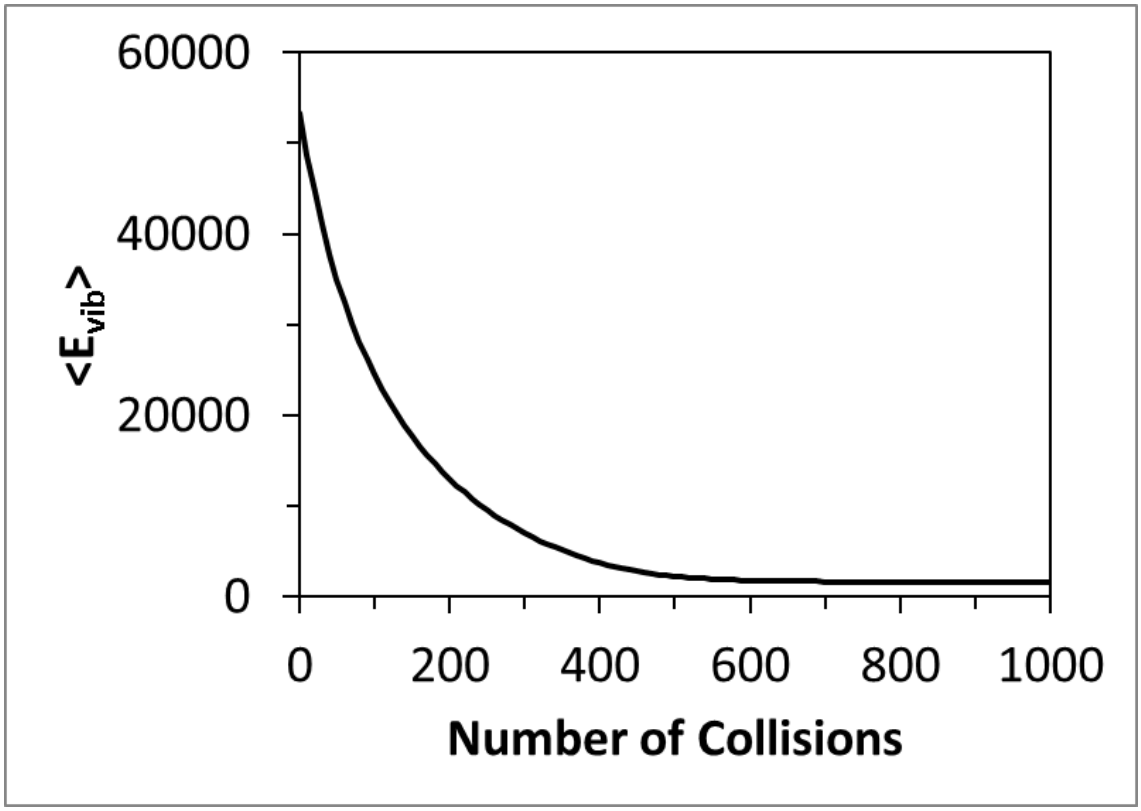

FIG. 35. Average vibrational relaxation of $C_6H_6^*$ given T_0 = 300 K and T_f = 610 K.

The thermal distribution of populated vibrational levels of C6H6 is also broader at 300 K than at 140 K, so the initial distribution in Figure 36 is broader than in Figure 30.

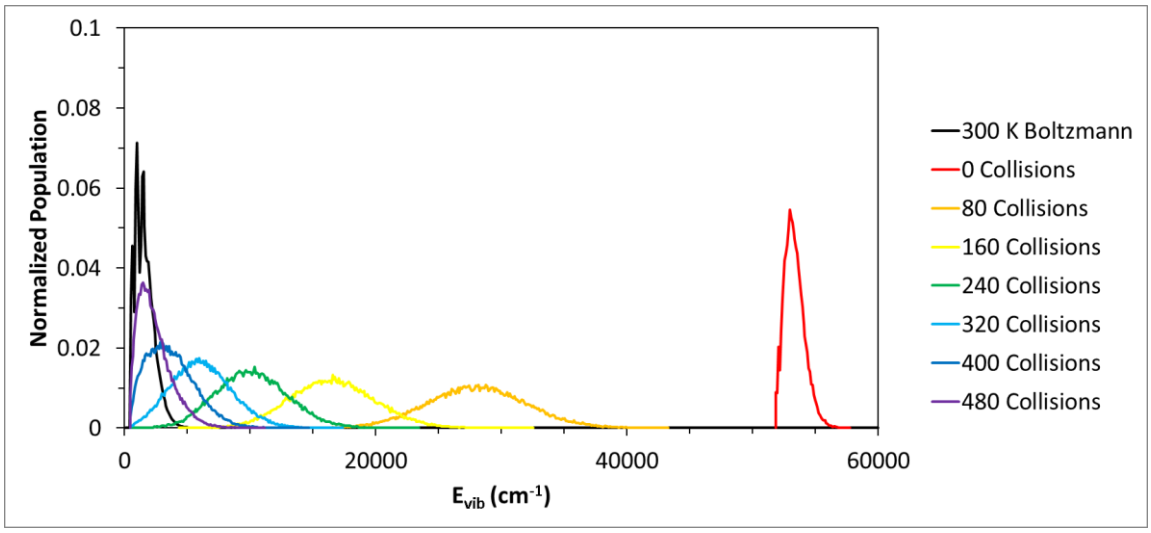

FIG. 36. Normalized vibrational energy distributions for 500,000 benzene molecules after various numbers of collisions in a MultiWell simulation. T_0 = 300 K.

Lastly, the effect on temperature rise curvature of the slight increase in N_2 vibrational heat capacity near 600 K compared to no vibrational heat capacity in the equipartition theorem is shown to be minimal when plotting temperature rises derived from both methods that have been scaled to each other as shown in Figure 37.

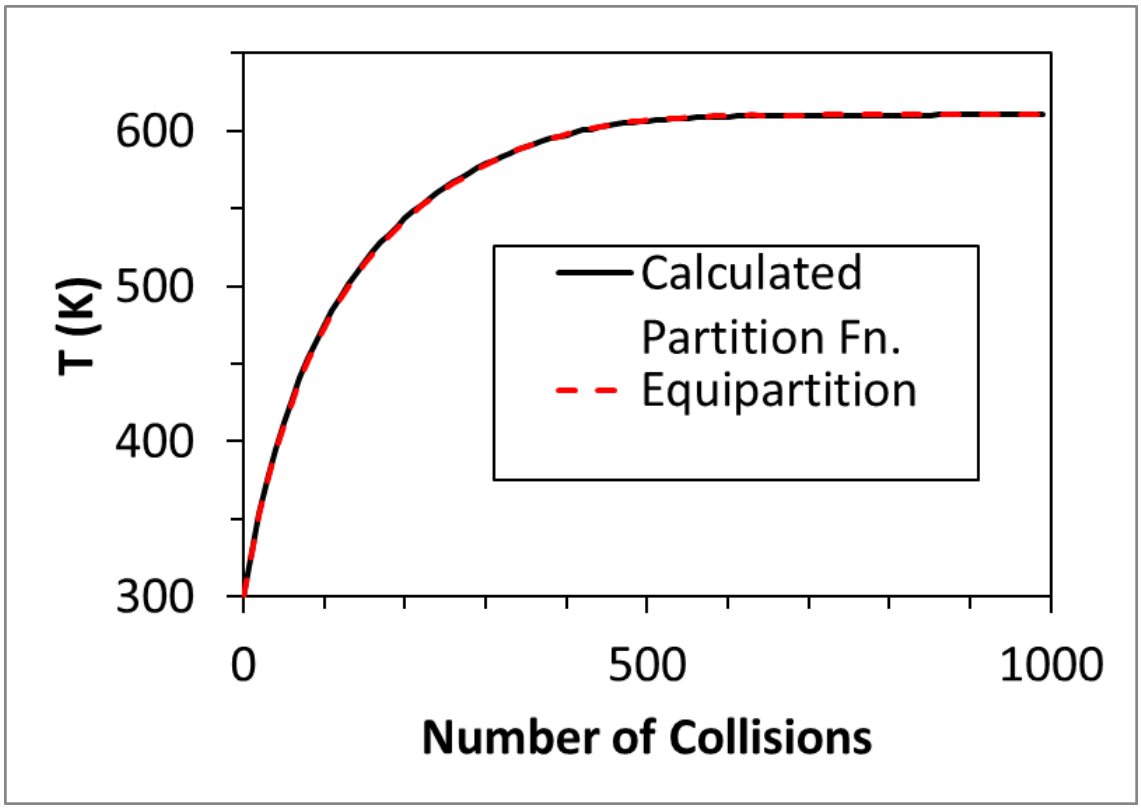

FIG. 37. Scaled bath temperature rises from integrating the N_2 total heat capacities derived from statistical mechanics and the equipartition theorem.

The heat capacities of other molecules can also affect LINE temperature rises, particularly the C_6H_6 heat capacities. The rotational partition function for C_6H_6 can be approximated as that of an oblate symmetric top where $I_A > I_B = I_C$.

$$q_{rot} = \sum_{J}^{\infty} g exp(-J(J+1)\beta\bar{B}) \sum_{K=-J}^{J} exp(-\beta[\bar{A}-\bar{B}]K^2) \tag{42}$$

$$= \sum_{J}^{\infty} g exp\left(-J(J+1)\frac{\Theta_B}{T}\right) \sum_{K=-J}^{J} exp\left(-\left[\frac{\Theta_A - \Theta_B}{T}\right]K^2\right),$$

Where I_A, I_B, and I_C are the moments of inertia of C_6H_6, $\overline{A}$ and $\overline{B}$ are the fundamental rotational constants for I_A and I_B respectively, Θ_A and Θ_B are the characteristic temperatures of rotational modes A and B, and K = -J, -J + 1, …, 0, …, J – 1, J. Figure 38 shows the vibrational and rotational heat capacities of C_6H_6.

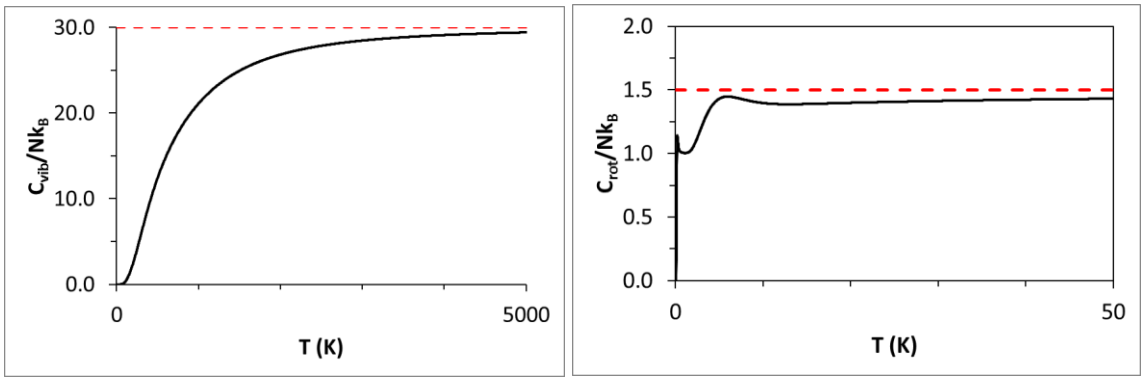

FIG. 38. Vibrational (Left) and rotational (Right) heat capacities of benzene.

Since benzene has many vibrational modes that are lower in frequency than the vibrational frequency of N_2, benzenes vibrational heat capacity begins to steeply increase toward the value predicted by the equipartition theorem at a lower temperature than the vibrational heat capacity of N_2. For the rotational heat capacity of benzene, the calculated heat capacity increased to approximately the value predicted by the equipartition theorem by ~10 K, and then asymptotes to the value predicted by the equipartition theorem. For the translational heat capacity of benzene, again, all molecules in this dissertation are assumed to be in the high temperature limit for

calculation of translational heat capacities. The total heat capacity for benzene below 1000 K is therefore the sum of the vibrational, rotational, and translational heat capacities which is shown in Figure 39.

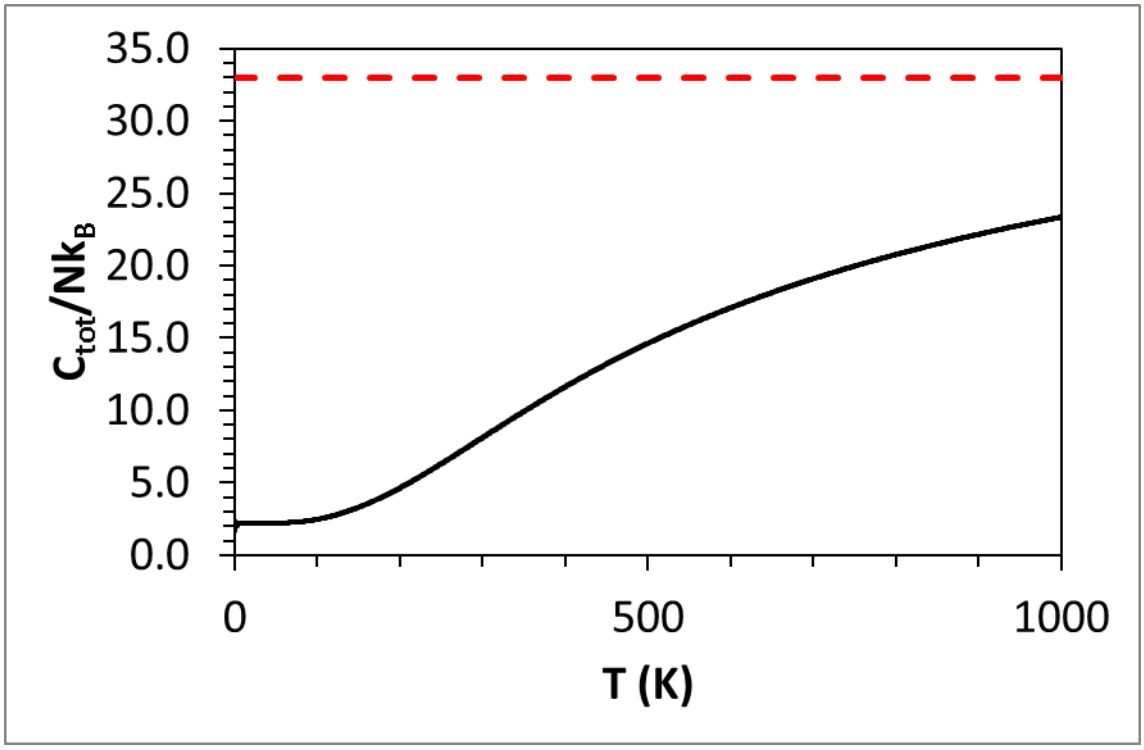

FIG. 39. Total heat capacity of benzene.

Overall benzene has a larger total heat capacity than N_2, but since benzene was only seeded into flow fields in experiments in this dissertation at a few percent of the gas mixture, it was assumed that unexcited benzene's impact on the temperature rises was minimal. It was also assumed that energy transfer to unexcited benzene from N_2 was a

much slower process than energy transfer from $C_6H_6^*$ to N_2, so this also minimized the affect that unexcited benzene had on predicted temperature rises.

It is possible that there is a non-negligible contribution from C_6H_6*-C_6H_6 CET in our experiments. However, we expect this to be a slower path for CET to the bath rotation-translation modes above 300 K since the pathway involves predominantly V-V CET, redistributing vibration from highly excited benzene to vibration in unexcited benzene.[23, 37] As a result, both benzenes in the C_6H_6*-C_6H_6 collision would later undergo V-RT CET to the bath at slower rates than the highly excited benzene would have undergone if the highly excited benzene had not collided with an unexcited benzene. Inefficient C_6H_6*-C_6H_6 V-RT collisions also occur, $\langle \Delta E \rangle$ of about -17 cm^{-1} for V-R CET at E' of 40,700 cm^{-1} in classical trajectory calculations by Oref *et al.*, which would quickly RT-RT CET to the N_2 bath.[23] However, the effect of both C_6H_6*-C_6H_6 CET pathways for CET to the bath in our experiment are also diminished by C_6H_6*-C_6H_6 collisions occurring much less frequently than C_6H_6*-N_2 collisions. Utilizing Equation 31, the collision rate for C_6H_6*-N_2 collisions at 18 torr decreases from 2.7×10^8 s^{-1} to 1.4×10^8 s^{-1} between 300 K and 700 K. Whereas the collision rate for C_6H_6*-C_6H_6 collisions at 1.26 torr (7% of 18 torr) decreases from 2.8×10^7 s^{-1} to 1.2×10^7 s^{-1} between 300 K and 700 K. Therefore, the C_6H_6*-N_2 collision rate is consistently at least a factor of 9 larger than the C_6H_6*-C_6H_6 collision rate in this experiment which implies that the effect of the large magnitude C_6H_6*-C_6H_6 collisions on the overall CET rate observed in the temperature rises is greatly diminished. Therefore, any CET rate parameters derived from data in this dissertation are for a gas

mixture and not pure C_6H_6*-N_2 collisions. However, improvements in this method such as higher probe laser power, better iCCD cameras, and an improved slow-flow cell will make it possible to use smaller C_6H_6 mixing ratios which will significantly reduce the effect of C_6H_6*-C_6H_6 collisions on the overall CET rate observed in the temperature rises.

At temperatures below 300 K it is likely that C_6H_6*-C_6H_6 V-V CET is much more efficient. Classical trajectory calculations by *Oref et al.* have indicated that C_6H_6*-C_6H_6 V-V CET becomes more efficient with decrease in temperature between the temperatures 300 K, 250 K, and 200 K.[23] Also, work by Miller *et al.* has shown that, in a similar system, pyrazine*-pyrazine V-V CET becomes more efficient at 254 K by monitoring excited pyrazine with IRF.[55] However, experiments in this dissertation are not sensitive to branching ratio between V-RT and V-V CET pathways. Therefore, in the future, it may be necessary to perform classical trajectory calculations in order to determine the effect of V-V CET in low temperature CET experiments.

Summary

Multiwell modeling was utilized in this dissertation to make simulations of the collisional relaxation of highly vibrationally excited benzene which were utilized to make simulated N_2 temperature rises to fit experimental N_2 temperature rises. It was assumed that most of the energy was transferred from benzene vibration to N_2 rotation and translation, and that the change in bath temperature due to the increase in energy of the bath could be determined by integrating the N_2 heat capacity. Since the collisional relaxation of benzene was modeled with internal energy and bath temperature

dependencies, best fit simulated temperature rises were utilized to determine the dependencies of benzene LINE on benzene internal energy and on bath temperature so that benzene LINE can be utilized in a variety of supersonic and hypersonic flow field conditions and cause perturbations that vary in both magnitude and rate.

CHAPTER V

PROJECT I: ROOM TEMPERATURE LINE*

Transient N_2 bath temperature rises to a variety of final bath temperatures due to CET from highly vibrationally excited benzene were measured given an initial bath temperature of 300 K. This allowed for the comparison of the CET rate results to previous studies performed at 300 K in order to verify that the CET rate could be monitored via NO LIF temperature measurements. Also, another goal of this project was to determine the temperature dependence of the rate of CET in order to make predictions about the rate of benzene LINE in diverse flow field conditions since regions of varying temperatures exist in many supersonic and hypersonic flow fields. Additionally, the internal energy dependence of benzene CET was of interest since it can be utilized to predict how change in the pump laser wavelength will affect the rate of benzene CET and hence the rate of benzene LINE relaxation.

Experimental Setup

In transient temperature rise measurements, NO two-line Planar Laser Induced Fluorescence (PLIF) transient temperatures were determined utilizing the $Q_2 + R_{12}$ (5.5) and $P_2 + Q_{12}$(17.5) transitions $A^2\Sigma^+$ (v′ = 0) ←$X^2\Pi_{1/2}$ (v′′ = 0) band, due to their large S/N

* Reprinted in part from N. A. West, J. D. Winner, R. D. W. Bowersox, and S. W. North. Resolving the Energy and Temperature Dependence of C6H6* Collisional Relaxation via Time-Dependent Bath Temperature Measurements, The Journal of Chemical Physics **145**, 014308 (2016). with the permission of AIP Publishing.

and temperature sensitivity between 300 K and 700 K. Bath temperatures were evaluated with Equation 23 where the value of C_{12} was determined by measuring the fluorescence intensities of the bath at room temperature. Two-line temperature values were also checked by scanning the 226.5-226.7 nm NO LIF region and performing least-squares fits to simulations in LIFBASE for scans between 300 K and 700 K.[81] The scans also demonstrated that the system was thermalized at the measured pump-probe delays.

We observed that >95% of the short term temperature rise occurred by 4 μs after the pump beam, and a plot of the temperature map of the maximum temperature achieved in the bath at 4 - 6 μs shows that there was a large gradient in bath temperature in the region imaged by the camera.[98] This temperature gradient was due to attenuation of 193 nm light by C_6H_6 as well as a gradient of C_6H_6 partial pressure in the region examined. However, diffusion of C_6H_6* was calculated to be between 10 -20 μm/μs and only significantly affected temperature measurements between 10 -15 μs.

Results

Spatially-resolved two-line NO PLIF temperature measurements were made for each pixel location in the raw fluorescence images. Representative raw emission images at a pump-probe time delay of 0.2 μs are shown in Figure 40. Each image was acquired > 10 times and was averaged to improve the S/N. In these images the 226 nm probe beam was directed right-to-left and the 193 nm beam was directed left-to-right. The horizontal variation of Q_2(5.5) NO fluorescence is due to quenching by C_6H_6, resulting in

the lowest signal near the exit of the 6.35 mm tube where the $C_6H_6/N_2/NO$ mixture was introduced into the slow-flow cell, the location in which $[C_6H_6]$ was largest. For the smallest pump-probe time delays, we observed appreciable emission from C_6H_6 on the left side of the images, Figure 40, due to a larger 193 nm beam power in that region. The variation from right to left is consistent with the attenuation of 193 nm beam power due to C_6H_6 absorption. For the smallest pump-probe time delay images, up to 33% of the signal for pixels on the right side of the image came from benzene emission. Therefore, at each pump-probe time delay, 10 images with the 226 nm beam blocked were acquired, averaged, and subtracted from the NO fluorescence (226 nm beam on) images.

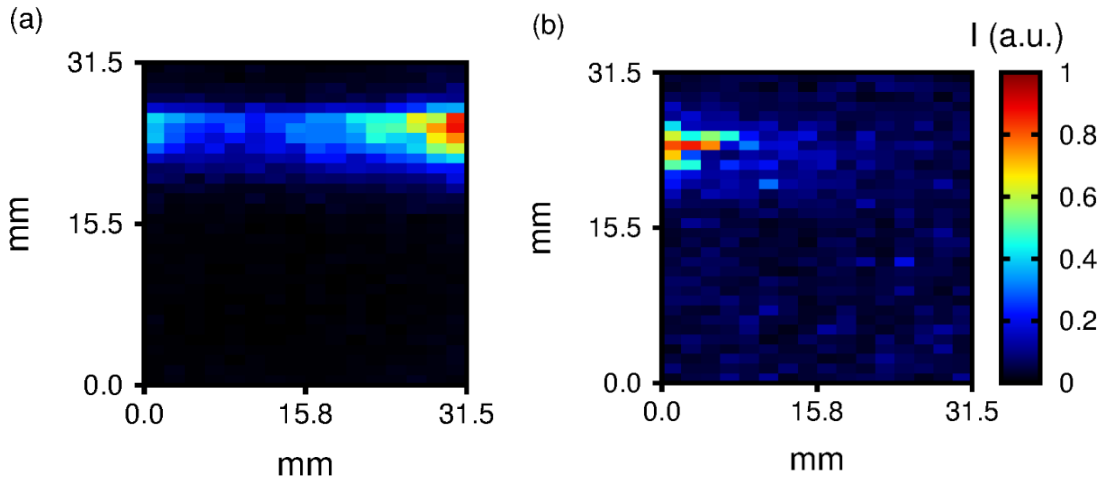

FIG. 40. Raw images at 18 torr at a pump-probe time delay of 0.2 μs. (a) $Q_2(5.5)$ NO fluorescence, (b) C_6H_6 emission (226 nm laser blocked).

Following subtraction of 193 nm emission, each temperature value was calculated with Equation 23 by comparing single pixel integrated signals, S_1 and S_2, originating from the same pixel position in a pair of images. The image that yielded S_1 probed the J = 5.5 rotational state of NO and the image that yielded S_2 probed the J = 17.5 rotational state of NO. These image pairs were acquired at each pump-probe time delay in a randomized order to yield a time-dependent temperature rise for each pixel. An example of the timing for the first few randomized time delay images is shown in Figure 41 with negative time delay images in between.

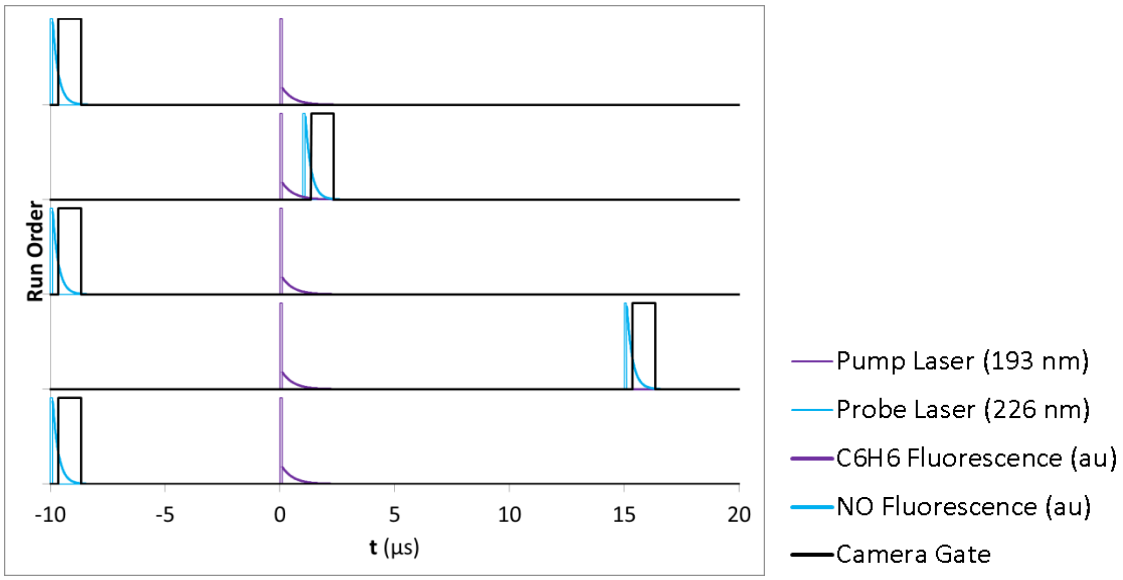

FIG. 41. Example timing diagrams for randomized PLIF temperature measurements.

The negative time delay images were utilized to calculate C_{12} values and to monitor drift in the measurements. The experiment was then repeated > 10 times to yield a group of > 10 temperature rises for each pixel such that temperature rise averaging and analysis of statistical error could be carried out for each pixel location. An example of ten repeatedly measured single pixel temperature rises originating from the same pixel location is shown in Figure 42.

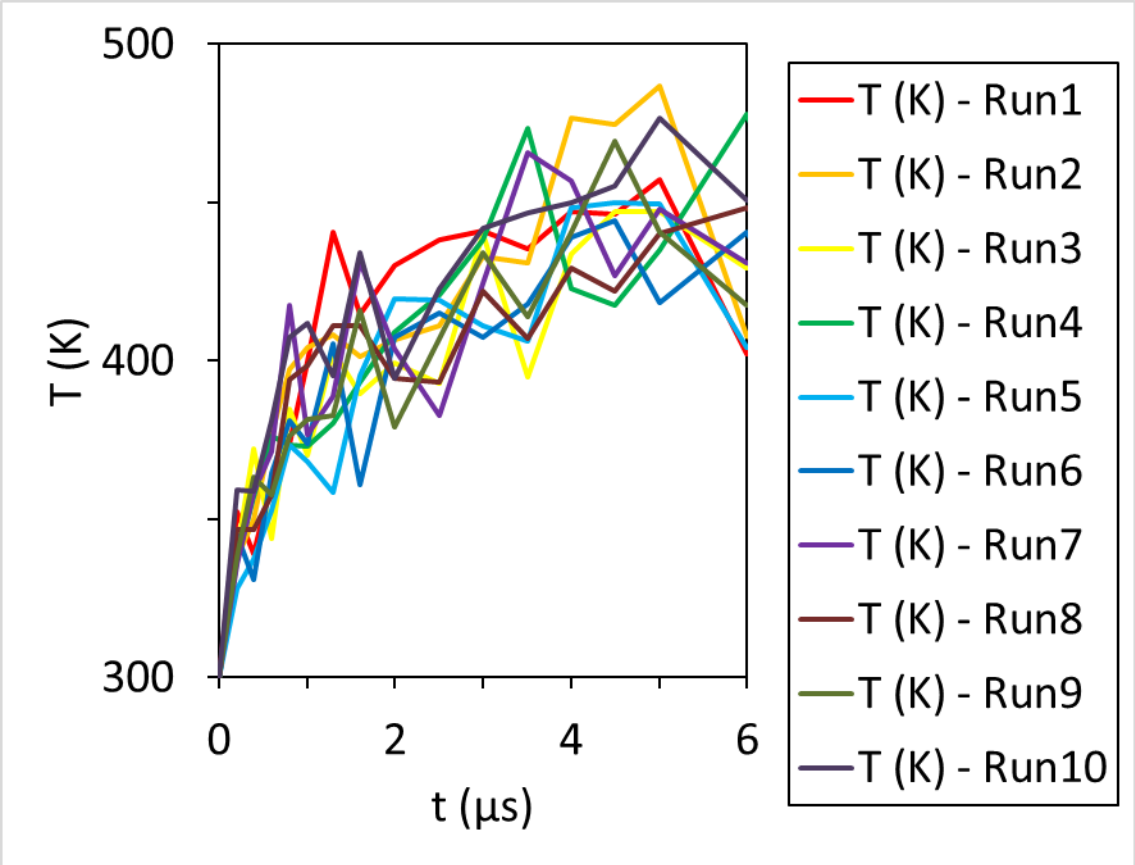

FIG. 42. Example of ten repeatedly measured single pixel temperature rises originating from the same pixel location.

Each group of > 10 temperature rises at each pixel location were scaled and averaged to yield an improved S/N temperature rise at each pixel location. An example single pixel averaged temperature rise is shown in Figure 43.

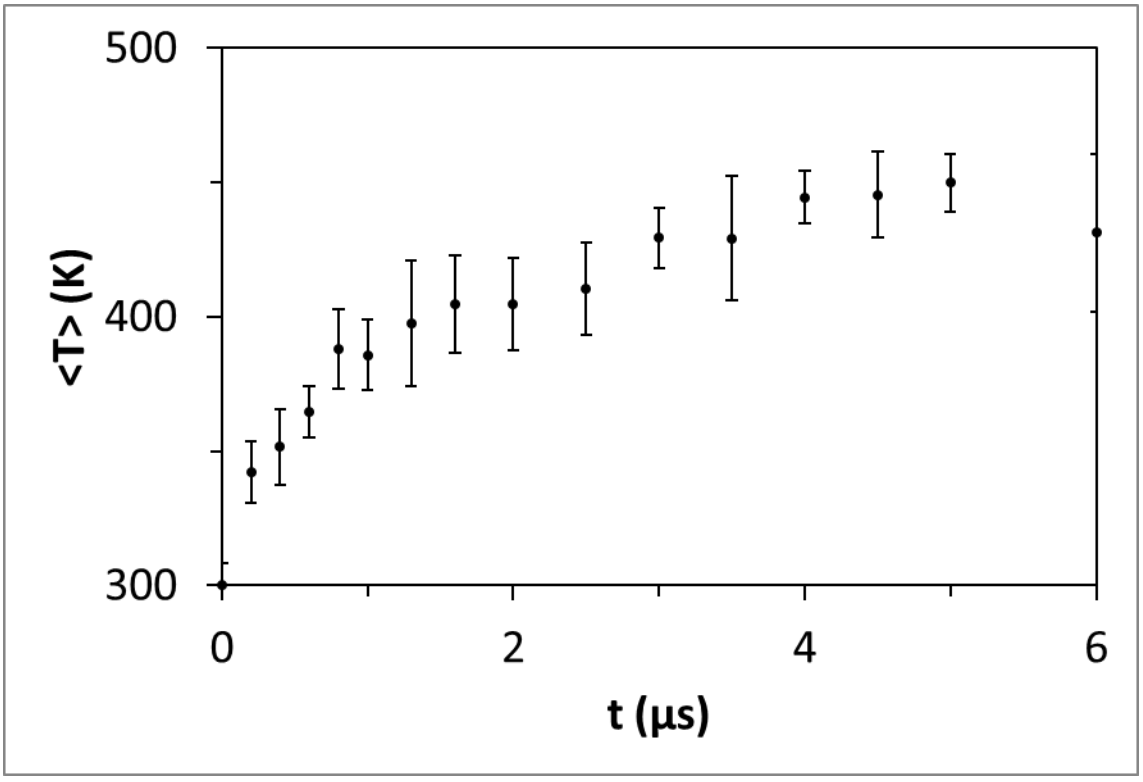

FIG. 43. Example of an averaged temperature rise obtained from averaging ten repeatedly measured single pixel temperature rises originating from the same pixel location.

Scaling of the > 10 temperature rises at each pixel location to the same final temperature was carried out to ensure that the error bars in time-dependent temperature values originate from statistical fluctuations in temperature measurements and not small

differences in final temperature from one experiment to the next. To scale the group of temperature rises at each pixel location, each group was first denoted by an integer *k*. Each temperature rise within a group was then denoted by an integer *j*. Next, each time-dependent temperature value was denoted by $T_{ijk}(t)$ where *i* represents each sequential pump-probe time delay. The final average temperature, $<T_{fjk}>$, for each temperature rise was then determined by averaging the $T_{ijk}(t)$ values at pump-probe time delays between 3 - 6 μs of that rise.

$$< T_{fjk} >= \sum_{i=I-N_f}^{I} \frac{T_{ijk}(t)}{N_f}, \tag{43}$$

Where *I* is the total number of pump-probe time delays and N_f is the number of final $T_{ijk}(t)$ values to be averaged. The pump-probe delay of 6 μs was chosen as the cutoff for analysis purposes because after 6 μs factors like diffusion caused temperature from each pixel location to either slightly increase or decrease depending on if the surrounding gas was either higher or lower in temperature on average. Next, the average of the $<T_{fjk}>$ values, $<<T_{fk}>>$, was determined for each group in order to determine the final temperature to which the rises should be scaled.

$$<< T_{fk} >>= \sum_{j=1}^{J_k} \frac{< T_{fjk} >}{J_k} \tag{44}$$

Where J_k is the total number of temperature rises in group *k*. Next, all $T_{ijk}(t)$ values were scaled utilizing Equation 45.

$$T'_{ijk}(t) = (T_{ijk}(t) - T_0)\left[\frac{(<< T_{fk} >> - T_0)}{(< T_{fjk} > - T_0)}\right] + T_0 \quad (45)$$

Where T_0 = 300 K in this experiment. At this point all temperature rises within each group have been scaled to the same final average temperature, $<<T_{fk}>>$. Next the final scaled and averaged temperature rise for each group was calculated by averaging the scaled time-dependent temperature values from each time delay.

$$< T'_{ik}(t) >= \sum_{j=1}^{J_k} \frac{T'_{ijk}(t)}{J_k} \quad (46)$$

Temperature error bars for the scaled and averaged temperature rises were then determined from the standard deviation, σ_{ik}, of the scaled time-dependent temperature values at each time delay.

$$\sigma_{ik} = \sqrt{\frac{1}{J_k}\sum_{j=1}^{J_k}\left(T'_{ijk}(t) - < T'_{ik}(t) >\right)^2} \quad (47)$$

The result was an averaged temperature rise for each pixel location in the field of view in the raw image. The final average temperature, $<<T_{fk}>>$, at each pixel location varied from 350 – 700 K within the field of view as shown in Figure 44. The gradient in final average temperature occurred due to a gradient in benzene concentration as well as a gradient in 193 nm beam power. The temperature gradient in the probed region allowed for the study of the temperature dependence of the CET efficiency.

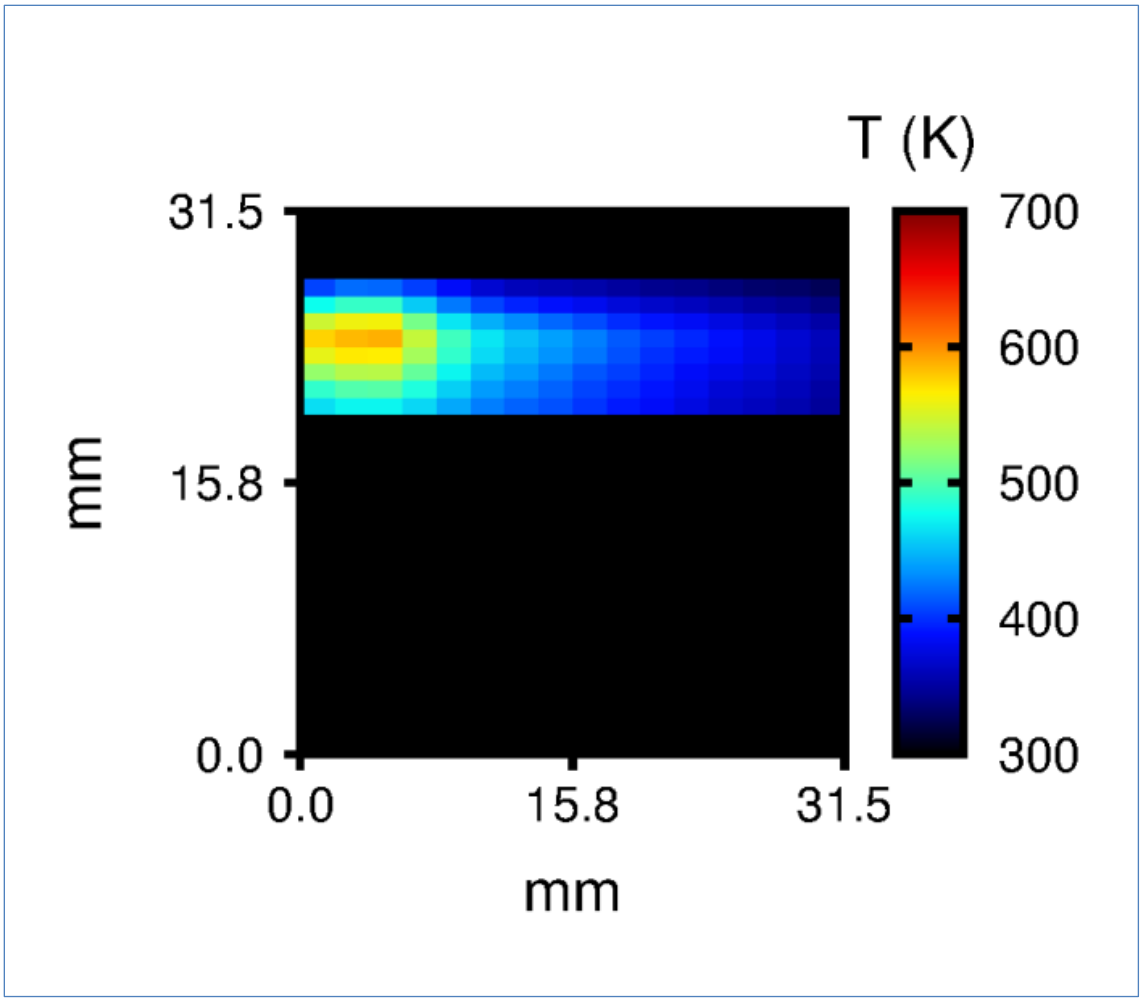

FIG. 44. Spatially resolved average temperature between 3 - 6 μs.

Since a dependence of CET efficiency on bath temperature was expected, the averaged temperature rise of each pixel was placed into a temperature dependent bin based on the final average temperature, $\langle\langle T_{fk} \rangle\rangle$. The bins were separated according to final average temperature every 30 K. A number of pixels had large error bar temperature measurements which originated from regions with low NO fluorescence

signal due to low 226 nm beam power at the edges of the beam. Temperature rises with undesirably large error bars were rejected from the bins if, in that temperature rise, the average of the error bars was larger than 20% of the total rise in temperature. Each bin of averaged temperature rises was then scaled and averaged using the same procedure that groups of temperature rises from each pixel location were scaled and averaged. This yielded time-dependent temperature rises which could be examined for their CET rate dependence on the final temperature of the rise. Therefore, the CET efficiency in a final scaled and averaged temperature rise of a bin represents the average CET efficiency for the range of temperature rises to different final temperatures that were averaged in that bin.

The time-dependent temperature rises were then converted to collision-dependent temperature rises for direct comparison with previous CET studies. To accomplish this conversion, the time between successive temperature measurements was converted to number of collisions using the temperature dependent collision rate, Equation 31 and is plotted vs temperature in Figure 45.

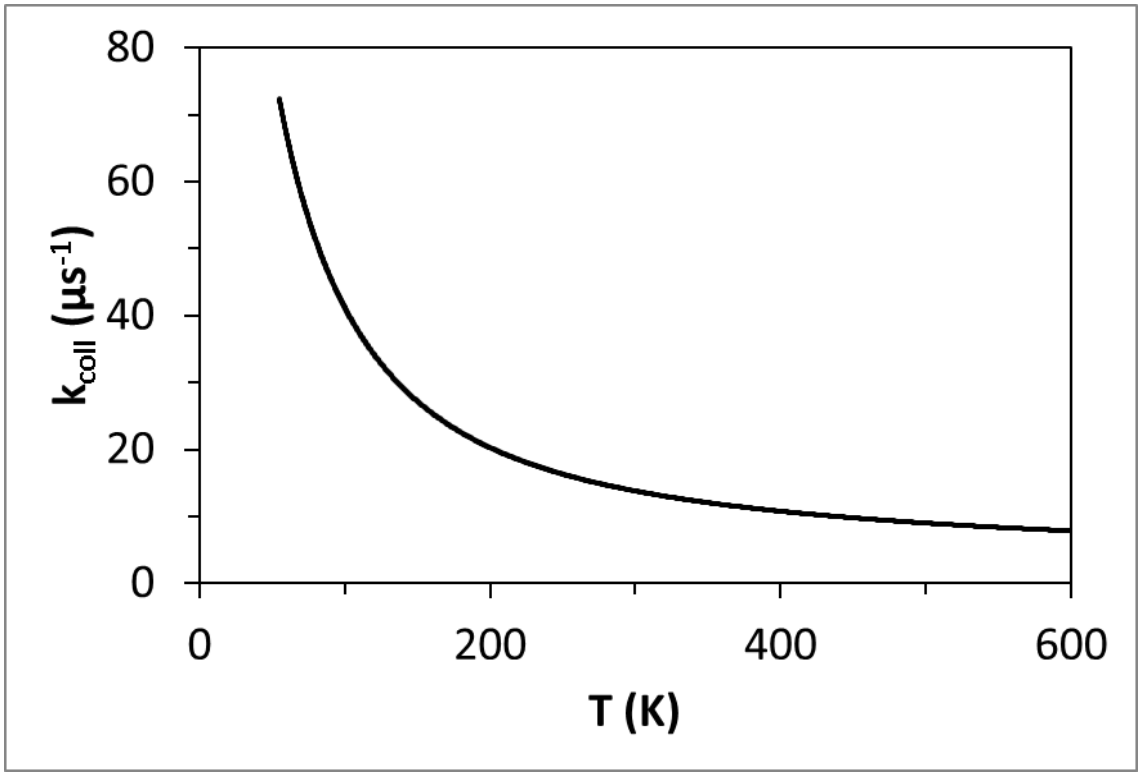

FIG. 45. Example Lennard-Jones temperature dependent collision rate vs temperature calculated at 1 torr.

The temperature used to calculate the collision rate for converting time dependent temperature rise data points to collision space was the average of successive temperature values in the temperature rise. An example time dependent temperature rise was scaled to (normalized) collision space in Figure 46.

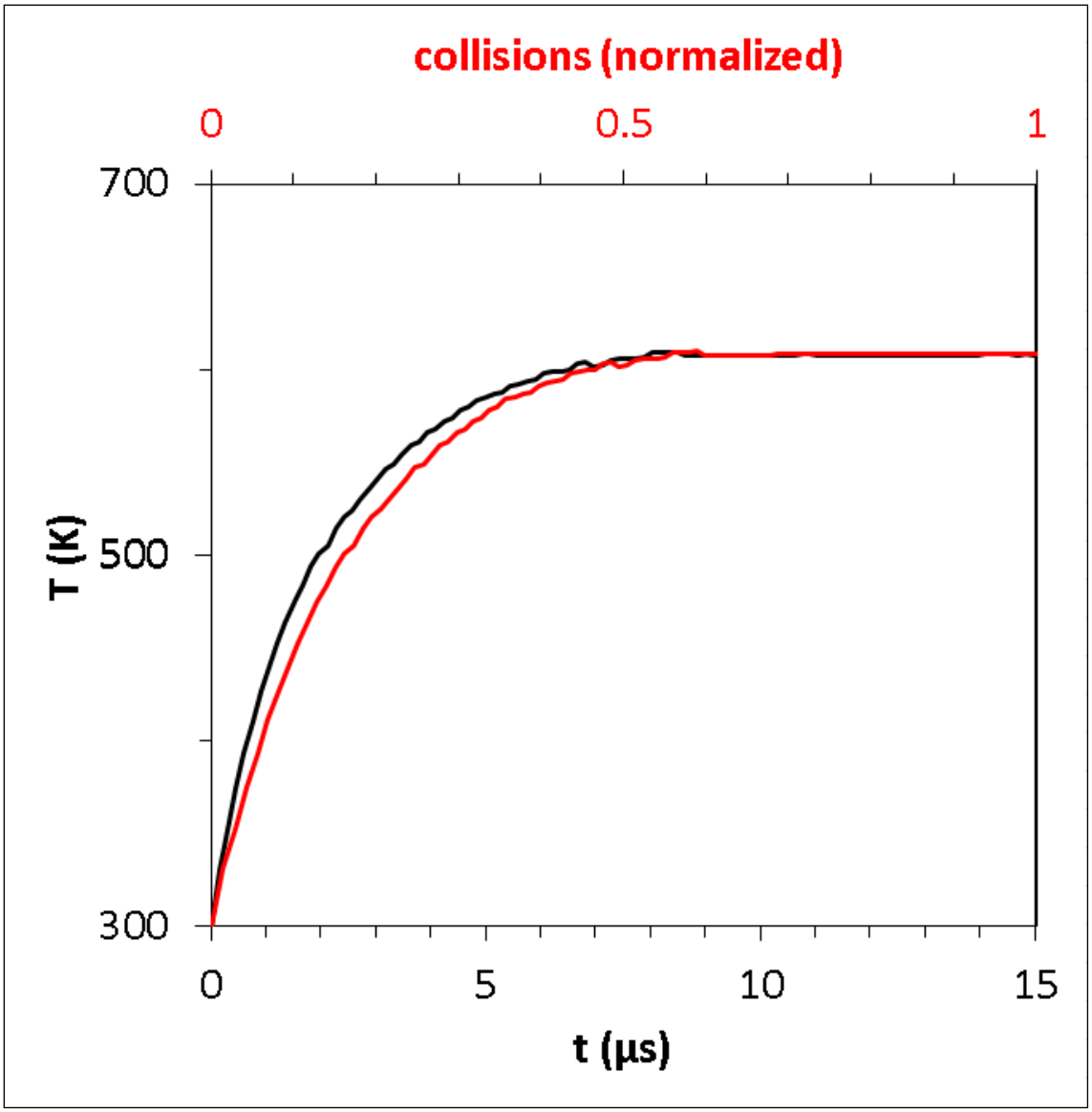

FIG. 46. Example time dependent temperature rise scaled to (normalized) collision space.

In Figure 46 the early low temperature data points become more spread apart in collision space and the late high temperature data points are closer together which slightly

changes the curvature of the temperature rise since the collision rate was higher at lower temperatures.

Temperature Rise Fitting

In our initial treatment of CET, we employed a constant value for $\alpha_1(E')$ in $P(E',E)$ (Equation 2) which was optimized to yield best a fit temperature rise simulation. The model utilizing a constant value for $\alpha_1(E')$ implies a constant amount of energy is transferred in deactivating collisions, $\langle \Delta E_d \rangle$, which yields a linear temperature rise that curves to an asymptote value as benzene thermalizes, as seen in Figure 47. The best overall fit to the 12 torr data with a ΔT of 130 K is shown in Figure 47. The curvature in the experimental temperature rise data is inconsistent with a master equation model utilizing a constant $\alpha_1(E')$ because the model underestimates the early CET rate and overestimates the late CET rate of the temperature rise. The curvature in the temperature rise suggests a dependence of the CET rate on temperature, $\langle E' \rangle$, or both.

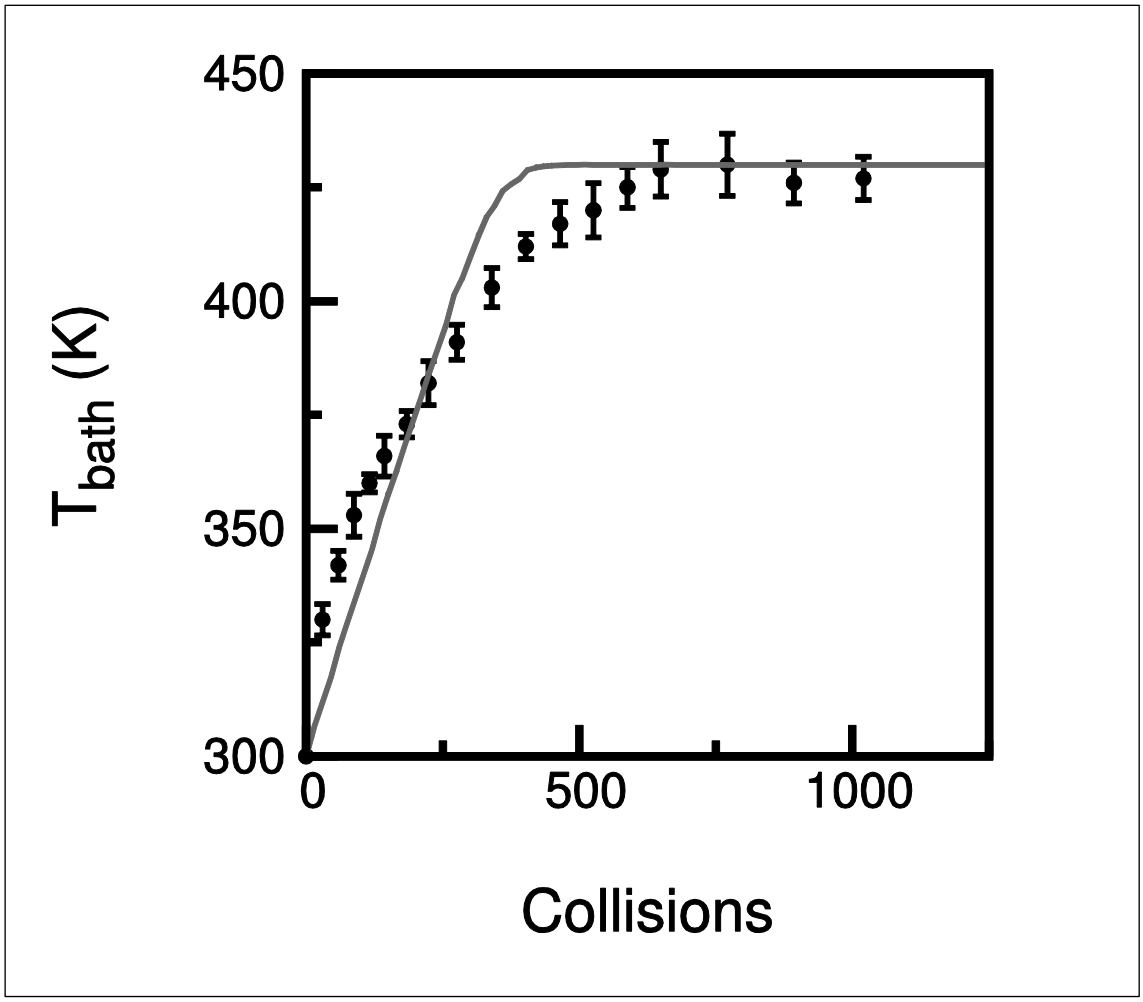

FIG. 47. Temperature rise at 12 torr with ΔT = 130 K (black circles) compared to a master equation simulation using a best fit constant $\alpha_1(E')$ of 275 cm^{-1} (grey line). Error bars represent ± 1 σ statistical error only.

In order to assess the possibility that the curvature in the experimental temperature rise was the result of a bath temperature dependent CET rate, we calculated the difference between subsequent temperature values in Figure 47 which we converted into $-\langle\Delta E\rangle$ values and plotted versus the corresponding average of the

subsequent temperature values as shown in Figure 48. If the change in CET rate were to depend only on the bath temperature, then the values of $\alpha_1(E')$ would have to be inversely proportional to temperature. However, this trend is counter to the temperature dependence on V-RT energy transfer utilized in most models which often utilize CET parameters that are approximately linearly increasing with increase in temperaure.[23, 56, 57]

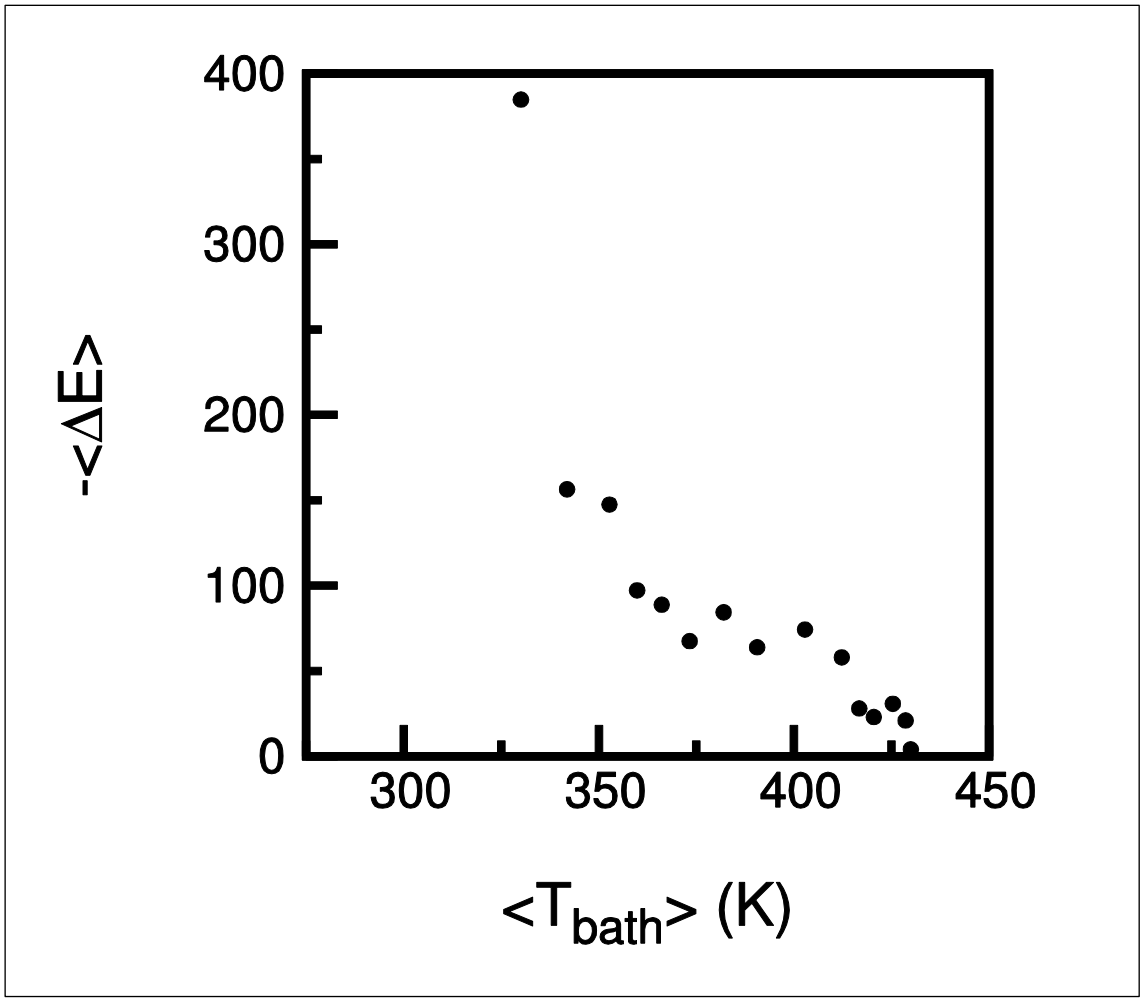

FIG. 48. Change in benzene internal energy per collision vs average temperature for a temperature-binned temperature rise.

An alternate origin for the observed curvature in a temperature rise is a form for $\alpha_1(E')$ that is linearly dependent on E', Equation 4. The temperature rise from the linearly dependent $\alpha_1(E')$ simulation was found to be a good fit to the experimental temperature rise at 12 torr, as seen in Figure 49. Furthermore, identical C_0 and C_1 parameters are found for the linearly dependent $\alpha_1(E')$ for both the 12 torr and 18 torr experimental

temperature rises, once converted to collision space. This result confirms that the energy transfer per collision is also independent of pressure as expected.

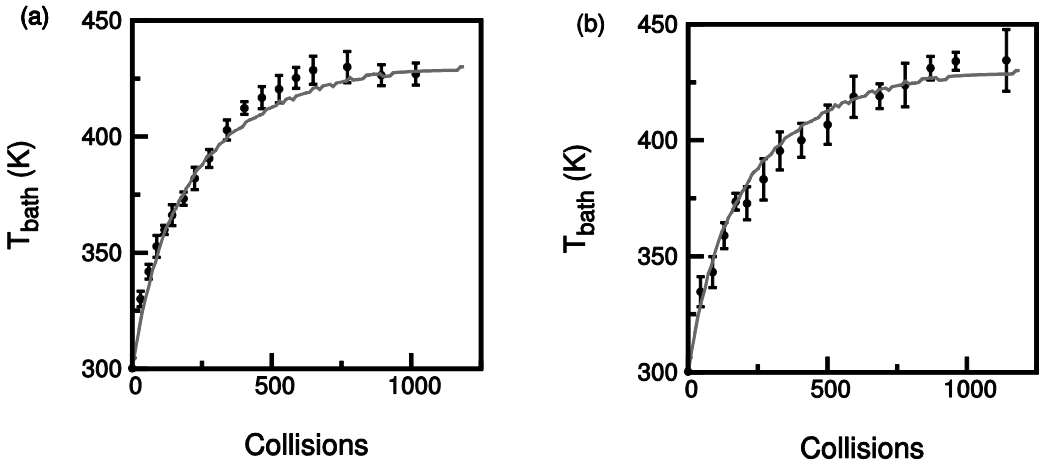

FIG. 49. Experimental temperature-binned temperature rises (black circles) at two pressures. (a) 12 torr. (b) 18 torr. These rises were simultaneously modeled (grey lines) using C_0 = 120 cm^{-1} and C_1 = 0.0080 in Equation 4. Error bars represent ± 1 σ statistical error only.

Internal E dependence of CET

In order to visualize how the CET efficiency varies as a function of benzene internal energy, we plot the average energy transferred per collision, $\langle \Delta E \rangle$, versus $\langle E' \rangle$ in Figure 50. This figure was generated from the optimized simulations of Figures 47 and 49 by taking the average change in energy of benzene per collision and plotting it versus the average internal energy of benzene every 20 collisions. When comparing the average energy transferred per collision, $\langle \Delta E \rangle$ in Equation 5, between a constant $\alpha_1(E')$ model

and an energy dependent $\alpha_1(E')$ model in Figure 50, the energy transfer is initially much larger for the energy dependent $\alpha_1(E')$ until $\langle E' \rangle$ = 30,000 cm^{-1} where the constant $\alpha_1(E')$ model overtakes the linear model. It should be noted that for the constant $\alpha_1(E')$ simulation, the deviation from linearity at low values of $\langle E' \rangle$ is a result of detailed balancing, where the probability of an activating collision has risen sufficiently to impact the average energy transferred per collision.

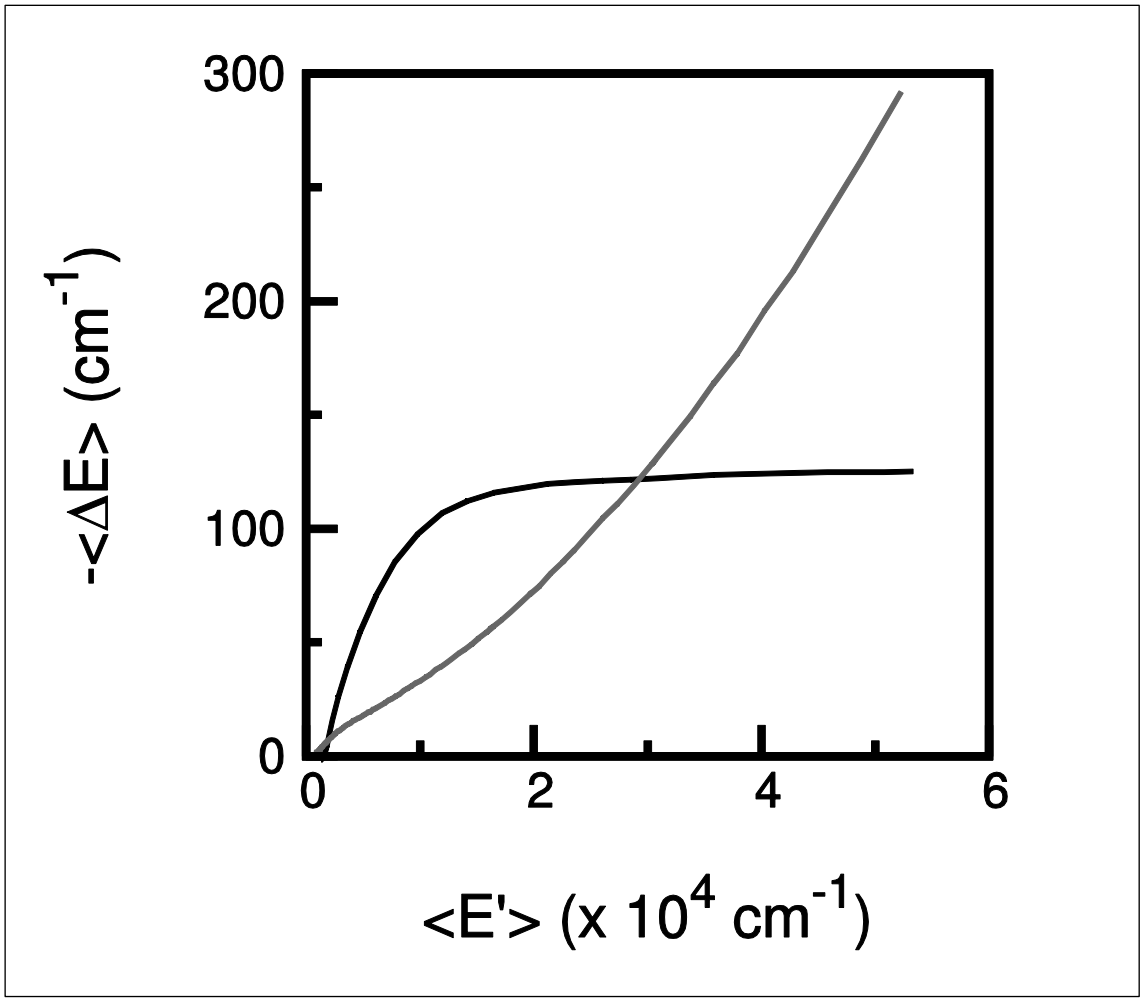

FIG. 50. Models utilizing constant (black line) and linear (grey line) forms of $\alpha_1(E')$ in Equation 4.

It is of importance to examine the temperature dependence of CET, as there is still uncertainty in this area.[37] We observe that the optimized simulations of time-dependent temperature rises corresponding to different final ΔT require fit parameters of Equation 2 that depend on the average final temperature. Table 5 summarizes the

optimized fit parameters using Equation 2 of the linear $\alpha_1(E')$ that were fit utilizing least squares analysis for several different temperature rises.

TABLE 5. Parameters for Equation 4 from fitting model temperature rise data to experimental temperature rises of differing total change in temperature.

ΔT (K)	C_0 (cm^{-1})	C_1 (unitless)	$\alpha_1(E')$ (cm^{-1})
130	138 ± 12	0.0082 ± 0.0007	575 ± 27
155	162 ± 5	0.0079 ± 0.0010	583 ± 20
185	162 ± 7	0.0091 ± 0.0005	647 ± 19
280	169 ± 14	0.0123 ± 0.0010	824 ± 40
310	209 ± 12	0.0118 ± 0.0007	838 ± 22
130 and 310	174 ± 20	0.0102 ± 0.0014	718 ± 48

The optimized values of both C_0 and C_1 increase monotonically with temperature, indicating a positive correlation of CET efficiency with temperature. The increase of C_0 and C_1 between ΔT of 130 K to 310 K results in a 59% increase in $\alpha_1(E')$ for an initial E' value of 53,326 cm^{-1}. In order to assess the error bars for the C_0 and C_1 parameters the least squares of the fits to the temperature rises versus changes in C_0 and C_1 were examined.

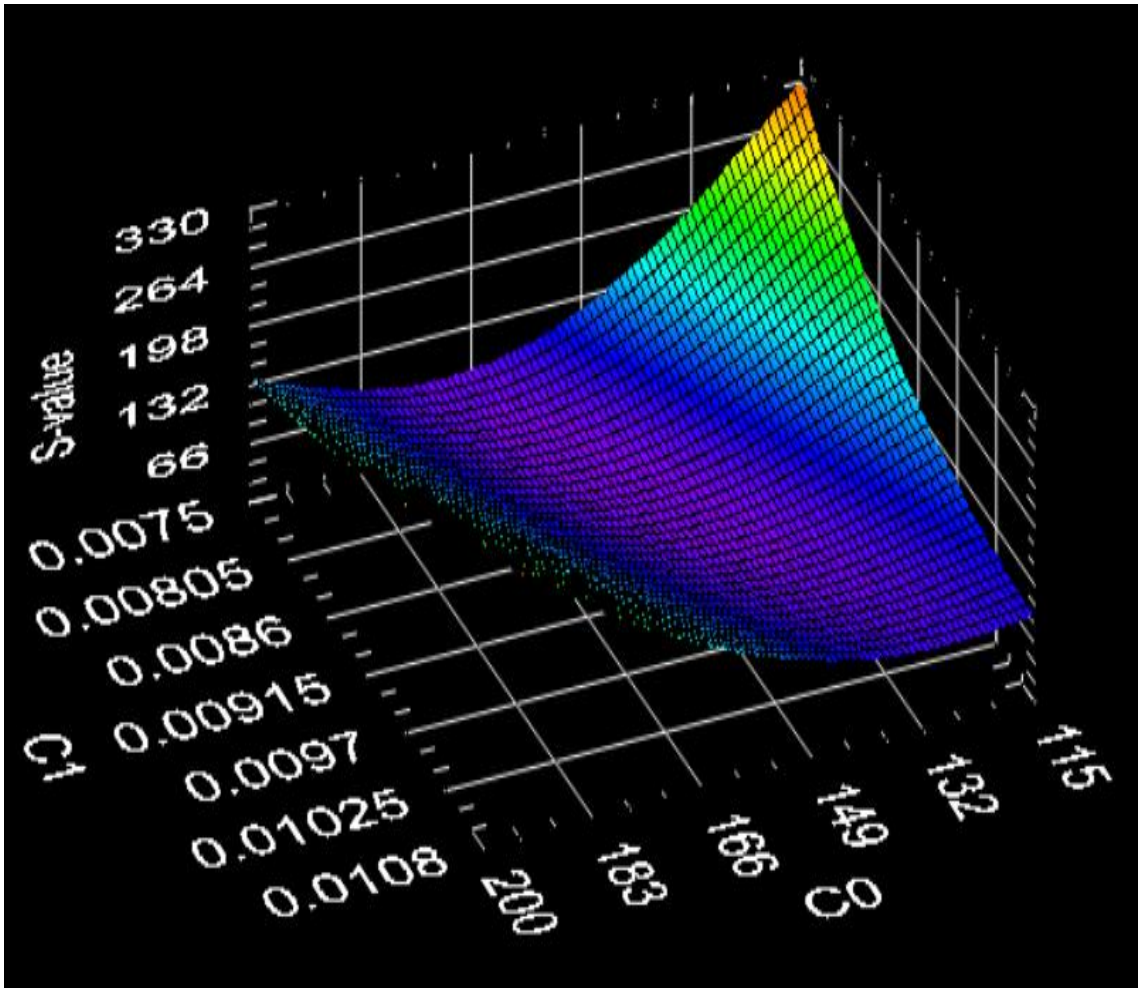

FIG. 51. Values of X^2 comparing the experimental ΔT = 130 K temperature rise to simulated temperature rises generated with varying C_0 and C_1 parameters.

For all of the least squares plots there was noise at the minimum of the χ^2 surface, and it was determined that the least squares values rose monotonically with change in C_0 and C_1 above 4.5% of the minimum value of each well. The analysis also revealed that the C_0 and C_1 parameters are coupled and still yield equivalent least square fits by the simultaneous variation in C_0 and C_1 values. Therefore, the error values for C_0 and C_1

reported in Table 5 represent the range of simultaneous changes in C_0 and C_1 values that meet the criteria of having least square values less than 4.5% above the χ^2 minimum. Although the coupling of the fit C_0 and C_1 values indicates that there is some uncertainty in the internal energy dependence of the C_6H_6* CET, this results in less than a 5% change in all of the $\alpha_1(E')$ values at E' = 53,326 cm^{-1}. Also, the lowest and highest ΔT temperature rises (130 K and 310 K) were fit simultaneously to obtain a temperature independent set of parameters, which are also included in Table 5.

Since the bath temperature does not change during simulations in the MultiWell program, the $\alpha_1(E')$ values did not change due to parameters affected by bath temperature changes during the simulation. However, since the bath temperature does change in the experimental data, the optimized parameters we report for $\alpha_1(E')$ represent a combination of two factors that influence the CET efficiency: bath temperature and internal energy of benzene. We therefore plotted $-\langle \Delta E \rangle$ as a function of $\langle E' \rangle$ generated from optimized fits of time-dependent temperature rises corresponding to various final temperatures, Figure 52, in order to estimate the effect of temperature on the CET rate efficiency.

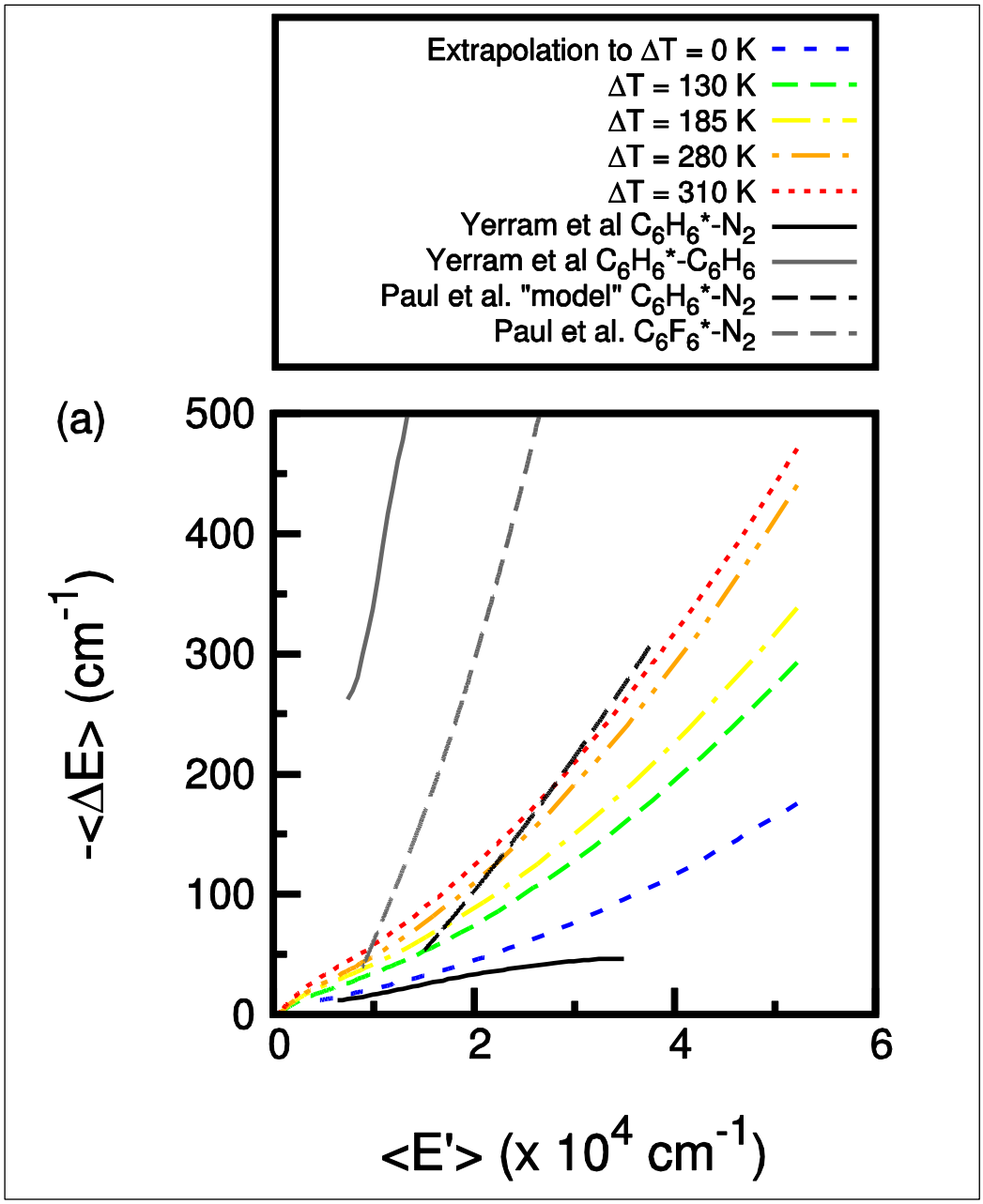

FIG. 52. (a) Average energy transferred per collision vs. average vibrational energy of C_6H_6* for models of temperature-binned temperature rises. (b) log plot of (a). Our experimental data was plotted alongside reconstructed IRF data adapted with permission from M. L. Yerram, J. D. Brenner, K. D. King, and J. R. Barker, J. Phys. Chem. 94, 6341 (1990), Copyright 1990, American Chemical Society, as well as fit curves to simulations adapted with permission from A. K. Paul, S. C. Kohale, and W. L. Hase, The J. Phys. Chem. C. 119, 14683 (2015), Copyright 2015, American Chemical Society.

Figure 52 shows that the magnitude of <*ΔE*> increases with both <*E'*> and final bath temperature. The effect of <*ΔE*> dependence on CET is also demonstrated in Figure 53 that shows that collisions that transfer larger amounts of energy are more likely at higher internal energies of highly vibrationally excited benzene.

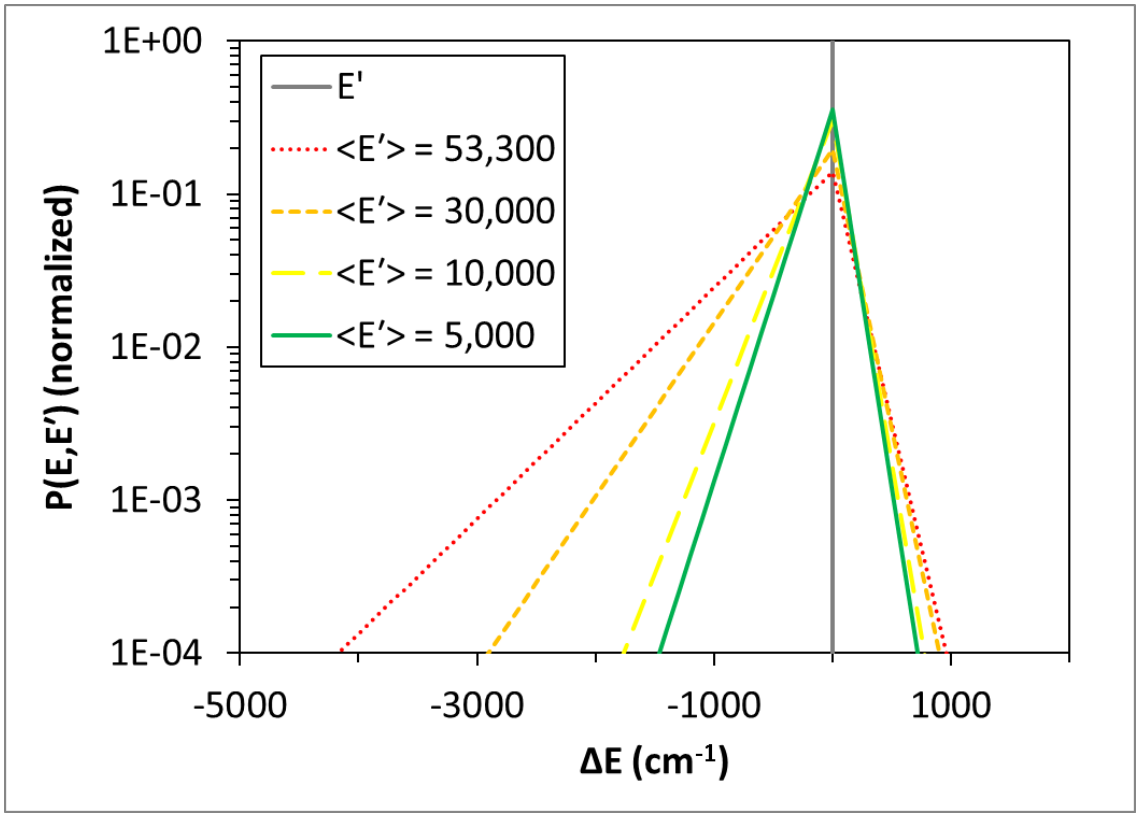

FIG. 53. Single exponential down P(E,E') functions plotted for varying benzene internal energy utilizing the CET parameters fit by the ΔT = 130 K data.

Data from Yerram *et al.*: C_6H_6*-N_2 and C_6H_6*-C_6H_6 IRF CET measurements is also reproduced in Figure 52.[36] Our experimental C_6H_6*-N_2 <*ΔE*> data is larger in magnitude than the C_6H_6*-N_2 IRF data and smaller in magnitude than the C_6H_6*-C_6H_6 IRF data for all

<*E'*> values. However, since the magnitude of our <*ΔE*> data decreases with decreasing final bath temperature, we also generated an extrapolation to the -<*ΔE*> vs <*E'*> curve that we would expect from a ΔT = 0 K experiment. The extrapolated curve was made by linearly fitting the optimized C_0 and C_1 parameters as a function of ΔT and then running a MultiWell simulation with the ΔT = 0 K extrapolated C_0 and C_1 values. The extrapolated -<*ΔE*> vs <*E'*> curve is in very good agreement with the C_6H_6*-N_2 IRF data, falling within the error bars of that data for most reported <*E'*> values. Also, given the CET rate dependence on bath temperature that we observe, it is to be expected that our experimental C_6H_6*-N_2 -<*ΔE*> data is larger than the C_6H_6*-N_2 IRF data since the IRF CET data was collected in a dilute enough mixture to cause negligible rise in bath temperature.

Fits to recent classical trajectory calculations of C_6F_6*-N_2 and "model" C_6H_6*-N_2 CET by Paul *et al.* are also included in Figure 52.[15, 16] The simulations were carried out in a regime in which the rise in bath temperature during the simulation is < 10 K and therefore the CET efficiency was not significantly affected by changes in bath temperature. The simulations also represent the regime in which there is no C_6F_6*-C_6F_6 or C_6H_6*-C_6H_6 CET since they were carried out with only one C_6F_6 or C_6H_6 molecule in a N_2 bath. The C_6F_6*-N_2 <*ΔE*> values that the authors obtained is larger than the <*ΔE*> values predicted by extrapolation of our C_6H_6*-N_2 <*ΔE*> data to ΔT = 0 K as expected. Previous work has demonstrated that C_6F_6 CET is more efficient than C_6H_6 CET largely due to the decrease in vibrational frequencies as well as increase in steepness of the

repulsive region of the intermolecular potentials upon fluorination of benzene.[10] The "model" C_6H_6*-N_2 <*ΔE*> values are also larger than the <*ΔE*> values predicted by the extrapolation of our C_6H_6*-N_2 <*ΔE*> data to *ΔT* = 0 K. The "model C_6H_6" utilized C_6H_6 atomic masses but retained the C_6F_6 intermolecular potentials. Utilization of C_6H_6 atomic masses decreased the CET efficiency due to an increase in vibrational frequencies which has been shown to decrease CET efficiency in other studies.[10, 13] However, utilization of C_6F_6-N_2 intermolecular potentials resulted in an increase in CET as compared to C_6H_6-N_2 intermolecular potentials since C_6F_6-N_2 intermolecular potentials have a steeper repulsive wall which has been shown to increase CET efficiency in impulsive collisions.[10, 99] Furthermore, unpublished results from the calculation of "real" C_6H_6*-N_2 CET by Paul *et al.* utilizing C_6H_6 atomic masses, intramolecular potentials, and intermolecular potentials yielded <*ΔE*> values that are lower than "model" C_6H_6*-N_2 <*ΔE*> values.

Measurements by Yerram *et al.* of C_6H_6*-N_2 and C_6H_6*-Ar IRF CET also suggest that CET efficiency is similar in magnitude throughout the relaxation of benzene.[36] In work by Lenzer et al., C_6H_6*-Ar <*ΔE*> was approximately -50 cm^{-1} for bath temperature of 300 K with an <*E'*> of 40700 cm^{-1}.[10] This value is consistent with an extrapolation of Yerram *et al.* C_6H_6*-N_2 <*ΔE*> values in Figure 52. In classical trajectory calculations by Bernshtein et al., C_6H_6*-Ar <*ΔE*> values were -44 cm^{-1} and -53 cm^{-1} for bath temperatures of 300 K and 500 K given an <*E'*> of 40,700 cm^{-1}.[23] This is a 20% increase in C_6H_6*-Ar CET efficiency when the bath temperature is increased from 300 K to 500 K which is consistent with the trend we observe in C_6H_6*-N_2 CET. The authors also determined that

C_6H_6*-C_6H_6 $\langle \Delta E \rangle$ values were -755 cm^{-1} and -713 cm^{-1} for bath temperatures of 300 K and 500 K respectively given an $\langle E' \rangle$ of 40,700 cm^{-1}.[23] This is a 5.6% decrease in C_6H_6*-C_6H_6 CET efficiency when the bath temperature is increased from 300 K to 500 K indicating that the total energy transfer from excited benzene to unexcited benzene becomes less significant at higher temperatures.

CET Bath Temperature Dependence

Since the average initial energy transferred from a deactivating collision, $\langle \Delta E_d \rangle$ in Equation 6, is often reported in studies utilizing a master equation treatment as well as in CET studies, we report a plot of $\langle \Delta E_d \rangle$ values versus final temperature of the temperature rise in Figure 54.

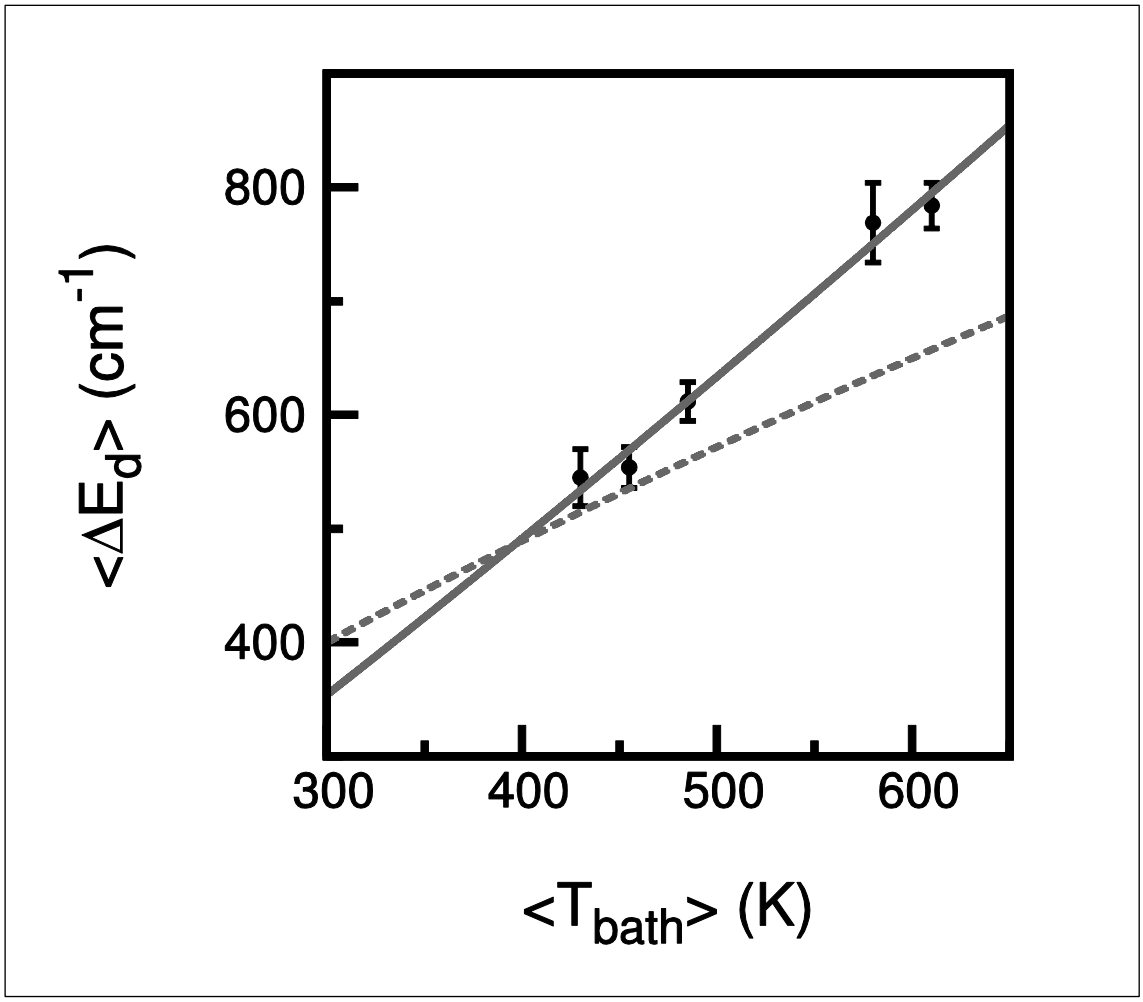

FIG. 54. Initial $\langle \Delta E_d \rangle$ values (black circles) for temperature rises to given average final temperatures between 3 – 6 μs and fit equation $\langle \Delta E_d \rangle = 354*(T_{final}/300)^{1.14}$ cm^{-1} (solid grey line). Error bars represent error in $\alpha_1(E')$ values in Table 5. Also plotted is the temperature dependent $\langle \Delta E_d \rangle$ utilized by Miller *et al.*, $\langle \Delta E_d \rangle = 400*(T_{final}/300)^{0.7}$ cm^{-1} (dashed grey line).[57]

To generate this figure, the parameters in Table 5 were utilized for the P_{down} equation, Equation 4, when calculating the $\langle \Delta E_d \rangle$ values at the assumed $\langle E' \rangle$ value of 51,813 cm^{-1}. Therefore the $\langle \Delta E_d \rangle$ values we present in Figure 54 are from collisions from nascent 193

nm photoexcited benzene to a bath at the extrapolated initial temperature values between 400 K and 650 K. The temperature dependence of deactivating collisions can also be seen in the plots of *P(E,E')*, shown in Figure 55, obtained from utilizing CET fit parameters from temperature rises to varying final temperature.

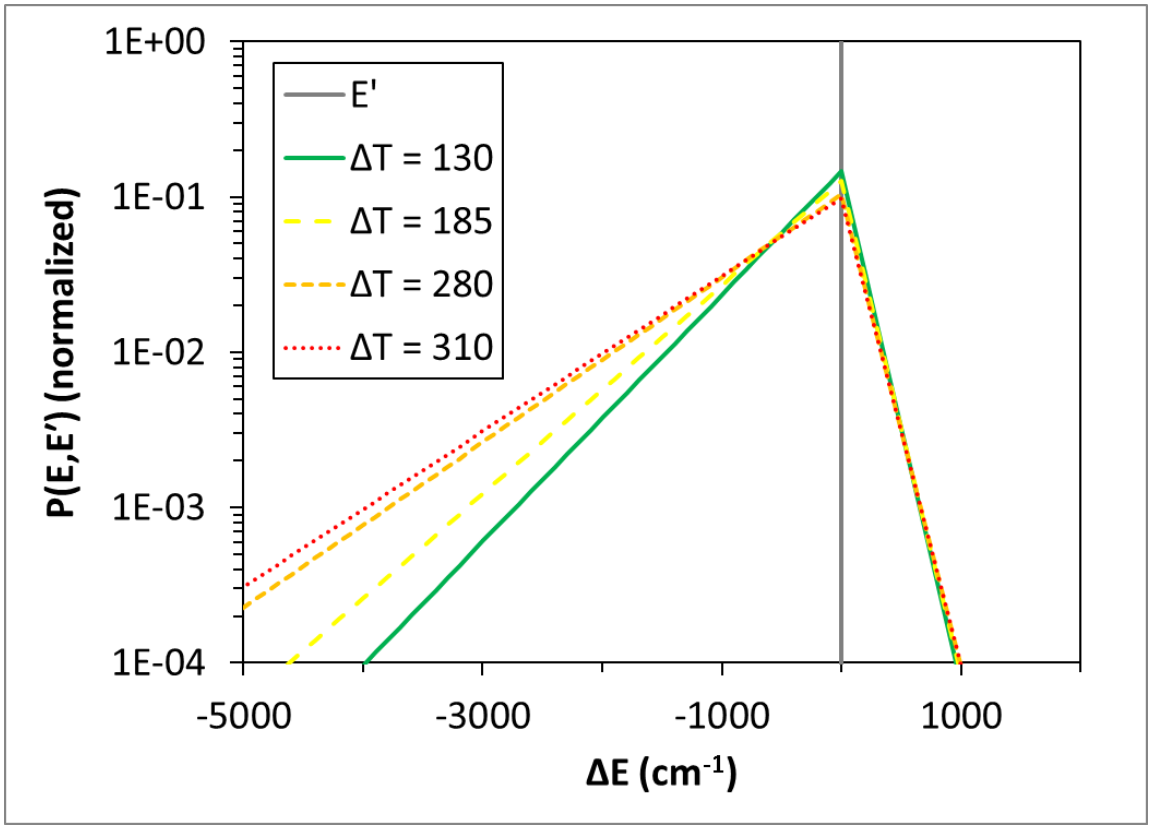

FIG. 55. Single exponential down P(E,E') functions plotted for the initial collision for temperature rises to varying final temperature.

In Figure 55 the *P(E,E')* curves demonstrate that highly vibrationally excited benzene is more likely to transfer larger amounts of energy in deactivating collisions as the bath temperature is increased.

The extrapolated value of $\langle \Delta E_d \rangle$ that we predict at 300 K is 354 cm^{-1} which is smaller than the value of 400 cm^{-1} utilized by Miller *et al* at 300 K.[57] However, our $\langle \Delta E_d \rangle$ fit increases more quickly with temperature than the fit by Miller *et al*.[57] It is also important to note that Miller *et al.* did not utilize an internal energy dependence in their CET rate modeling. For comparison to classical trajectory calculations by Bernshtein *et al*., we also generated the fit of our $\langle \Delta E_d \rangle$ values, $\langle \Delta E_d \rangle = 300*(T_{final}/300)^{1.12}$ cm^{-1}, given an $\langle E' \rangle$ of 40,700 cm^{-1}.[23] Bernshtein et al. reported C_6H_6*-Ar $\langle \Delta E_d \rangle$ values of 182 cm^{-1} and 249 cm^{-1} for bath temperatures of 300 K and 500 K respectively given an initial benzene $\langle E' \rangle$ of 40,700 cm^{-1} in classical trajectory calculations. This corresponds to a 36% increase in C_6H_6*-Ar $\langle \Delta E_d \rangle$ when the bath temperature is increased from 300 K to 500 K which is consistent with the trend we see in C_6H_6*-N_2 CET. However, the C_6H_6*-Ar $\langle \Delta E_d \rangle$ is substantially lower than the C_6H_6*-N_2 $\langle \Delta E_d \rangle$ of 300 cm^{-1} obtained from extrapolating our fit to 300 K given an $\langle E' \rangle$ of 40,700 cm^{-1}.

Summary

Benzene LINE was characterized for temperatures between 300 K - 700 K and for benzene internal energies < 51,813 cm^{-1}. The rate of $C_6H_6^*$-N_2 V-RT CET in these flow field conditions was determined to be linearly dependent on benzene internal excitation as well as approximately linearly dependent on bath temperature. This implies that

factors like flow field temperature, wavelength of benzene excitation, and magnitude of temperature rise can affect the rate of $C_6H_6^*$-N_2 V-RT CET that is produced when utilizing benzene LINE in supersonic and hypersonic flow fields. It also allows for the rate and magnitude of benzene LINE to be controllably varied by varying the $[C_6H_6]$, the pump laser power, the pump laser wavelength, or all of these factors in order to test how both the rate and magnitude of CET affects macroscopic flow field properties like turbulent fluctuations in velocity.

CHAPTER VI

PROJECT II: LOW TEMPERATURE LINE

Many supersonic and hypersonic flow field facilities operate with flow fields between approximately 10 K and 300 K, so it is important that experimental difficulties of low temperature benzene LINE are accounted for before benzene LINE can be implemented in these facilities. First, the increase in dimer formation rate as bath temperature decreases limits the maximum concentration of benzene that can be seeded into supersonic and hypersonic flow fields. Additionally, the low temperature behavior of the $C_6H_6^*$-N_2 CET rate is not well studied, so it was unclear if the temperature dependence of $C_6H_6^*$-N_2 CET could be extrapolated to temperatures below 300 K. Therefore, the characterization of low temperature $C_6H_6^*$-N_2 CET was necessary in order to determine how it can be utilized for the generation of benzene LINE.

Experimental Setup

Low temperature CET measurements were conducted in the rPHT cell. In transient temperature rise measurements, NO two-line Planar Laser Induced Fluorescence (PLIF) transient temperatures were determined utilizing the $Q_{22} + R_{12}$ (2.5) and $P_{22} + Q_{12}$(14.5) transitions $A^2\Sigma^+$ (v′ = 0) $\leftarrow X^2\Pi_{1/2}$ (v′′ = 0) band, due to their large S/N and temperature sensitivity between 140 K and 300 K. Bath temperatures were evaluated with Equation 23 where the value of C_{12} was determined by measuring the fluorescence intensities of the bath at room temperature. Two-line temperature values

were also checked by scanning the 226.5-226.8 nm NO LIF region and performing least-squares fits to simulations in LIFBASE for scans between 140 K and 300 K.[81] The scans also demonstrated that the system was thermalized at the measured pump-probe delays.

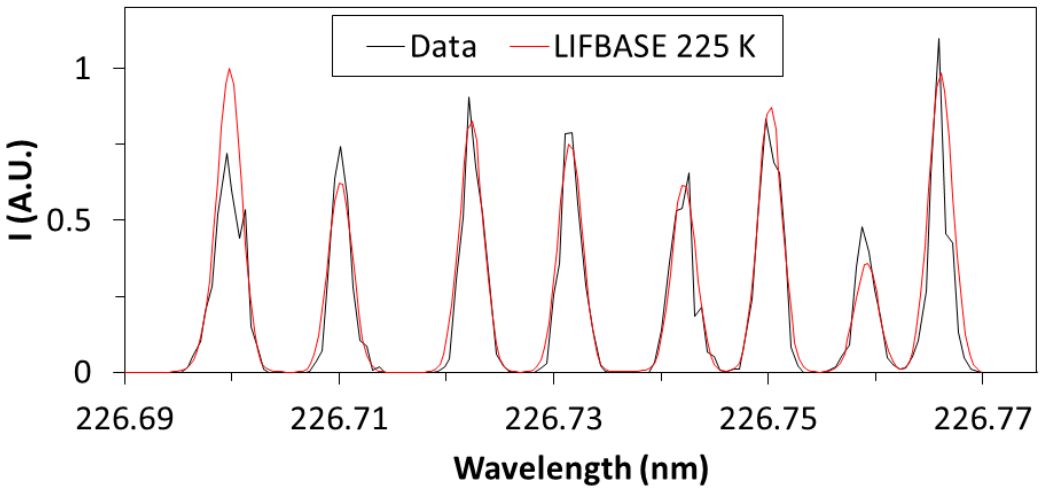

FIG. 56. Binned 3x3 pixel NO LIF scan and LIFBASE simulation at 225 K.

We observed that >95% of the short-term temperature rise occurred by 10 µs after the pump beam. Diffusion of C_6H_6* was calculated to be 11.0 µm/µs and 15.7 µm/µs at 140 K and 300 K respectively for the lowest pressure conditions tested and only significantly affected temperature measurements after approximately 15 µs.

Benzene Condensation

Condensation of benzene at low temperatures has the potential to affect flow field properties as well as CET properties in a benzene LINE experiment. Any condensation can cause a decrease in Mach number for supersonic flow fields (or increase for hypersonic flow fields) and also an increase in temperature of the flow field due to energy released in the condensation process.[100] Therefore the density of the bath can be altered by seeding benzene into rPHT-cell-based low-temperature experiments. Also, if benzene dimers, trimers, higher order oligomers, or clusters form then some of the energy from highly vibrationally excited benzene will be lost to the dissociation of condensed benzene and less energy will be available for the $C_6H_6^*$-N_2 V-RT CET that is desired for the generation of benzene LINE.

Another problem that was caused by benzene dimers, trimers, higher order oligomers, or clusters was multiphoton effects observed in the NO LIF. An example measurement demonstrating multiphoton effects is shown in Figure 57.

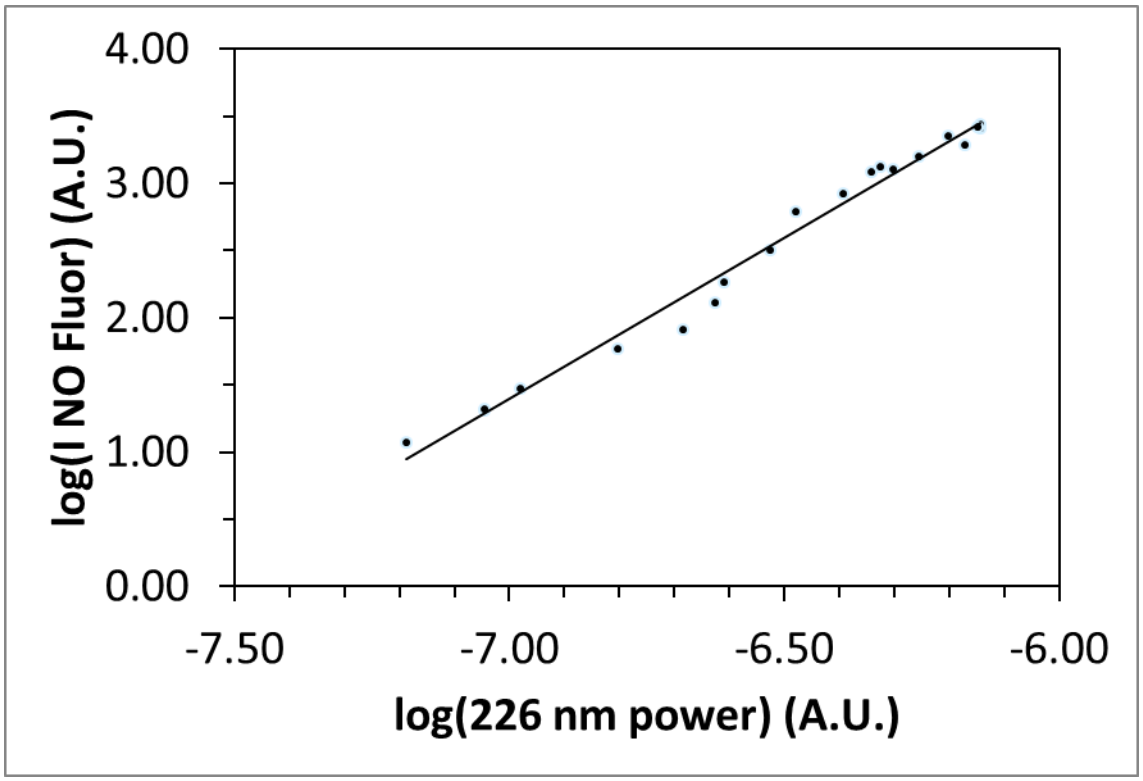

FIG. 57. Log of NO LIF signal vs probe laser power with a slope of 2.39 demonstrating multiphoton effects in a 56 K flow field caused by cluster formation.

This nonlinear dependence of LIF signal on probe laser power made the methods utilized to measure temperature through LIF in this dissertation unreliable under flow field conditions where clusters exist. Therefore, two methods of reducing dimers, trimers, higher order oligomers, and clusters that were next attempted were the design of shorter nozzles and heated settling regions based on estimates of the kinetic rates of dimer formation such that only a very low percentage of benzene molecules would form dimers between the nozzle throat and furthest location downstream from the nozzle throat that that flow field was measured with NO LIF.

The theory of benzene dimer formation rates utilized to estimate the extent of dimerization in low temperature flow fields in this dissertation was published by the Smith group.[92] In that work, the authors utilized LIF based methods for determining the rate of benzene dimer formation in a He bath. The rates measured in that work were estimated to be within a factor of two of the real dimer formation rate and each measurement was only conducted at a limited number of pressure conditions, so the pressure dependence of the benzene dimer formation rate is not known. Therefore, rates in the work of the Smith group were utilized to obtain rough estimates of the degree of benzene dimer formation in low temperature N_2 flow fields (though the dimer formation rate in a N_2 bath is likely higher since a N_2 bath is more effective at collisionally stabilizing benzene dimer complexes than a He bath). Experimental conditions were then chosen such that only few percent of benzene dimers were expected to exist in the flow fields.

As an example, if the number density of benzene is $N_{C6H6} = 8.7x10^{14}$ cm^{-3} in a nitrogen flow field with a number density of $N_{N2+C6H6} = 6.9x10^{16}$ cm^{-3} (1.25% C_6H_6 in N_2) at 140 K and the estimated pressure dependent benzene dimer formation rate of $k(T=123K) = 2.0x10^{-30}$ cm^6 s^{-1} from the work of the Smith group is utilized, then 96% of benzene in the flow field would still be monomers (as much as 4% would be dimers) at 10.0 cm downstream from the nozzle throat assuming a simplifying approximation that the gas instantly cools to 140 K when passing through the nozzle throat. Alternatively, in a 56 K flow with $N_{C6H6} = 2.2x10^{14}$ cm^{-3}, $N_{N2+C6H6} = 1.7x10^{16}$ cm^{-3} (1.25% C_6H_6 in N_2),

$k(T=49K) = 2.2x10^{-28}$ cm^6 s^{-1} then 89% of benzene in the flow field would still be monomers (as much as 11% would be dimers) at 5.5 cm downstream from the nozzle. Therefore, the flow field pressure, temperature, and length of the nozzles that generated the flow fields were selected in order to minimize the dimerization of benzene in the region of the flow field that was measured. A photo of an attempt at making a shorter M4.8 nozzle is shown in Figure 19. Unfortunately, The Mach number of this nozzle ended up being larger than the Mach number that it was designed to produce, so this nozzle produced flow fields that were colder than anticipated and therefore did not accomplish the goal of sufficiently reducing the benzene dimer formation in the flow field.

Another way that the effect of dimerization was monitored was by heating the settling region and measuring the temperature of the settling region and the flow field. Since the temperature change in the flow field due to the minimal formation of benzene dimers given ~1.25% benzene is estimated to be smaller than the error bars of the temperature measurements made in this dissertation, it was assumed that any change in the temperature of the flow field was due to change in the Mach number of the flow field due to condensation. Therefore, with a 300 K settling region, the M2.9 nozzle yielded a flow field temperature of 95.9 ± 5.2 K and with the addition of 1.25% benzene the flow field temperature increased to 118.8 ± 3.1 K indicating that benzene condensation effectively changed the Mach number to 2.77. However, when the settling region was then heated, the rate of dimerization was reduced and the effects of

condensation were reduced. The condensation effects were found to be minimized once the flow field was heated to about 140 K through this method.

For flow fields that were designed to have minimal benzene dimer formation, the effect of benzene dimer formation on CET properties was verified to be negligible by checking that the maximum temperature of the temperature rises was linear with concentration of benzene and that the curvature of the temperature rises did not vary for temperature rises to the same final temperature from differing benzene concentration and 193 nm laser power.

Bath Density Determination

Since the density of the bath is affected by the condensation of benzene, the bath density of each flow field was determined through temperature-dependent NO self-quenching measurements. Averaged NO LIF decays were obtained for flow fields of varying concentrations of NO, between 1-30% NO, as shown in Figure 58.

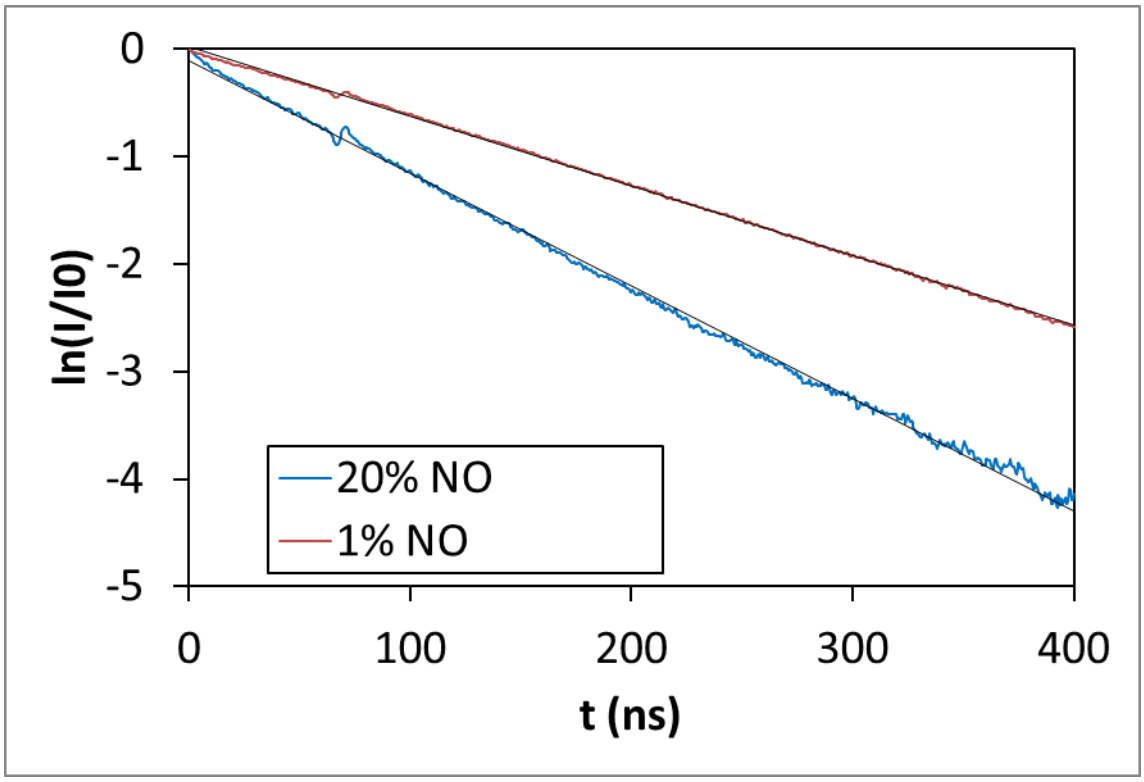

FIG. 58. 500 shot averaged NO LIF decays for 140 K flow fields of varying concentration of NO.

There was a small bump in the decay at 67 ns from ringing that did not significantly affect the fitting of the decays. The rate of NO LIF decay, k_{tot}, was then plotted vs fraction of NO in Figure 59.

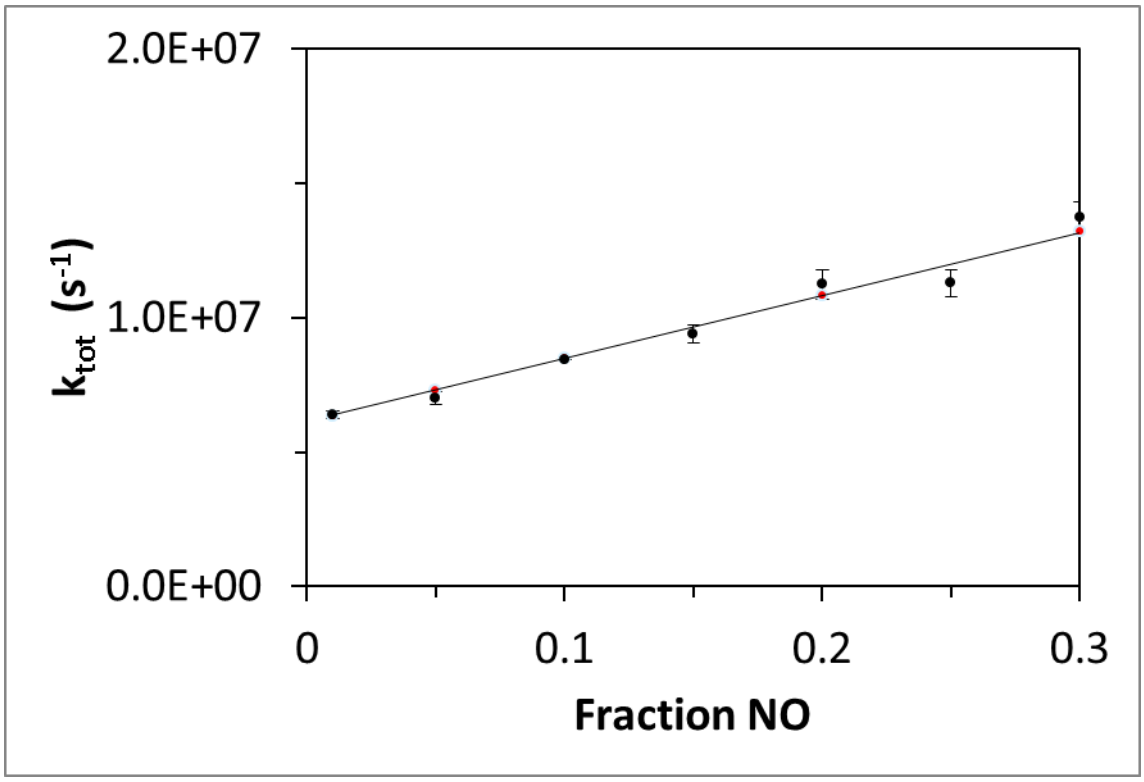

FIG. 59. Rate of NO LIF decay vs fraction of NO in flow field at 140 K.

From the slope of Figure 59, the bath density at 140 K was determined to be $1.141 \times 10^{17} \pm 8.2 \times 10^{15}$ cm^{-3} from ρ_{bath} = slope/$k_{q,NO}(T)$.

Results

Spatially-sensitive, integrated NO LIF signals were collected via pixel-dependent signal from iCCD camera images as shown in Figure 60.

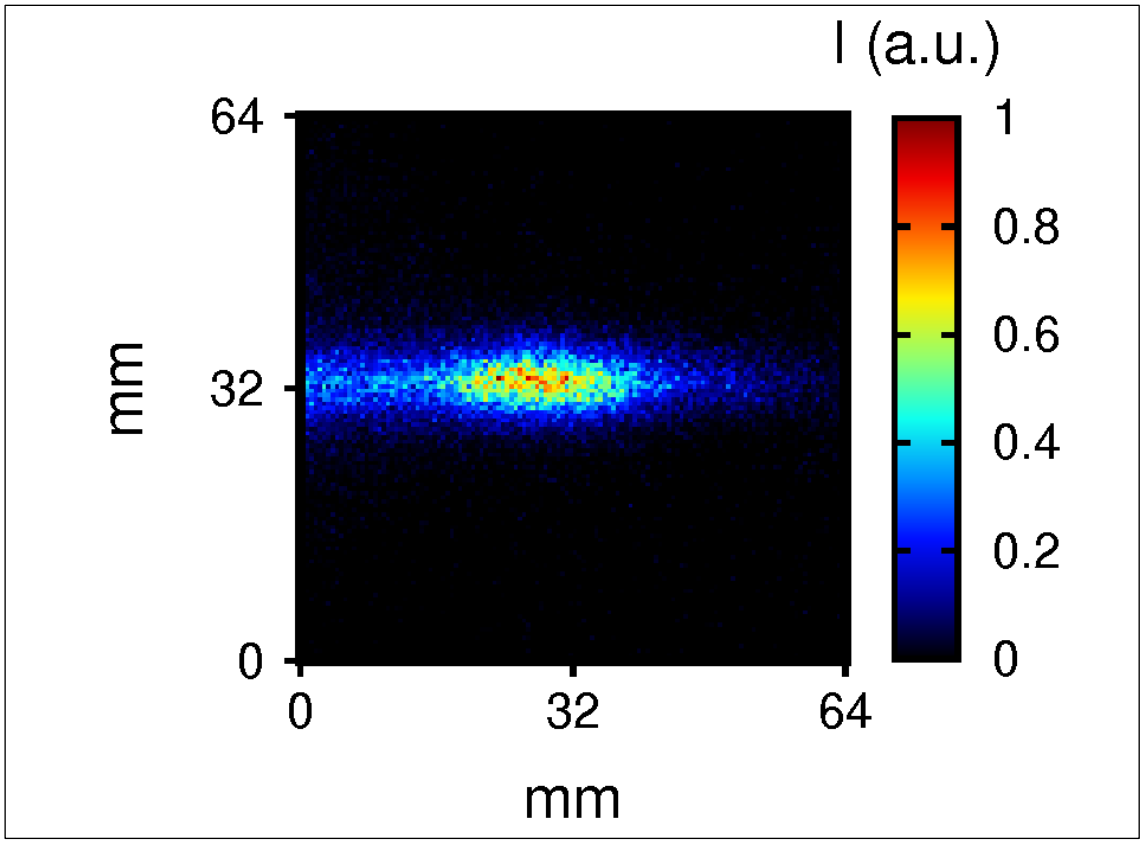

FIG. 60. Raw image for a bath at 140 K at a pump-probe time delay of 10 μs.

In Figure 60 the exit of the de Laval nozzle is located just outside the left side of this image, and the flow field gas in the image is traveling from left to right. Therefore, the pumped region of the flow field moves from left to right in the image window with increase in pump-probe time delay. Also, the probe laser enters the image window from right to left and is approximately 7 mm in height (FWHM of an approximately Gaussian profile) along the center of the image. Additionally, in Figure 60 in the region from approximately 25 - 35 mm from the nozzle exit the integrated NO LIF signal is more

intense since this is the pumped region of the flow field that is at a higher temperature than the free stream gas. This region has moved approximately 20 mm in 10 μs.

Since the velocity of the flow field is known, time dependent temperature measurements can be determined from a moving volume of gas. In order to calculate the number of pixels that the pumped volume of gas has shifted over a given time delay, it is necessary to utilize a calibration dot card placed in the image plane with a mercury pen lamp behind it in order to calculate the length in mm of each pixel while the flow field is not running. Then it is possible to calculate the shift in pixels that a volume of gas has moved over a given time delay. Therefore, in order to track the time dependent temperature rise of a given volume of gas, temperature measurements have to be made at the appropriate pixel location for each time delay. A plot of the temperature rise from the average of 3x3 binned pixel temperature measurements is shown in Figure 61.

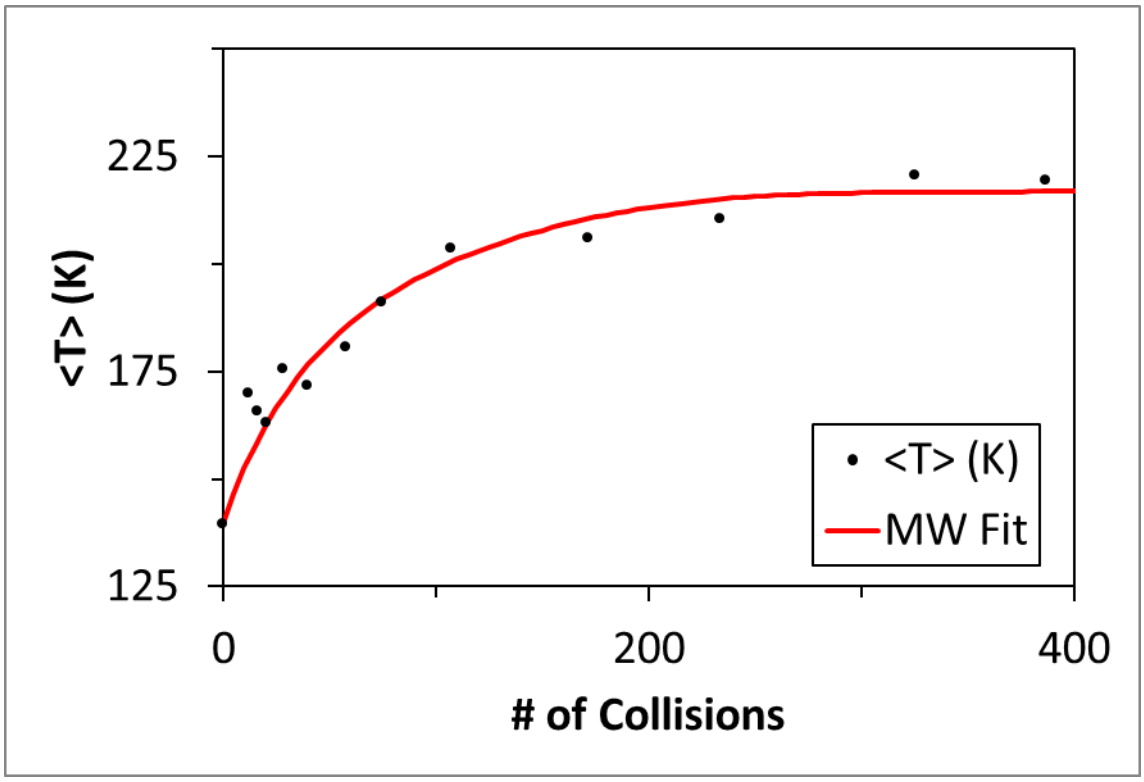

FIG. 61. Temperature rise from a T_0 = 140 K flow field.

The temperature rise in Figure 61 reached 95% of its maximum value by 10 µs. Low T_0 Temperature rises were fit in the same way that temperature rises initially at room temperature were fit in Chapter V except with a few modifications. The MultiWell simulations were conducted at the initial bath temperature so that the initial distribution of vibrational energies was a distribution at the initial temperature shifted by 51,813 cm^{-1} which is a narrower distribution than at 300 K as shown in Figure 30 and Figure 36.

CET Bath Temperature Dependence

Bath temperature dependence of $C_6H_6^*$-N_2 V-RT CET was examined by comparing the optimized values of both C_0 and C_1 at an initial bath temperature of 140 K as shown in Table 6 to the obtained values of both C_0 and C_1 at an initial bath temperature of 300 K as shown in Table 5.

TABLE 6. Parameters for Equation 4 from fitting model temperature rise data to experimental temperature rises of differing initial T_{bath}.

$T_{bath,0}$ (K)	$T_{bath,f}$ (K)	C_0 (cm^{-1})	C_1 (unitless)	$\alpha_1(E')$ (cm^{-1})
140	225	306	0.0221	1483.9

Unfortunately, the data shown in shown in Table 5 is based on a fit to one temperature rise data set after which the excimer pump laser was no longer functioning. Therefore, statistical information was not obtained for these fit values. Ideally more data would have been collected for temperature rises with initial temperatures of 140 K < T_0 < 300 K in order to determine more information on the nature of the temperature dependence of the C_6H_6*-N_2 CET rate. However, comments can be made about the trend of the temperature dependence by comparing the values in Table 5 to the temperature dependence of the CET rate above 300 K. The optimized values of both C_0 and C_1 decrease with increasing bath temperature up to 300 K. This is the opposite trend as observed for optimized CET parameters between 300 K and 700 K. It is possible that the

inverse temperature dependence of the CET parameters at low temperatures indicate that another CET mechanism becomes the dominant mechanism for the collisional relaxation of highly vibrationally excited benzene at low temperatures. It is likely that V-V CET processes become more important at low temperature and that these processes can explain the inverse temperature dependence of the low temperature CET. However, the experimental technique utilized in this dissertation is not capable of determining the branching ratios between V-RT and V-V CET processes, so other experiments or possibly classical trajectory calculations will have to be conducted to determine the origin of the inverse temperature dependence.

A low temperature plot of the average energy transferred per collision, $\langle \Delta E \rangle$, versus $\langle E' \rangle$ in Figure 62 was also calculated in the same manner as Figure 50 in order to visualize how the CET efficiency varies as a function of both benzene internal energy and bath temperature.

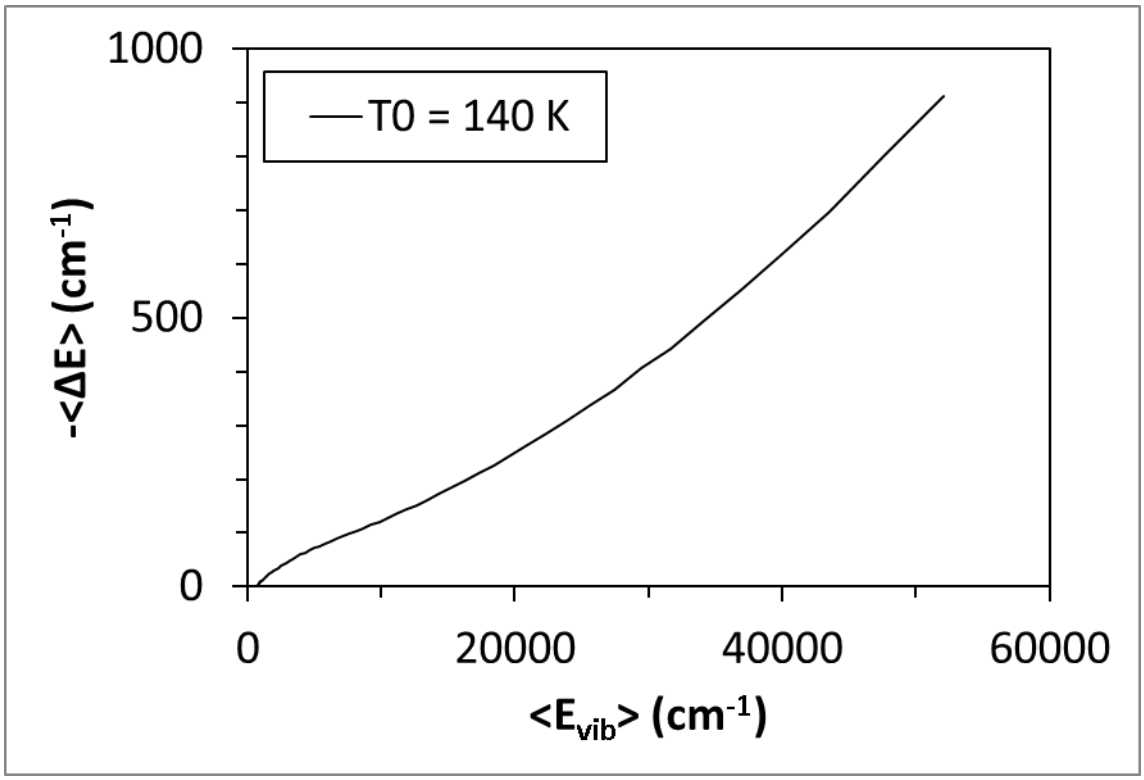

FIG. 62. Low temperature average energy transferred per collision vs. average vibrational energy of C_6H_6* from fit simulations of temperature rises.

The curvature of the low temperature curves in Figure 62 is similar to the curvature in curves above 300 K in Figure 50, except the trend of the total magnitude of $\langle \Delta E \rangle$ vs temperature is the opposite. Also, the CET rate for the 140 K curve is approximately two times larger than the CET rate for the temperature rise from 300 K to 610 K from Figure 50. Therefore, the CET rate increases more quickly per Kelvin below 300 K than it does above 300 K.

Lastly, low temperature values of $\langle \Delta E_d \rangle$ have been added to Figure 55 to yield Figure 63.

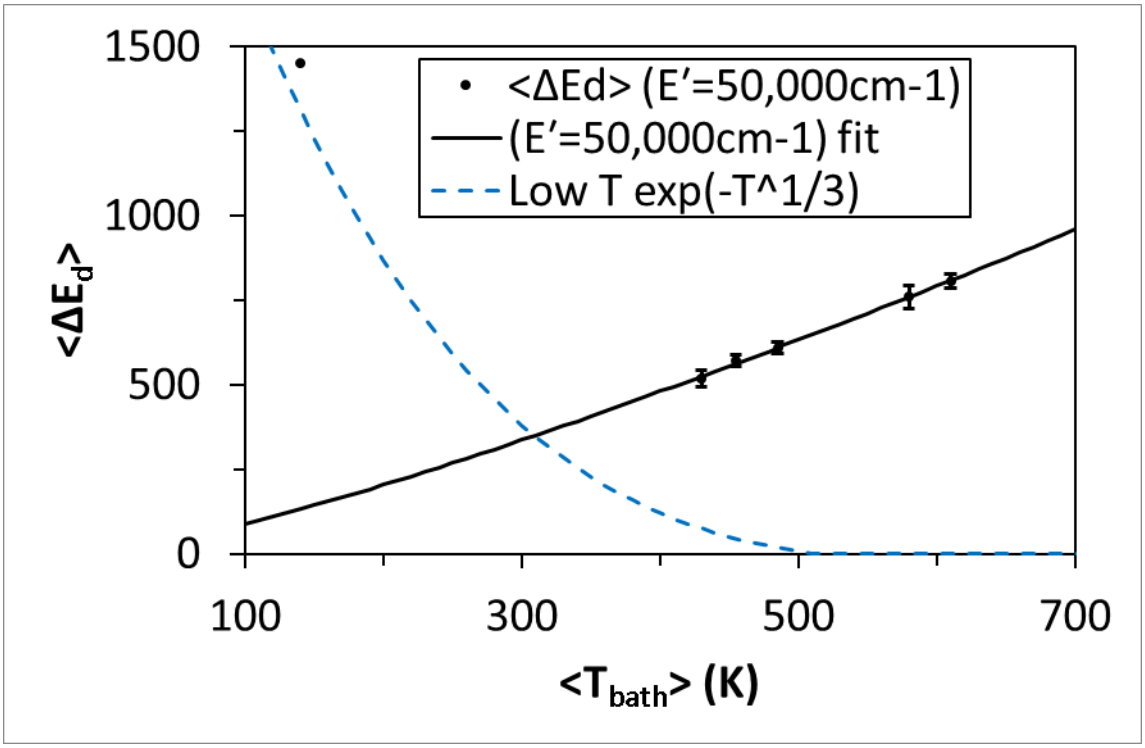

FIG. 63. Initial $\langle \Delta E_d \rangle$ values (black circles) for temperature rises to given average final temperatures and fit equation $\langle \Delta E_d \rangle = 354*(T_{final}/300)^{1.14}$ cm^{-1} (black curve). A diatomic V-V CET $exp(-T^{1/3})$ model (blue dashed curve) has also been included for reference.

In Figure 63 the $\langle \Delta E_d \rangle$ values above 300 K are reported at the final bath temperature where the CET rate is the largest and the 140 K $\langle \Delta E_d \rangle$ value was reported at the initial temperature value at 140 K where the low temperature $\langle \Delta E_d \rangle$ value would be the largest. Although the typical behavior for a diatomic-diatomic V-V CET was shown for reference (scaled based on the CET value at 140 K and the extrapolated value at 300 K) it is likely that the CET rate temperature dependence for C_6H_6-N_2 collisions is different since the mechanism for CET from C_6H_6-N_2 collisions at temperatures below 300 K are likely different than those for diatomic-diatomic collisions. For example, if C_6H_6-N_2 collisions

are dominated by "chattering" type collisions as C_6H_6- C_6H_6 collisions are, then it is possible that the increase in $\langle \Delta E_d \rangle$ with decreasing temperature is dominated by the long lifetimes of low temperature collision complexes.

Summary

The characterization of low temperature $C_6H_6^*$-N_2 CET is crucial for developing the ability to utilize benzene LINE in canonical supersonic and hypersonic flow fields. Therefore, the temperature dependence of the collisional relaxation of highly vibrationally excited benzene in a low temperature bath has been characterized. It was found that $C_6H_6^*$-N_2 CET efficiency increases with decrease in bath temperature below 300 K, which is the opposite trend as observed above 300 K. We believe that this indicates that a different mechanism of collisional relaxation of $C_6H_6^*$ may become the dominant CET pathway at low temperatures. A V-V CET pathway may be the cause of the inverse temperature dependence since V-V CET depends on long range interactions that have more time to occur in the low velocity collisions that occur at low temperatures. However, the technique utilized in this dissertation was unable to determine the branching ratios between V-RT and V-V CET, so more experiments and classical trajectory calculations are necessary in order to determine the reason for the inverse temperature dependence of $C_6H_6^*$-N_2 CET at low temperatures. Therefore, benzene LINE can now be utilized in supersonic and hypersonic flow fields as long as it does not matter that it is possible that a large percentage of the energy that benzene

absorbs upon excitation by UV light may be partitioned into vibrational energy in the flow field.

CHAPTER VII

CONCLUSIONS AND FUTURE DIRECTIONS*

In conclusion, a technique for controllably generating benzene LINE perturbations in flow fields with a range of initial bath temperatures (140 K - 600 K) has been developed. With this technique, the rate of the CET, the total magnitude of the CET, and the geometry of the perturbation can be controlled by varying factors like the concentration of benzene, the power of the pump laser, the wavelength of the pump laser, and the geometry of the pump laser. This control of the perturbation should provide a diverse set of possible conditions for experiments to determine the coupling of TNE and turbulent fluctuations in velocity in supersonic and hypersonic flow fields.

Project I: Room Temperature LINE Conclusions

In project I, benzene LINE was characterized between 300 K and 600 K. In order to do this, the time-dependent temperature rise of a N_2 bath, initially at 300 K, was measured in order to investigate the V-RT CET behavior of highly vibrationally excited benzene colliding with N_2 bath molecules. We observed a clear increase in rate of the experimental temperature rise with increase in final bath temperature which could not be described using a CET dependency on either the bath temperature or the internal

* Reprinted in part from N. A. West, J. D. Winner, R. D. W. Bowersox, and S. W. North. Resolving the Energy and Temperature Dependence of C6H6* Collisional Relaxation via Time-Dependent Bath Temperature Measurements, The Journal of Chemical Physics **145**, 014308 (2016). with the permission of AIP Publishing.

excitation of benzene independently. We find that, the best fit model of the CET depended linearly on the internal energy of the excited benzene molecules as well as depended approximately linearly on the temperature of the N_2 bath.

The V-RT CET behavior measured in this dissertation is consistent with previous excited benzene CET experiments and calculations.[15, 16, 36] In numerous previous studies the CET efficiency is modeled as increasing with increase in internal excitation as well as increasing with increase in bath temperature which is consistent with our results. In our analysis we have neglected the effect of a number of CET processes in temperature rise modeling including C_6H_6*-C_6H_6 CET and supercollisions. It is possible that C_6H_6*-C_6H_6 CET affects the rate of bath temperature rise, but C_6H_6*-C_6H_6 collisions are suspected to play a minor role in the prediction of CET to the bath in this experiment. In addition, the role of supercollisions in generating metastable highly rotationally excited N_2 is suspected to cause the energy transfer to the bath to be underestimated in our modeling. The effect of this small percentage of collisions is also suspected to increase with increase in temperature.[23] Ultimately, we believe that our model temperature rises provide a good estimate of the CET processes for > 95% of the temperature rise in the bath although there may be slower CET processes that would cause our model to underestimate the total energy transferred from highly vibrationally excited benzene to the rotation-translation modes of the N_2 bath.

Project II: Low Temperature LINE Conclusions

In project II, benzene LINE was characterized between 140 K and 300 K via pulsed converging-diverging nozzle gas expansion technique.[90] In order to do this, the time-dependent temperature rise of a N_2 bath, initially at temperatures between 140 K and 300 K, was measured in order to investigate the V-RT CET behavior of highly vibrationally excited benzene colliding with N_2 bath molecules. We observed a clear increase in rate of the experimental temperature rise with decrease in final bath temperature. This is the opposite behavior as observed at temperatures between 300 K and 600 K. There are very few studies that have examined CET dependencies on internal energy of highly vibrationally excited aromatic molecules as well as on bath temperature at this range of temperatures. It is likely that V-RT CET efficiency continued to decrease at lower temperatures in accordance with the impulsive collision model but that V-V CET efficiency dramatically increased at lower temperatures due to the increasing importance of long range interactions in CET at lower temperatures.[37] However, the technique utilized in this dissertation was not able to provide the branching ratio between the V-RT and V-V CET pathways, so more experiments and classical trajectory simulations will need to be conducted in the future in order to determine the mechanism behind the inverse temperature dependence of benzene CET at temperatures below 300 K. Therefore, benzene LINE can only be utilized in flow fields below room temperature if vibrational energy transfer does not have a significant effect on flow field properties over the length scale of the flow field.

Future Directions

Characterize Other LINE Seed Molecules

One future direction to explore would be to characterize LINE generated with different seed molecules. By modifying factors like molecular weight, number of vibrational modes, deuteration, fluorination, and internal excitation, the CET rate and magnitude can be varied to allow for more control of perturbations generated by the LINE technique in supersonic and hypersonic flow fields. Example seed molecules include: deuterated benzene (C_6D_6), halogenated benzene (C_6F_6), azulene ($C_{10}H_8$), naphthalene ($C_{10}H_8$), cycloheptatriene (C_7H_8), and pyrazine ($C_4H_4N_2$). In such cases, the CET efficiency is expected to increase with molecular size, molecular weight, vibrational frequency, and internal excitation. Therefore, LINE generated in flow fields with these molecules would create acoustic perturbations in the flow field over a smaller time/distance scale than for perturbations generated with benzene LINE.

Utilize Benzene LINE

Another possible future direction to explore would be to utilize the now characterized benzene LINE technique in supersonic and hypersonic flow fields. Benzene LINE can be "written" into canonical flow fields which are subsequently examined with the VENOM technique.[8, 9] Since the VENOM technique can instantaneously measure the bath rotational temperature and the velocity of the flow field, shot-to-shot fluctuations in velocity due to varying benzene LINE perturbations can be examined in order to

determine how macroscopic flow field properties, like turbulence, are affected by benzene LINE relaxation rate, magnitude, and geometry.

In order estimate the conditions necessary for the utilization of benzene LINE, the inverse relaxation time for highly vibrationally excited benzene was determined in order to facilitate comparisons to previous studies on the effect of collisional thermalization of molecular vibrational modes on damping of acoustic fluctuations of specific frequencies. Since the relaxation of highly vibrationally excited benzene is better fit by multi-exponential functions, the inverse relaxation time was taken as the time/number of collisions required for the average energy of highly vibrationally excited benzene to reach a fraction of 1/e of the initial energy (36.8%). The inverse relaxation time for benzene LINE conditions studied in this dissertation are shown in Table 7.

TABLE 7. Inverse relaxation time/collisions (τ) (time of relaxation to 36.8% of LINE excitation) for flow fields of varying initial temperature and final temperature.

T_0 (K)	ΔT (K)	τ (collisions)	τ (s) (M4 Ludwieg tube)[6]
300	~0	396.9	3.20×10^{-6}
300	130	221.1	1.78×10^{-6}
300	155	205.2	1.65×10^{-6}
300	185	186.3	1.50×10^{-6}
300	280	147.0	1.18×10^{-6}
300	310	133.5	1.08×10^{-6}
140	85	72.5	N/A

The inverse relaxation times were also calculated for the conditions in the flow field of the study by Schmidt and Shepherd to show how benzene LINE could affect transition in flow over a 5° angle cone with benzene/N_2 gas injected into the boundary layer (U_∞ = 670 m/s, Boundary Layer T ~ 300 K, P_∞ ~ 1.2 kPa).[6] The collision rate utilized to calculate the inverse relaxation times is $k_{L\text{-}J}(T = 300\ K) = 1.24 \times 10^8$ collisions s^{-1}. The time scale of the inverse relaxation time of benzene in this example is about 2 orders of magnitude faster than the time scale of the instability fluctuations (~6×10^4 s^{-1}) measured in the N_2 flow fields, and therefore, may not couple well with the acoustic frequencies that result in the transition to turbulence in this particular system. However, if experimental conditions are adjusted or a new experiment is devised such that benzene LINE inverse

relaxation times are closer to the acoustic frequencies that lead to transition to turbulence (~10^6 s^{-1} or other values at differing pressures), then benzene LINE might have the greatest likelihood of effectively being utilized to study the coupling of TNE with turbulent fluctuations in velocity in supersonic/hypersonic flow fields. However, this is just an initial estimate of where the benzene LINE could be most effectively utilized. Unlike the previous studies that relied on changing of seeded molecules to adjust the time scale and magnitude of vibrational relaxation, benzene LINE can produce vibrational perturbations of varying time scale and magnitude in flow fields of identical composition and therefore may be useful in previously inaccessible experimental regimes/conditions when studying the coupling of TNE and turbulence.

REFERENCES

[1]I. Leyva, S. Laurence, A. Beierholm, H. Hornung, R. Wagnild, and G. Candler, in *47th AIAA Aerospace Sciences Meeting including The New Horizons Forum and Aerospace Exposition* (American Institute of Aeronautics and Astronautics, 2009).

[2]R. Wagnild, G. Candler, I. Leyva, J. Jewell, and H. Hornung, in *48th AIAA Aerospace Sciences Meeting Including the New Horizons Forum and Aerospace Exposition* (American Institute of Aeronautics and Astronautics, 2010).

[3]R. Wagnild, G. Candler, P. Subbareddy, and H. Johnson, in *50th AIAA Aerospace Sciences Meeting including the New Horizons Forum and Aerospace Exposition* (American Institute of Aeronautics and Astronautics, 2012).

[4]J. Jewell, R. Wagnild, I. Leyva, G. Candler, and J. Shepherd, in *51st AIAA Aerospace Sciences Meeting including the New Horizons Forum and Aerospace Exposition* (American Institute of Aeronautics and Astronautics, 2013).

[5]A. V. Fedorov, V. Soudakov, and I. A. Leyva, in *7th AIAA Theoretical Fluid Mechanics Conference* (American Institute of Aeronautics and Astronautics, 2014).

[6]B. E. Schmidt, and J. Shepherd, in *54th AIAA Aerospace Sciences Meeting* (American Institute of Aeronautics and Astronautics, 2016).

[7]T. J. Fuller, A. G. Hsu, R. Sanchez-Gonzalez, J. C. Dean, S. W. North, and R. D. W. Bowersox, The Journal of Fluid Mechanics **748**, 663 (2014).

[8]R. Sanchez-Gonzalez, R. D. W. Bowersox, and S. W. North, Applied Optics **51**, 1216 (2012).

[9]R. Sanchez-Gonzalez, R. Srinivasan, R. D. W. Bowersox, and S. W. North, Optics Letters **36**, 196 (2011).

[10]T. Lenzer, K. Luther, J. Troe, R. G. Gilbert, and K. F. Lim, The Journal of Chemical Physics **103**, 626 (1995).

[11]J. D. Brenner, J. P. Erinjeri, and J. R. Barker, The Journal of Chemical Physics **175**, 99 (1993).

[12]A. J. Sedlacek, R. E. Weston, and G. W. Flynn, The Journal of Chemical Physics **94**, 6483 (1991).

[13]D. G. Mitchell, A. M. Johnson, J. A. Johnson, K. A. Judd, K. Kim, M. Mayhew, A. L. Powell, and E. T. Sevy, The Journal of Physical Chemistry A **112**, 1157 (2008).

[14]C. A. Michaels, Z. Lin, A. S. Mullin, H. C. Tapalian, and G. W. Flynn, The Journal of Chemical Physics **106**, 7055 (1997).

[15]A. K. Paul, S. C. Kohale, and W. L. Hase, The Journal of Physical Chemistry C **119**, 14683 (2015).

[16]A. K. Paul, S. C. Kohale, S. Pratihar, R. Sun, S. W. North, and W. L. Hase, The Journal of Chemical Physics **140**, 194103, 11 (2014).

[17]N. Nakashima, and K. Yoshihara, The Journal of Physical Chemistry **93**, 7763 (1989).

[18]L. Brouwer, H. Hippler, L. Lindemann, and J. Troe, The Journal of Physical Chemistry **89**, 4608 (1985).

[19]C.-L. Liu, H. C. Hsu, Y. C. Hsu, and C.-K. Ni, The Journal of Chemical Physics **127**, 104311 (2007).

[20]H. Hippler, K. Luther, J. Troe, and H. Wendelken, The Journal of Chemical Physics **79**, 239 (1983).

[21]D. K. Havey, J. A. Du, Q. N. Liu, and A. S. Mullin, The Journal of Physical Chemistry A **114**, 1569 (2010).

[22]J. Du, N. A. Sassin, D. K. Hayey, K. L. Hsu, and A. S. Mullin, The Journal of Physical Chemistry A **117**, 12104 (2013).

[23]V. Bernshtein, and I. Oref, The Journal of Physical Chemistry B **109**, 8310 (2005).

[24]Z. M. Li, R. Sansom, S. Bonella, D. F. Coker, and A. S. Mullin, The Journal of Physical Chemistry A **109**, 7657 (2005).

[25]T. Lenzer, and K. Luther, The Journal of Chemical Physics **104**, 3391 (1996).

[26]S. T. Tsai, C. K. Lin, Y. T. Lee, and C. K. Ni, The Journal of Chemical Physics **113**, 67 (2000).

[27]G. P. Smith, and J. R. Barker, Chem. Phys. Lett. **78**, 253 (1981).

[28]M. J. Rossi, and J. R. Barker, Chem. Phys. Lett. **85**, 21 (1982).

[29]M. J. Rossi, J. R. Pladziewicz, and J. R. Barker, The Journal of Chemical Physics **78**, 6695 (1983).

[30]T. Ichimura, Y. Mori, N. Nakashima, and K. Yoshihara, Chem. Phys. Lett. **104**, 533 (1984).

[31]T. Ichimura, Y. Mori, N. Nakashima, and K. Yoshihara, The Journal of Chemical Physics **83**, 117 (1985).

[32]T. Ichimura, M. Takahashi, and Y. Mori, The Journal of Chemical Physics **114**, 111 (1987).

[33]N. Nakashima, H. Inoue, M. Sumitani, and K. Yoshihara, The Journal of Chemical Physics **73**, 5976 (1980).

[34]N. Nakashima, and K. Yoshihara, The Journal of Chemical Physics **77**, 6040 (1982).

[35]N. Nakashima, and K. Yoshihara, The Journal of Chemical Physics **79**, 2727 (1983).

[36]M. L. Yerram, J. D. Brenner, K. D. King, and J. R. Barker, The Journal of Physical Chemistry **94**, 6341 (1990).

[37]J. R. Barker, L. M. Yoder, and K. D. King, The Journal of Physical Chemistry A **105**, 796 (2001).

[38]U. Hold, T. Lenzer, K. Luther, K. Reihs, and A. C. Symonds, The Journal of Chemical Physics **112**, 4076 (2000).

[39]U. Hold, T. Lenzer, K. Luther, K. Reihs, and A. C. Symonds, The Journal of Chemical Physics **112**, 4076 (2000).

[40]T. Lenzer, K. Luther, K. Reihs, and A. C. Symonds, The Journal of Chemical Physics **112**, 4090 (2000).

[41]U. Hold, T. Lenzer, K. Luther, and A. C. Symonds, The Journal of Chemical Physics **119**, 11192 (2003).

[42]V. Bernshtein, and I. Oref, The Journal of Physical Chemistry **98**, 3782 (1994).

[43]A. Pashutski, and I. Oref, The Journal of Physical Chemistry **92**, 178 (1988).

[44]S. Hassoon, I. Oref, and C. Steel, The Journal of Chemical Physics **89**, 1743 (1988).

[45]J. M. Morgulis, S. S. Sapers, C. Steel, and I. Oref, The Journal of Chemical Physics **90**, 923 (1989).

[46]K. Luther, and K. Reihs, Physical Chemistry Chemical Physics **92**, 442 (1988).

[47]H. G. Lohmannsroben, and K. Luther, Chem. Phys. Lett. **144**, 473 (1988).

[48]D. F. Kelley, T. Kasai, and B. S. Rabinovitch, The Journal of Physical Chemistry **85**, 1100 (1981).

[49]R. Arakawa, D. F. Kelley, and B. S. Rabinovitch, The Journal of Chemical Physics **76**, 2384 (1982).

[50]A. S. Mullin, J. Park, J. Z. Chou, G. W. Flynn, and R. E. Weston, The Journal of Chemical Physics **175**, 53 (1993).

[51]G. Lendvay, and G. C. Schatz, The Journal of Physical Chemistry **94**, 8864 (1990).

[52]D. L. Clarke, K. C. Thompson, and R. G. Gilbert, Chem. Phys. Lett. **182**, 357 (1991).

[53]N. J. Brown, and J. A. Miller, The Journal of Chemical Physics **80**, 5568 (1984).

[54]D. C. Clary, R. G. Gilbert, V. Bernshtein, and I. Oref, Faraday Discuss. **102**, 423 (1995).

[55]L. A. Miller, C. D. Cook, and J. R. Barker, The Journal of Chemical Physics **105**, 3012 (1996).

[56]J. A. Miller, S. J. Klippenstein, and C. Raffy, The Journal of Physical Chemistry A **106**, 4904 (2002).

[57]J. A. Miller, and S. J. Klippenstein, The Journal of Physical Chemistry A **107**, 7783 (2003).

[58]M. Klessinger, and J. Michl, *Excited States and Photochemistry of Organic Molecules* (Wiley-VCH, New York, New York, 1995).

[59]C. E. Otis, J. L. Knee, and P. M. Johnson, The Journal of Chemical Physics **78**, 2091 (1983).

[60]M. Sumitani, D. V. Oconnor, Y. Takagi, N. Nakashima, K. Kamogawa, Y. Udagawa, and K. Yoshihara, The Journal of Chemical Physics **93**, 359 (1985).

[61]M. A. Duncan, T. G. Dietz, M. G. Liverman, and R. E. Smalley, The Journal of Physical Chemistry **85**, 7 (1981).

[62]J. K. Foote, M. H. Mallon, and J. N. Pitts, The Journal of the American Chemical Society **88**, 3698 (1966).

[63]K. Shindo, and S. Lipsky, The Journal of Chemical Physics **45**, 2292 (1966).

[64]J. P. Reilly, and K. L. Kompa, The Journal of Chemical Physics **73**, 5468 (1980).

[65]A. Yokoyama, X. Zhao, E. J. Hintsa, R. E. Continetti, and Y. T. Lee, The Journal of Chemical Physics **92**, 4222 (1990).

[66]T. C. Hsu, J. N. Shu, Y. Chen, J. J. Lin, Y. T. Lee, and X. M. Yang, The Journal of the Chinese Chemical Society **49**, 1 (2002).

[67]V. V. Kislov, T. L. Nguyen, A. M. Mebel, S. H. Lin, and S. C. Smith, The Journal of Chemical Physics **120**, 7008 (2004).

[68]S. Y. Toh, P. Djuricanin, T. Momose, and J. Miyazaki, The Journal of Physical Chemistry A **119**, 2683 (2015).

[69]T. C. Hsu, J. N. Shu, Y. Chen, J. J. Lin, Y. T. Lee, and X. M. Yang, The Journal of Chemical Physics **115**, 9623 (2001).

[70]G. Herzberg, *Molecular spectra and molecular structure. Vol. 3: Electronic spectra and electronic structure of polyatomic molecules* (Van Nostrand Reinhold Company, New York, New York, 1966), Vol. 3.

[71]T. Etzkorn, B. Klotz, S. Sorensen, I. V. Patroescu, I. Barnes, K. H. Becker, and U. Platt, Atmos. Environ. **33**, 525 (1999).

[72]B. S. Olive, http://satellite.mpic.de/, (University of North Alabama, Florence, Alabama, 2015).

[73]A. Bolovinos, J. Philis, E. Pantos, P. Tsekeris, and G. Andritsopoulos, The Journal of Molecular Spectroscopy **94**, 55 (1982).

[74]B. Thompson, P. Harteck, and R. Reeves, The Journal of Geophysical Research **68**, 6431 (1963).

[75]A. C. Eckbreth, *Laser diagnostics for combustion temperature and species* (OPA, Amsterdam, 1996), Vol. 3.

[76]B. K. McMillin, (1993).

[77]A. G. Hsu, *Application of advanced laser and optical diagnostics towards non-thermochemical equilibrium systems* (Texas A&M University, 2009).

[78]T. B. Settersten, B. D. Patterson, and C. D. Carter, The Journal of Chemical Physics **130**, 204302 (2009).

[79]R. Sanchez-Gonzalez, W. D. Eveland, N. A. West, C. L. N. Mai, R. D. W. Bowersox, and S. W. North, The Journal of Chemical Physics **141**, 074313, 1 (2014).

[80]G. Herzberg, *Molecular Spectra and Molecular Structure: Volume I-Spectra of Diatomic Molecules* (Van Nostrand Reinhold, New York, 1950).

[81]J. Luque, and D. Crosley, SRI international report MP **99**, (1999).

[82]J. R. Barker, The International Journal of Chemical Kinetics **33**, 232 (2001).

[83]J. R. Barker, The International Journal of Chemical Kinetics **41**, 748 (2009).

[84]J. H. de Boer, Transactions of the Faraday Society **32**, 0010 (1936).

[85]*NIST Chemistry WebBook, NIST Standard Reference Database Number 69* 2018).

[86]A. Bolovinos, J. Philis, E. Pantos, P. Tsekeris, and G. Andritsopoulos, The Journal of Molecular Spectroscopy **94**, 55 (1982).

[87]J. Philis, A. Bolovinos, G. Andritsopoulos, E. Pantos, and P. Tsekeris, The Journal of Physics B: Atomic Molecular and Optical Physics **14**, 3621 (1981).

[88]K. Yoshino, J. R. Esmond, A. S. C. Cheung, D. E. Freeman, and W. H. Parkinson, Planet Space Sci. **40**, 185 (1992).

[89]J. D. Anderson, *Modern compressible flow: with historical perspective* (McGraw-Hill, New York, New York, 1990), Vol. 12.

[90]R. Sanchez-Gonzalez, R. Srinivasan, J. Hofferth, D. Y. Kim, A. J. Tindall, R. D. W. Bowersox, and S. W. North, AIAA Journal **50**, 691 (2012).

[91]R. Sanchez-Gonzalez, *Advanced laser diagnostics development for the characterization of gaseous high speed flows* (Texas A&M University, 2012).

[92]S. Hamon, S. D. Le Picard, A. Canosa, B. R. Rowe, and I. W. M. Smith, The Journal of Chemical Physics **112**, 4506 (2000).

[93]R. C. Reid, J. M. Prausnitz, and B. E. Poling, *The Properties of Gases and Liquids* (McGraw-Hill, New York, 1987), 4th edn.

[94]H. Hippler, J. Troe, and H. J. Wendelken, The Journal of Chemical Physics **78**, 6709 (1983).

[95]S. E. Stein, and Rabinovi.Bs, The Journal of Chemical Physics **58**, 2438 (1973).

[96]T. Beyer, and Swinehar.Df, Commun. ACM **16**, 379 (1973).

[97]S. Hay, F. Shokoohi, S. Callister, and C. Wittig, Chem. Phys. Lett. **118**, 6 (1985).

[98]N. A. West, J. D. Winner, R. D. W. Bowersox, and S. W. North, The Journal of Chemical Physics **145**, 014308 (2016).

[99]P. D. Claire, and W. L. Hase, The Journal of Physical Chemistry **100**, 8190 (1996).

[100]A. Pope, and K. L. Goin, *High-speed wind tunnel testing* (Wiley, New York, New York, 1965).

APPENDIX A

NO LIF TEMPERATURE MEASUREMENT PROGRAM*

Appendix A describes the utilization of the rotational temperature fitting LabVIEW program "Scan_Laser_And_Fit_T_Rot.vi". It therefore reviews and expands upon the concepts covered in "Boltzmann Plot Temperature from Scans" section of Chapter III.

NO LIF Temperature Fitting with Scan_Laser_And_Fit_T_Rot.vi

Obtaining a fit to the rotational temperature from a Boltzmann plot relies on the rearrangement of the rotational Boltzmann equation to obtain Equation 28. Therefore, the rotational temperature can be determined from the slope of a Boltzmann plot which plots $k_B \ln(N_J/g)$ vs the rotational energy of each state as shown in Figure 25. Since the relative populations of each state *J* is proportional to the area under the corresponding peak in a LIF scan, scans over transitions originating from many different rotational states can be utilized to determine the rotational temperature. Therefore, a program called "Scan_Laser_And_Fit_T_Rot.vi" was written to fit the scan peaks as sums of Gaussian functions in order to determine the relative population of each rotational state.

---

* Reprinted in part from N. A. West, J. D. Winner, R. D. W. Bowersox, and S. W. North. Resolving the Energy and Temperature Dependence of C6H6* Collisional Relaxation via Time-Dependent Bath Temperature Measurements, The Journal of Chemical Physics **145**, 014308 (2016). with the permission of AIP Publishing.

Once a scan is loaded into the program, the fitting algorithm, the LabVIEW Levenberg-Marquardt constrained non-linear curve fit algorithm, requires guesses and constraints for curve fitting. The initial guesses for Gaussian curve parameters are determined via cursor input from the plot, Figure 64.

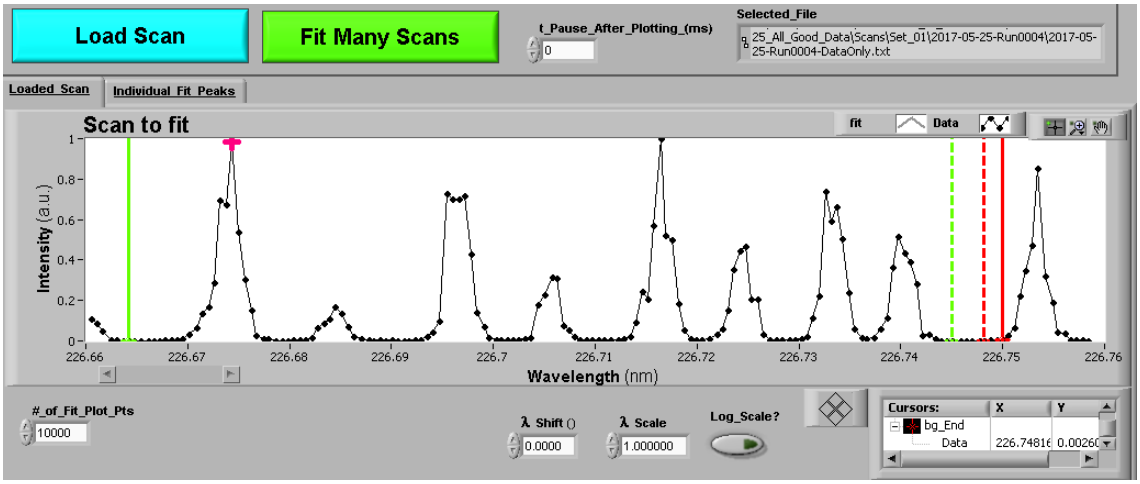

FIG. 64. An experimental scan loaded into the Scan_Laser_And_Fit_T_rot.vi LabVIEW program for analysis.

The solid green and red cursors select the start and stop of the range of data points that will be utilized to fit the Gaussian curves respectively. In Figure 64 there are 8 peaks within the range of data points, so this example scan will be fit by the sum of 8 Gaussian functions. The dashed green and red cursors select the start and stop of the range of data points that can be utilized to fit the baseline offset, via averaging all baseline points

between the dashed cursors, of the scan respectively. The constraints for the fitting parameters are set in the controls below the scan in the program shown in Figure 65.

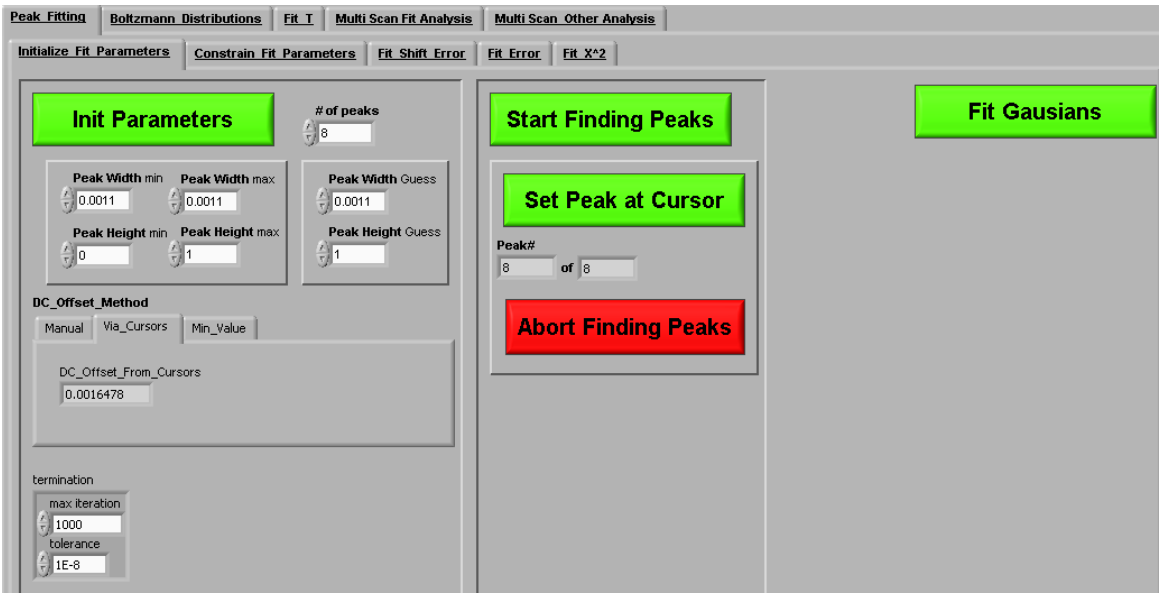

FIG. 65. The initial fit settings have been configured.

The number of peaks, max and min peak widths, max and min peak heights, and method of DC offset fitting must be selected and then the “Init Parameters” button pressed. Quick guesses for each peak’s wavelength and height can then be input from the location of each peak’s maxima. This can be done by clicking the “Start Finding Peaks” button, moving the pink cursor in Figure 65 to a peak maxima, clicking the “Set Peak at Cursor” button (or alternatively pressing the “p” key), and repeating for all peaks to be fit. At this

point, all constraints and guess parameters have been input to the program and the scan can be fit by pressing the “Fit Gaussians” button to yield the fit in Figure 66.

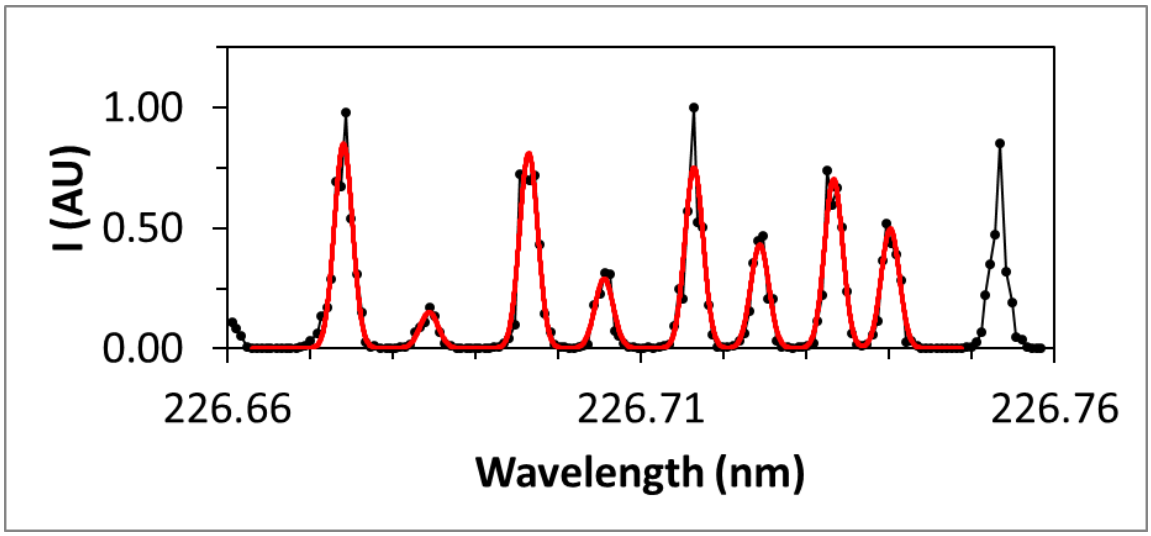

FIG. 66. A subsection of the scan (black circles/curve) has been fit with 8 Gaussians (red curve).

An example of a fit of a noisy scan with a large baseline value due to uncorrected benzene emission at a low pump-probe time delay is shown in Figure 67.

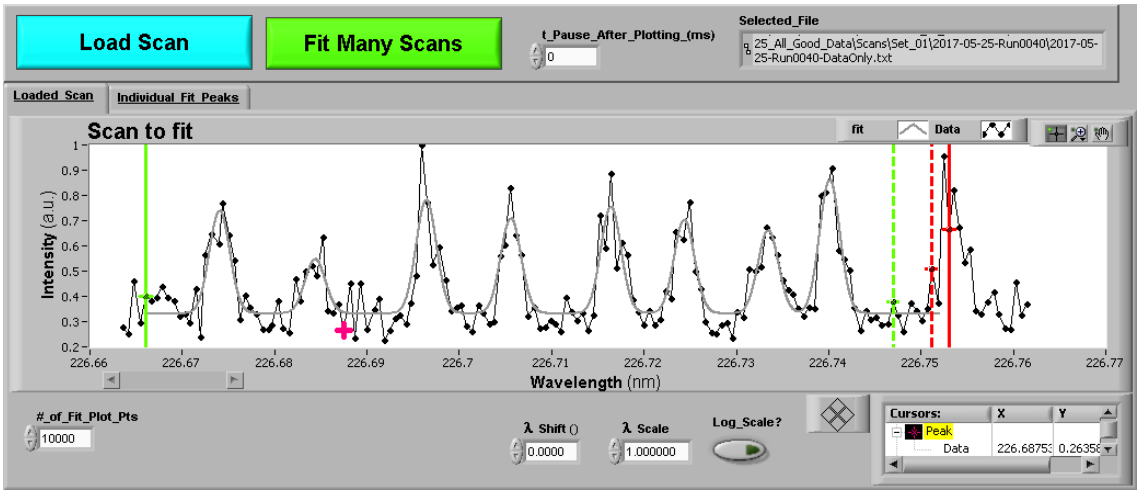

FIG. 67. Example of a fit of a noisy plot with a large baseline signal.

Constraining the baseline to the average value between the dashed cursors was crucial in this fit to obtaining the proper relative areas under all of the peaks. The relative area under each Gaussian is proportional to the width multiplied by the height of the Gaussian or, if the widths of the Gaussians are constrained, just the heights may be compared. The corresponding relative population can then be derived from the area under each peak if multiplied by a branch-specific correction factor obtained from the LIFBASE database.[81] This is performed in the temperature fitting program by assigning the *J* value and branch to each fit peak, as shown in Figure 68.

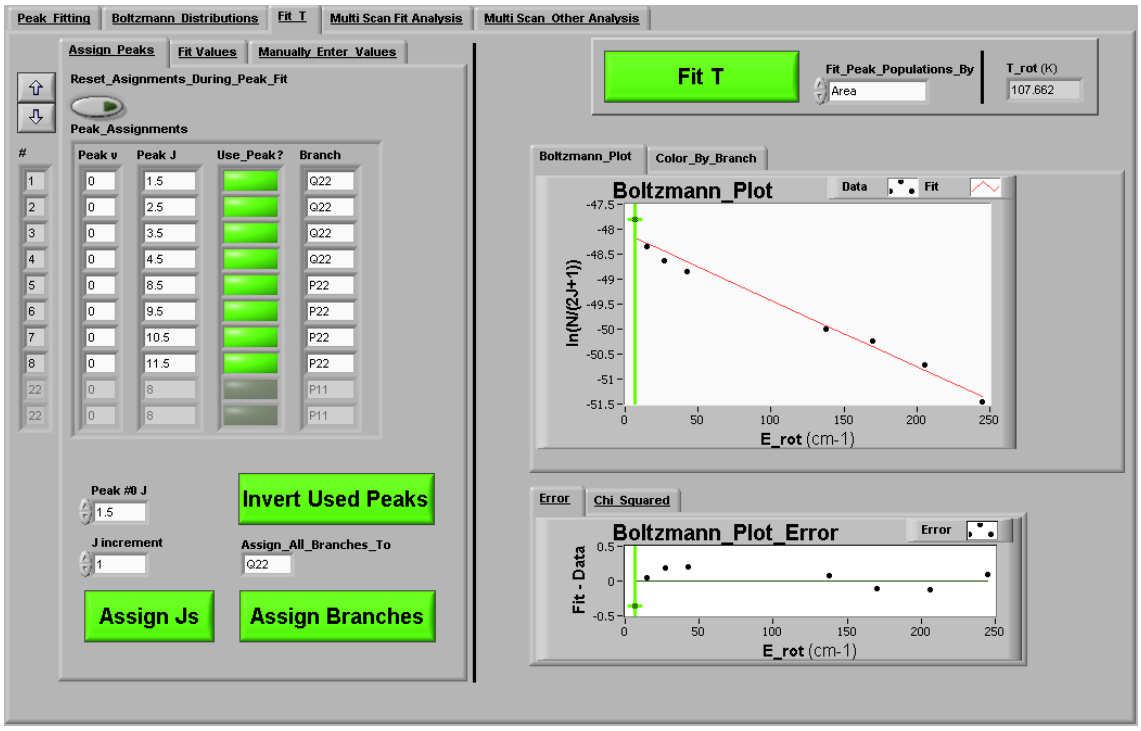

FIG. 68. Assignment of peaks for Boltzmann plot fitting with corresponding Boltzmann plot fit.

The temperature fitting program can then calculate the correction factor for each peak and obtain the relative population of each *J* state for making a Boltzmann plot. If the "Fit T" button is then pressed, a Boltzmann plot derived from the fit peaks, a fit to the Boltzmann plot, and the temperature derived from the slope of that plot are then displayed in the program as shown in Figure 68.

Since it is desirable to quickly fit the temperatures of the many scans in a data set after each data set is collected in a temperature rise experiment, a good way to accomplish this fitting while monitoring the experiment is through automation of the temperature fitting. If the same peaks are collected in every scan, then, after the first

scan is fit manually, the fit of the previous scan can be utilized to provide guess parameters in order to fit each subsequent scan. However, two problems that need to be considered to accomplish proper automation of fitting is that the peak heights will be different between the two scans if the temperature is different in the two scans and also the scans can be shifted in the wavelength that the dye laser reports for each scan point since there can be drift in the calibration of the stepper motors in the dye laser from scan to scan. An example of a shifted scan at a different temperature can be seen in Figure 69.

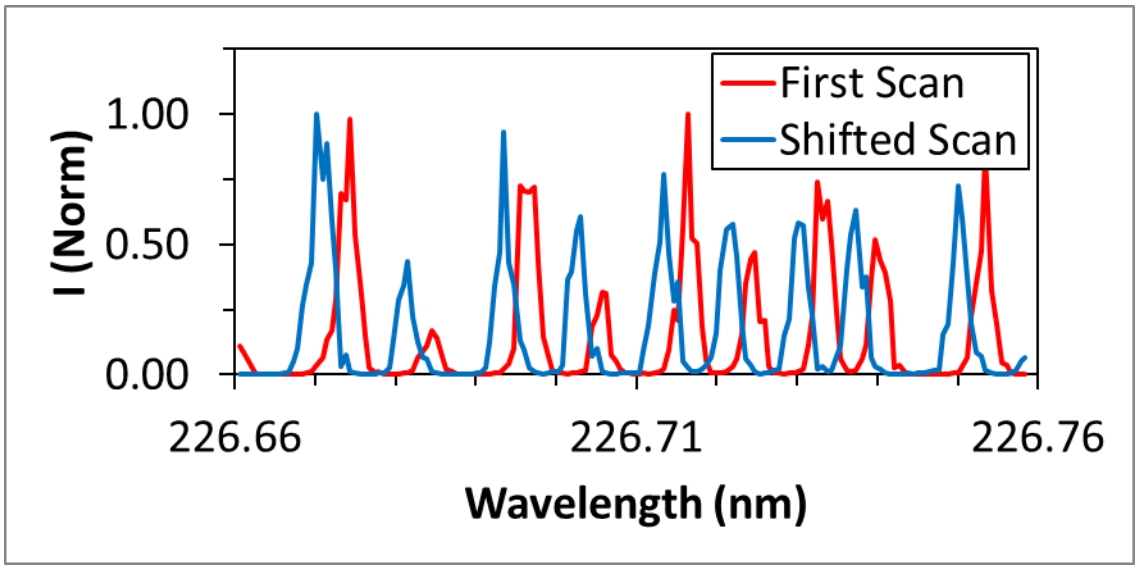

FIG. 69. Example of experimental temperature scans that are shifted in wavelength due to stepper motor drift.

Therefore, the shift in the shifted scan needs to be corrected before the Gaussian peaks are fit. In order to determine the shift between the two scans, a least squares analysis is performed between the previous scan's Gaussian fit and the current scan vs increments of scan shift that are much smaller than the width of the peaks as shown in Figure 70.

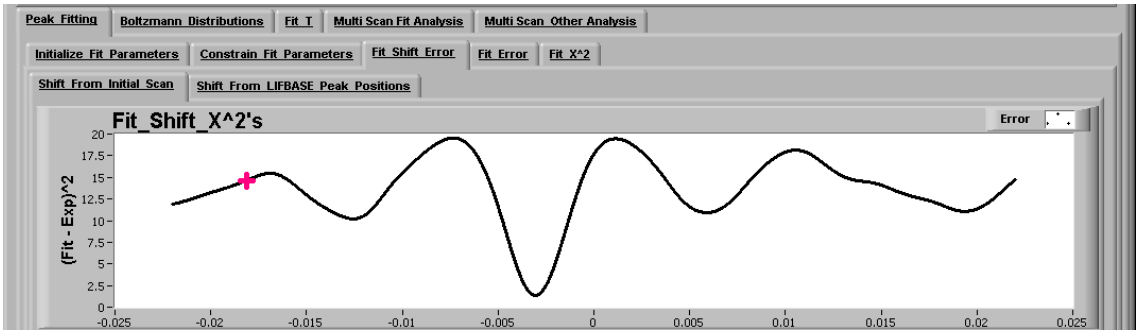

FIG. 70. Plot of X^2 values between fit and experimental scan vs shift in wavelength of the fit scan before shifting the experimental scan.

The minimum value in Figure 70 is then corresponds to the shift in the scan that is to be fit. Once shifted, the scan can then be fit utilizing the previous scan's fit parameters as the new initial guess parameters. To ensure that a sufficient shift was applied, the scan shift process is repeated with the new fit curve and then the scan is fit again. By the second iteration of the scan shifting process, the least square plot should have a minimum at 0 like in Figure 71.

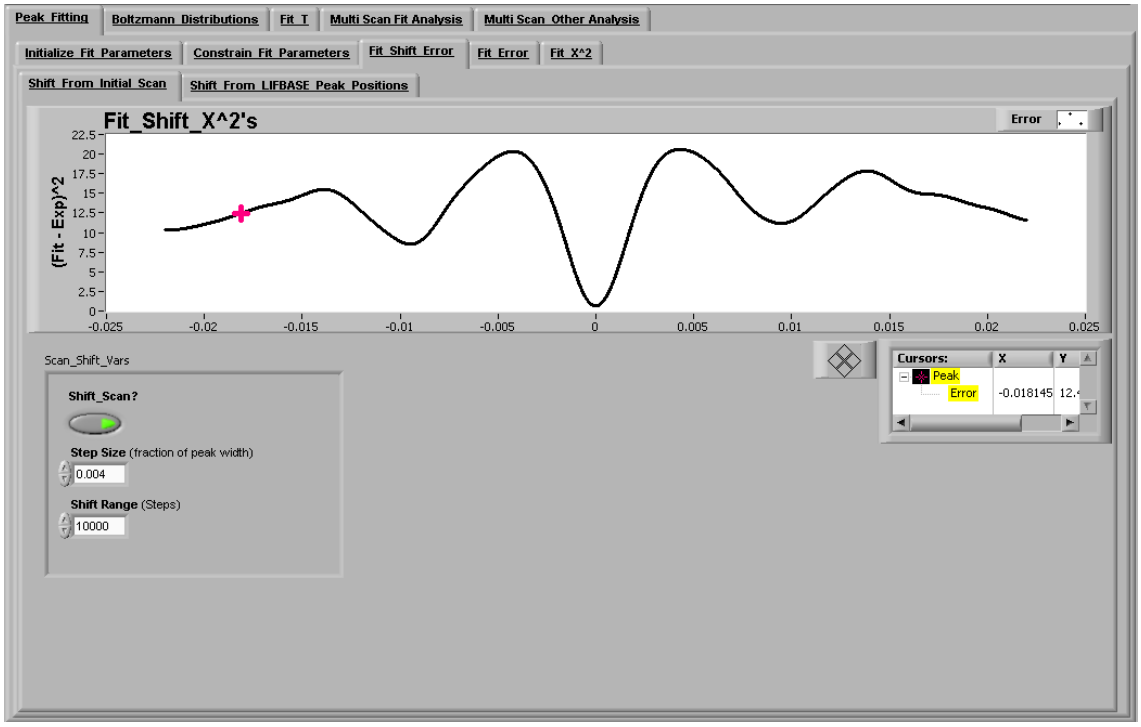

FIG. 71. Plot of X^2 values between fit and experimental scan vs shift in wavelength of the fit scan after shifting the experimental scan.

From a folder of LIF scans, the automated fitting of each scan can then yield a temperature from each Boltzmann plot linear fit. In the temperature fitting program, an array of the temperatures from the automated fitting is recorded in a text file for future analysis.

One last feature of the temperature fittting program that was utilized to verify the Boltzmann plot fits of NO LIF scans was the shifting of all of the scans to the wavelengths reported for the peaks in the LIFBASE program.[81] This was accomplished by comparing the assigned peak locations in an exported database from LIFBASE to the fit

peak locations that correspond to the center of each fit Gaussian function, as shown in Figure 72.

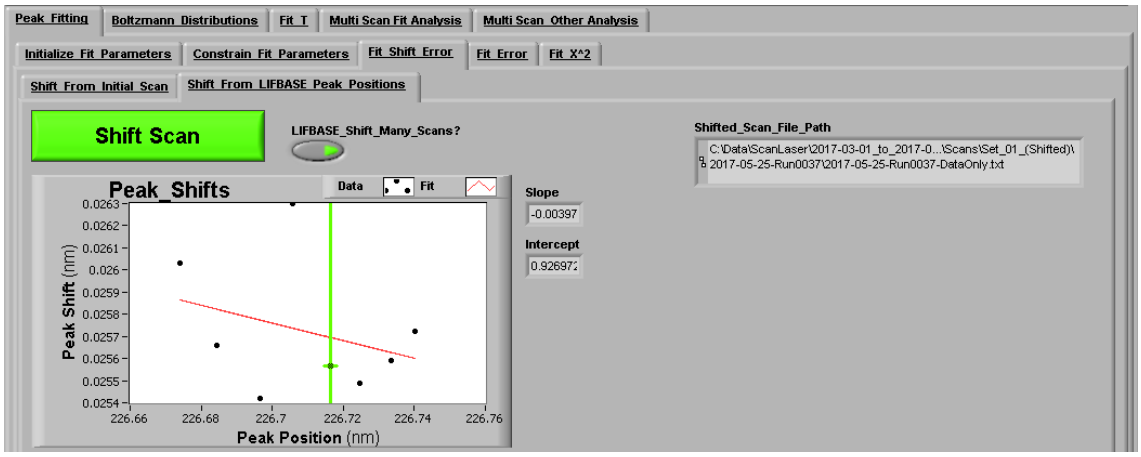

FIG. 72. Plot of fit peak position vs shift from the value assigned by LIFBASE.

A linear fit to the shift of each peak from LIFBASE vs the peak position determined from the Gaussian fit was utilized for each scan to shift and stretch the wavelength values of experimental scans to match the true wavelength values. This method corrected for small errors in the wavelength calibration of the dye laser.